ALMA MATER STUDIORUM

UNIVERSITÀ DEGLI STUDI DI BOLOGNA

Dipartimento di Fisica e Astronomia

Dottorato di ricerca in Astronomia
Ciclo XXIX

Clustering of clusters as a cosmological probe

CANDIDATO:
Alfonso Veropalumbo

RELATORE:
Prof. Lauro Moscardini

CO-RELATORE:
Dr. Federico Marulli

COORDINATORE:
Prof. Francesco Rosario Ferraro

Esame finale anno 2016

Contents

Introduction

Galaxy clusters play a leading role in both present and planned cosmological investigations (see Allen, Evrard, and A. B. Mantz, 2011, and references therein). They represent the biggest collapsed structure of the Universe, sitting on top of the highest peaks of the dark matter density field. These objects are considered from long time as cosmological probes; the possibility to link their observed properties to the fundamental quantities of their host haloes, modelled as a function of cosmological parameters, is in fact very concrete. The advantage in using these objects for this kind of studies comes from a) the presence of multiple independent methods covering the whole spectrum to determine the total halo mass: this helps in understanding the systematics that affect different procedures and then provide a robust mass estimate; b) the less sophisticated modelling required to link the observations with cosmologically relevant quantities, as for these masses the baryon physics has only a marginal influence; the same cannot be exploited with e.g. galaxies, as the link between the total mass and observable quantities is much more influenced by baryon physics.

These positive aspects apply also to the case of clustering of galaxy clusters. Moreover, clusters have a large clustering signal, due to the high bias and a very negligible contribution from non-linear redshift-space distortions caused by peculiar motions of objects in virialized haloes. All of these advantages counterbalance the larger measurement uncertainties due to the paucity of cluster sample with respect to galaxy clustering analyses. Moreover, the possibility to combine all the probes the galaxy clusters can provide gives us an unique instrument to address the fundamental puzzles in the present-day cosmology (Sartoris et al., 2016).

In this Thesis we will exploit the clustering of an optically selected sample of galaxy clusters, focusing in particular on the two-point correlation function (2PCF). In § 1 we will give a general overview on clustering. Firstly, we will describe the basic concepts of standard cosmological model and on the theory of structure formation. Then we will provide details on the methods used to measure the clustering signal from samples of discrete tracers and how to model them to derive cosmological constraints. In § 2 we will present the CosmoBolognaLib (Marulli, Veropalumbo, and Moresco, 2016), a large set of Open Source C++ numerical libraries for cosmological calculations, aimed at defining a common numerical environment for cosmological investigations of the large-scale structure of the Universe. In these libraries are implemented all the tools that we will use in this thesis. We will describe in § 3 our results on clustering, focusing in particular on the detection and modelling of the baryon acoustic oscillation peak. In § 4 we will exploit the *standard ruler* technique to measure the distance from the BAO peak detected from the clustering of three cluster samples, selected in three different redshift

ranges. We will then sample the distance-redshift relation and derive constraints on different cosmological models. We will present in § 5 a joint analysis of clustering and stacked lensing to break the degeneracy between the bias and the power spectrum amplitude parameter σ_8. Finally, in § 6 we draw our conclusions.

Chapter 1

Clustering - theory and observations

The standard cosmological model is the theoretical framework that describes the evolution of the Universe, its dynamic and the emerging of structures from the growth of gravitational instabilities of small overdensities. This paradigm postulates that the Universe is spatially homogeneous and isotropic, and evolves according to the General Relativity theory of gravity. The Universe is found to be spatially flat, and formed in a hot Big Bang scenario about 13.8 Gyr ago, as confirmed from observations of the Cosmic Microvawe Background (CMB) (Planck Collaboration et al., 2016).

Its evolution is determined by its energy budget. The latter consists of several components: relativistic radiation (lights and neutrinos); non-relativistic matter, made of a dominant dark component, the *cold dark matter* (CDM) that interacts only gravitationally and a minor fraction of baryonic matter; finally the larger part of the energy budget today is composed of a *dark energy* (DE) component, that can be described as a constant term, Λ. The seeds of the gravitational instabilities are the quantum fluctuations, stretched to macroscopic scales during an exponentially expanding phase at very early time, called *cosmic inflation*.

In this chapter we will overview the basic assumptions of the standard cosmological model that we aim to constrain in the forthcoming sections of this Thesis. in § 1.1 we will describe the geometry of the Universe, and how the Universe dynamics is influenced by its content § 1.1.1. In § 1.2, we will describe the growth of perturbations, that led to the large-scale structure properties observed at present days, starting from linear theory, in § 1.2.1, and then briefly outlining the theory of non-linear growth in § 1.2.2. Finally, we will describe the emerging of collapsed objects from the peaks of the density field in § 1.3. We will review the most common definitions of distances used in cosmological analyses in § 1.1.3, focusing in particular on baryon acoustic oscillation feature, that is described in § 1.4. Finally we will present the main techniques used to measure and model the two-point correlation function (2PCF) in § 1.5, and § 1.6.

1.1 Metric of the Universe space-time

The two main pillars of the standard cosmological model are the General Relativity (GR) theory and the *Cosmological Principle* (CP). GR is the theory of gravity developed by Albert Einstein in 1915, in which the Newtonian gravitational scalar field is replaced by a 4-th dimensional tensor, that describes the behaviour of space-time in presence of

mass. The field equations are:

$$G_{\mu,\nu} = \frac{8\pi G}{c^4} T_{\mu,\nu} \, , \tag{1.1}$$

where G is the gravitational constant and c is the speed of light. Eq. (1.1) relates the source of the gravitational field, that is the energy-momentum tensor, $T_{\mu,\nu}$, with the space-time curvature $G_{\mu,\nu}$.

The CP states that the Universe is homogeneous and isotropic on large scales; that is, its main properties appears the same at each observer, in all directions. Indeed, large scale structure studies demonstrated the isotropy of the present day universe on scales larger than $150\,\mathrm{Mpc}$; going to earlier epochs the same results appear from the analysis of the temperature distribution of cosmic microwave background radiation, which deviation from the mean value of $T = 2.7255$ K is of the order of 10^{-5}. Homogeneity is instead impossible to be probed directly. It must be assumed that we are not a privileged observer in the Universe: this can only be *not rejected* by testing data against non-homogeneous models (see Maartens, 2011, for a review of homogeneity tests) .

The direct consequence from these assumptions is the possibility to define a uniquely determined space-time metric: the *Robertson-Walker* metric (RW), defined as follows:

$$ds^2 = c^2 dt^2 - a(t)^2 \left[\frac{dr^2}{1 - Kr^2} + r^2 d\Omega^2 \right] \, , \tag{1.2}$$

where ds^2 is the infinitesimal element separating two events in space-time, c is the speed of light, dt is the time interval and dr, $d\Omega$ is the spatial separation in spherical coordinates. The metric depends on two quantities:

- the scale factor $a(t)$, that describes the evolution of the space; as a consequence of the cosmological principle, only the temporal dependence remains,

- the curvature constant K, that describes the geometry of the Universe and can have three values: $K = 0, -1, +1$, that mean flat, hyperbolic and spherical Universe, respectively; moreover it is important to notice that this quantity is constant with time.

Keeping fixed the angular coordinates, we can derive two types of distances from RW:

- the proper distance, that is the distance computed by considering contemporaneity in the measure ($dt = 0$):

$$d_p(r,t) = a(t) \int \frac{dr}{\sqrt{(1 - Kr^2)}} = a(t) f(r) \, , \tag{1.3}$$

$$f(r) = \begin{cases} \sinh^{-1}(r) & K = -1 \\ r & K = 0 \\ \sin^{-1}(r) & K = 1 \end{cases} \tag{1.4}$$

- the comoving distance, that is the proper distance computed today ($t = t_0, a(t) = a_0$):

$$d_c = a_0 f(r) = \frac{a_0}{a(t)} d_p(r,t) , \tag{1.5}$$

From Eq. (1.4) we can obtain the expansion rate of the Universe, that is the *Hubble* function:

$$H(t) \equiv \frac{\dot{a}(t)}{a(t)} , \tag{1.6}$$

The Universe expands (contracts) if $H > 0$ ($H < 0$). Taylor expanding at second order the scale factor $a(t)$ for t_0 and after some algebra we obtain:

$$a(t) \approx a_0 \left[1 + H_0(t - t_0) - q_0 H_0^2 (t - t_0)^2 \right] , \tag{1.7}$$

where H_0 is the Hubble constant and q is the deceleration parameter, defined as:

$$q = -\frac{\ddot{a}a}{\dot{a}^2} , \tag{1.8}$$

According to the above definition, the space accelerates if $q < 0$, and viceversa. The Hubble constant and the deceleration parameter can be used to approximate the description of the universe dynamics, the first describing the expansion rate, the second quantifying how fast it is. In the following, we will provide more general equations that describes the dynamics of the Universe as a function of its content.

1.1.1 Universe components

The energy content of the Universe enters the Einstein field equations (Eq. 1.1) trough the stress-energy tensor, $T_{\mu,\nu}$. The most generic choice under the CP assumption is to assume a multi-species perfect fluid:

$$T_{\mu,\nu} = (p + \rho)U_\mu U_\nu + p g_{\mu,\nu} , \tag{1.9}$$

where ρ and p are the energy density and pressure of the fluid, U_ν its $4-$velocity and $g_{\mu,\nu}$ is the space-time metric. For non-interacting particle species, the stress energy tensor can be written as the sum of the contributions of each component: $T_{\mu,\nu} = \sum_{i=1}^{N} T_{\mu,\nu}^i$.

Applying continuity equations to this quantity, $\nabla^\nu T_{\mu,\nu} = 0$, Eq. (1.9) becomes:

$$\dot{\rho} + 3\frac{\dot{a}}{a}(\rho + p) = 0 . \tag{1.10}$$

Each of the Universe component can be considered a *barotropic* fluid, so that its equation of state can be written as:

$$p = wc^2 \rho , \tag{1.11}$$

where w the equation of state parameter. From Eqs. (1.10) and (1.11), one can easily derive the equation that links energy density and Universe dynamics:

$$\rho \propto a(t)^{-3(1+w)} , \tag{1.12}$$

with $a(t)$ the scale factor.

Taking the first derivative with respect to ρ in Eq. (1.11), we derive the fluid speed of sound as $c_s^2 = \frac{\mathrm{d}p}{\mathrm{d}\rho} = wc^2$..The Zel'dovich interval is defined by imposing $c_s < c$. It provides the range of allowed values for the equation of state parameter: $0 \leq w < 1$.

The main components of the Universe are the following:

- non-relativistic matter, in the form of baryonic matter and CDM whose equation of state parameter is $w_m = 0$. The matter energy density contribution scales as the volume, getting diluted as the Universe expands;

- relativistic component, with $w_r = \frac{1}{3}$. Its energy density scales as a^{-4}: relativistic species such as photons and massless neutrinos get diluted and lose energy as a consequence of the expansion;

- the cosmological constant: The solutions of the Einstein field equations are invariant for a constant term Λ; interpreted as the vacuum energy, this term enters the stress-energy tensor as an extra density component $\rho_\Lambda = -\frac{\Lambda c^4}{8\pi G}$. From Eq. (1.9) it can be derived $w_\Lambda = -1$.

The standard cosmological paradigm can be extended once we relax the cosmological constant hypothesis, that is we can introduce a DE component with equation of state $w_{de} \neq -1$. There is no restriction on w_{DE}, it can be either constant or redshift dependent: Chevallier and Polarski (2001) and Linder and Jenkins (2003) propose the following parametrization (CPL):

$$w_{DE} = w_0 + w_a \frac{z}{1-z} , \tag{1.13}$$

where w_0 is the present day value of the equation of state and w_a parametrises its redshift evolution.

1.1.2 Friedmann equations

Solving the Einstein field equations, using Eq. (1.2) as a metric, for an isotropic and homogeneous Universe and a perfect fluid stress-energy tensor, only 2 equations remain independent. These are called the *Friedmann* equations:

$$\dot{a} + Kc^2 = \frac{8\pi G}{3}\rho a^2 + \frac{\Lambda}{3}, \qquad \ddot{a} = \frac{4\pi}{3}G\left[\rho + \frac{3p}{c^2}\right]a + \frac{\Lambda}{3} \tag{1.14}$$

where ρ is the energy density and p is the pressure; $\dot{a}, \ddot{a}$ are the first and second time derivatives of the scale factor, respectively.

Defining the critical density as:

$$\rho_{crit} = \frac{3H(t)^2}{8\pi G} \; ,$$

(1.15)

and combining Eqs. (1.12), (1.15), we can write the density parameter, Ω as:

$$\Omega = \frac{\rho}{\rho_{crit}} = \frac{8\pi G}{3H_0^2}\rho = \frac{8\pi G}{3H_0^2}\rho_0 \left(\frac{a_0}{a}\right)^{3(1+w)} \; .$$

(1.16)

Substituting the latter into first Friedmann equation for a multi-component fluid, we have:

$$\frac{H^2(a)}{H_0^2(a)} = \left(\frac{a_0}{a}\right)^2 \left[\sum_i \Omega_{0,i}\left(\frac{a_0}{a}\right)^{1+3w_i} + 1 - \Omega_0\right] \; ,$$

(1.17)

where $H(t)$ and H_0 are the Hubble function values at t and $t = 0$ respectively, Ω_0 is the total density parameter today and the sum runs over the energy density components. From Eq. (1.17) we can deduce two fundamental points. The first is that dynamics of the Universe is determined completely by its contents. The second one is related to the curvature constant K: by further manipulating the first Friedmann equation, we can write:

$$Kc^2 = -\frac{\Omega_k a_0^2}{D_H^2} \; ,$$

(1.18)

where $\Omega_k = 1 - \Omega_0$ is the present day total energy density parameter and $D_H = c/H_0$ is the Hubble distance. It is evident that the curvature is determined by the total amount of energy in the Universe; if $\rho > \rho_{crit}$ the Universe is closed, while $\rho < \rho_{crit}$ means an open Universe. Finally $\rho = \rho_{crit}$ stands for a flat Universe.

By looking at the second time derivative of the scale factor, $\ddot{a}$ it can be easily shown that the expansion is accelerated only if $w \leq -\frac{1}{3}$: In fact, the deceleration parameter can be written as follows:

$$q_0 = \frac{\Omega_0}{2}\left(1 + 3w\right) \; ,$$

(1.19)

A Universe with only components whose equation of state fall into the Zel'dovich interval cannot experiencing an accelerated expansion.

1.1.3 Distances in cosmology

In the previous sections we have seen how strong is the connection between the Universe dynamics and its contents. In this section we will describe how this connection can be exploited to derive cosmological constraints.

The most important distance indicator is the redshift, that is the wavelength shift of the observed spectrum with respect to its rest frame value, due to photons travelling in

an expanding space. By integrating the RW geodetics, we have:

$$z \equiv \frac{\lambda_o - \lambda_e}{\lambda_e} = \frac{a_0}{a(t)} - 1 \; , \tag{1.20}$$

where a_0 and $a(t)$ are respectively the scale factor nowadays and at time t. An expanding (contracting) Universe implies $a_0 > a(t)$ ($a_0 < a(t)$), then the observed wavelenght of distant sources will be redshifted (blueshifted) with respect to the emitted wavelength. Taking the first order of Eq. (1.7) we obtain $cz = H_0 d_p$; that is a reasonable approximation only at low redshift.

We can rewrite the comoving distance as:

$$D_C(z) = D_H \int_0^z \frac{\mathrm{d}z}{\sqrt{E(z)}} \; , \tag{1.21}$$

with $D_H = c/H_0$ is the Hubble distance and $E(z) = H(z)/H_0$ is given by Eq.(1.17). We can introduce also the other distance definitions, as follows:

- the luminosity distance D_L: this quantity is defined to keep unaltered the relation between the source flux F and the intrinsic luminosity L, that is $\rightarrow F = \frac{L}{4\pi D_L^2}$. Taking into account the redshift due to photons travelling in the expanding space, D_L can be written as:

$$D_L = a_0 r(1+z) \; , \tag{1.22}$$

  where from Eq. (1.5), $r = f^{-1}(D_C/a_0)$.

- angular diameter distance D_A: suppose we have a source with angular extension $\delta\theta$ at $r = r_1$, emitting photons at $t = t_1$; Eq (1.2) relates its angular size to the proper dimension as $D = a(t_1)r_1\delta\theta$. We can define:

$$D_A(t) = a(t)r \; . \tag{1.23}$$

In order to constrain fundamental quantities related to the geometry of the Universe, it's required to measure independently distances and redshifts. This can be done by comparing distance-dependent observables, such as fluxes or projected source sizes, *a*bsolute quantities, known a priori or calibrate independently. This is the case of *standard candles* and *standard rulers* , sources with known absolute magnitude and intrinsic sizes, respectively.

1.2   Basic concepts of clustering

As already stated, the CP holds only at very large scales. In fact the Universe is largely inhomogeneous at scales $\leq 150\mathrm{Mpc}$ with an hierarchy of structures emerging from the

background density field. The density contrast δ is defined as:

$$\delta(\vec{x}) \equiv \frac{\rho(\vec{x}) - \overline{\rho}}{\overline{\rho}} \; , \tag{1.24}$$

where $\rho(x)$ is the punctual density and $\overline{\rho}$ is the background mean density. Its Fourier transform is:

$$\hat{\delta}(\vec{k}) = \frac{1}{(2\pi)^{3/2}} \int \mathrm{d}^3 x \, \delta(\vec{x}) \mathrm{e}^{i\vec{k}\cdot\vec{x}} \; , \tag{1.25}$$

where $k = 2\pi/x$.

As a theoretical starting point, we can assume that density contrast is a homogeneous and isotropic stochastic field; the value of the field at each point is randomly extracted from a probability distribution, that has to be invariant for translations and rotations. This extends the CP to a perturbed Universe. The exact theoretical description of the density contrast field is not achievable as the field comes out of stochastic processes. Instead what can be modelled are the compressed statistical information that describe it. To complicate the picture, we are not able to compare different realizations: the observed Universe represents the only achievable realisation among all ones. Nevertheless, we can exploit the ergodic hypothesis, that states that the mean between the different realisations is equal to the spatial mean of a single one: according to this principle, sufficiently distance regions evolved independently between each other. CP + Ergodic assumption together form the so called *Fair Sample* hypothesis.

To determine the density contrast field, we can measure its moments. The mean value and the first order central moments are zero, (Eq. 1.24). The first significant quantity is the variance. In the density fluctuations are Gaussian, the variance is all we need to describe statistical properties of the density field. The variance of the density contrast field can be computed by taking the spatial average:

$$\sigma^2 \equiv \frac{1}{V_\infty} \int \mathrm{d}^3 x \, < \delta^2(x) > \; , \tag{1.26}$$

where $V_\infty = \int \mathrm{d}^3 x$ is the so-called *Universe volume.* that in *Fourier* space become:

$$\sigma^2 \equiv \frac{1}{(2\pi)^3 V_\infty} \int \mathrm{d}^3 k \, < \delta^2(k) > \; . \tag{1.27}$$

$< \delta^2(k) >$ is what is called the *power spectrum* $P(k)$, and measures the contribution of scales k to a generic fluctuation in configuration space, $\delta(x)$. Its anti-transform is the two-point correlation function (2PCF):

$$\xi(r) = \frac{1}{(2\pi)^{3/2}} \int \mathrm{d}^3 k P(k) \mathrm{e}^{ikr} \; . \tag{1.28}$$

Moreover, punctual density fluctuations cannot be observed directly; we can actually measure only mass fluctuations averaged on a typical scale R:

$$\delta_M(\vec{x}) \equiv < \frac{\delta M}{M} >= \delta(\vec{x}) * W(\vec{x}, R) \;, \tag{1.29}$$

where R is the scale, $M \propto \bar{\rho}R^3$ and $W(\vec{x}, R)$ is the window function.

This operation provide a filtered density field; all the information at scale $< R$ is then lost. $\delta_M(\vec{k})$ is again the Fourier transform of $\delta_M(\vec{x})$. In Fourier space convolutions became products, so that:

$$\delta_M(\vec{k}) = \delta(\vec{k})\hat{W}(\vec{k}, R) \;, \tag{1.30}$$

where $\delta(\vec{k})$ and $\hat{W}(\vec{k}, R)$ are the Fourier transform of $\delta(\vec{x})$ and $W(\vec{x}, R)$ respectively.

From Eq. (1.29) the *mass variance* is defined as the convolution of the power spectrum with the window function $\tilde{W}_R(k)$:

$$\sigma_M^2 \equiv \frac{1}{(2\pi)^3 V_\infty} \int \mathrm{d}^3 k \; < \delta^2(\vec{k}) > \hat{W}^2(\vec{k}, R) \;. \tag{1.31}$$

This quantity is the typical size of a density fluctuation on a scale R. The value of this quantity at $z = 0$ and $r = 8\,\mathrm{Mpc}\,h^{-1}$, that is σ_8, is commonly used to parametrise the power spectrum normalization.

1.2.1   Linear perturbation theory

As long as the density contrast field is much lower then 1, the linear theory can be applied to obtain analytic solutions for the growth of structures. The approach is similar to the classical *Jeans* solution for gravitational instabilities, here expanded to a non-static space.

From fluid equations approximated at first order and modified for an expanding Universe, we can derive the dispersion relation:

$$\ddot{\delta}_k + 2\frac{\dot{a}}{a}\dot{\delta}_k + \delta_k \left[k^2 v_s^2 - 4\pi \mathrm{G}\rho_b \right] = 0, \;, \tag{1.32}$$

where v_s^2 is the speed sound, ρ_b is the background density and $k = k_{com}/a$ is the *physical wave number*. This equation links the temporal evolution of fluctuations on a scale k of a certain component to the background expansion. It thus depends on a) the type of component, which determines the pressure term via the sound speed, b) the epoch considered, that determines the background evolution. Another important consequence is that the density contrast depends only on its scale k; fluctuations on different scales evolves independently. This is one of the main advantages of the linear approximation.This condition will cease to be true when approaching non-linear regimes.

In analogy with classical Jeans theory, we can define a typical length $\lambda_J = \sqrt{(\pi c_s^2)/(\mathrm{G}\rho)}$, at which corresponds a mass $M_J \propto \lambda_J^3 \rho_b$. This scale separates two regimes: for $\lambda > \lambda J$

perturbations become unstable and can growth; for smaller values, fluctuations propagate into the fluid at the sound speed. The dissipation scale, λ_d, separates the regimes at which perturbations can survive, from the ones in which perturbations are washed out by energy exchange between particles. The dissipation scale is associated to the typical particle velocity, the speed of sound for baryonic matter, the dispersion velocity for DMr particles. It is worth notice that both the Jeans scale and the dissipation scale change with time and as a function of cosmological parameters.

We are going to present the solutions for the growth of fluctuations before and after the equivalence, by assuming that in these two epochs the background evolution is described by a radiation dominated (for $z > z_{eq}$) and matter dominated (for $z < z_{eq}$) Einstein-de Sitter model. The solutions presented below are valid for $\Omega = 1$. It can be shown that the growth outside and inside the horizon for $\Omega < 1 \, (> 1)$ Universe is slower (faster) with respect to the one of flat universe.

Outside the horizon

Above the horizon scale ($\lambda > R_H$), by definition, perturbations are dominated by gravity, as these scales are not causally connected. The growth of fluctuations is common for all the components and it only depends on the background cosmology.

We have the following trends:

- $\delta_{DM} \propto \delta_b \propto \delta_R \propto a^2$ for $z > z_{eq}$,

- $\delta_R \propto \delta_b \propto \delta_{DM} \propto a$ for $z < z_{eq}$,

where δ_{DM}, δ_b and δ_R are the fluctuations of DM, radiation and baryons respectively.

Inside the horizon

Due to their high sound speed, radiation fluctuations cannot growth inside the horizon scale as their Jeans scale is larger than the horizon: each overdensity is then rapidly cancelled. For the matter component we have to consider different behaviours before and after the equivalence: before the equivalence, DM fluctuation can growth until they enter the horizon, then they remain frozen; this is the so called *stagnation* effect (Meszaros, 1974). Their maximum growth is $\propto (a_H/a_{eq})^2$, where a_H and a_{eq} are the value of the scale factor when the perturbation scale crosses the horizon and at the equivalence epoch, respectively. After the equivalence, fluctuations larger than the Jeans scale growth at a rate $\dot{\delta} \propto a(t)$. Fluctuations that enters the horizon after the equivalence never stop to growth.

Baryons stay coupled to radiation until Compton scattering is efficient against expansion of the Universe. The baryon-photon fluid oscillates in the already collapsed DM haloes and, after decoupling ($z < z_{dec}$) they are free to collapse, with a growth $\delta_B = \delta_{DM}(1 - a_{dec}/a)$(baryon catch-up), where a_{dec} is the scale horizon at z_{dec}.

Primordial power spectrum and transfer function

The standard cosmological paradigm predicts an early phase of *inflation*, in which the expansion of the scale factor is exponential with time, and thus the expansion is accelerated. The inflationary phase provides a mechanism for the origin of the initial seeds of the large-scale structure that we see today. The distribution of the primordial density fluctuations is described by a power-law power spectrum:

$$P(k) = A_s k^{n_s}, \tag{1.33}$$

where A_s and n_s are the amplitude and the scalar index of primordial power spectrum, respectively. The value of n_s has been measured with high accuracy with CMB data. It's concordance values is $n_s = 0.968 \pm 0.006\pm$ (Planck Collaboration et al., 2016). The growth of perturbations modifies the primordial shape according to:

$$P(k,t) = A_s k^{n_s} \left(\frac{D(t)}{D(t_0)} \right)^2 T(k) , \tag{1.34}$$

where $D(t)$ is the growth factor, that scales as $a \propto 1/(1+z)$ after equivalence, and $T(k,t)$ is the transfer function that describes how much of the original perturbation survives the processes related to micro-physics (i.e. the sub-horizon effects). The scales interested by this kind of processes are the ones smaller than the horizon scale before equivalence. We have:

$$k \to 0 \implies T(k) \to 1 , \tag{1.35a}$$
$$k \to \infty \implies T(k) \to k^{-2} \to 0 . \tag{1.35b}$$
$$\tag{1.35c}$$

The scale that separates these two regimes is the size of the horizon at the equivalence. Thus it depends on both Ω_M and Ω_r.

1.2.2 Growth of perturbations in non-linear regime

The linear perturbation theory works only at very high redshift, and is accurate enough to reproduce the CMB power spectrum (see e.g. Planck Collaboration et al., 2014b). This is not enough anyway to reproduce the properties of the observed non linearly evolved density field.

The description of the density field evolution in non-linear regime cannot be done analytically: the major complication, as anticipated in § 1.2.1, is mode-coupling: the growth depends on all the scales k. The basic approach is the so-called *Perturbation Theory* (PT), that extends to higher orders the equations describing the gravitational instability. The linear theory briefly summarised in § 1.2.1 represents its limit at first-order. For a review on PT and its extension see Bernardeau et al. (2002) and Crocce and Scoccimarro (2006). The PT modelling is not the unique way to address the question. Many efforts have also been spent in the past to build large cosmological simulations,

aimed to directly look the non-linear effects of gravity, to have an independent re-alisation to be compared with models and data. (see e.g. Sanchez et al., 2016, for a comparison between models and simulations).

The final goal is to have a theory that should be able to predict with high accuracy statistical properties of the density field. The big challenge is that future surveys are predicted to reach a statistical precision that is below the present day systematics of theoretical models.

Far to be exhaustive on the topic, we provide some basic results that are useful for the context of this Thesis; we will present the first order Largrangian perturbation theory solutions for the non-linear evolved density field, commonly recognized as *Zel'dovich* approximation (ZA) (Zel'dovich, 1970).

The Lagrangian approach to perturbation theory (LPT) aims at describing the non-linear density field by the *displacement* field $\vec{\Psi}((\mathbf{q}, t))$:

$$\mathbf{x}(t) = \mathbf{q}(t) + \vec{\Psi}(\mathbf{q}, t) , \tag{1.36}$$

where $\mathbf{x}(t)$ and $\mathbf{q}(t)$ are respectively the Eulerian and Lagrangian particle positions, respectively. The displacement field is the function that maps the two reference frames. The *Zel'dovich* approximation is the linear solution of the motion equations in LPT. For $\vec{\Psi}((\mathbf{q}, t))$ we have:

$$\nabla_{\mathbf{q}} \vec{\Psi}(\mathbf{q}, t) = -D(t)\delta(\mathbf{q}) , \tag{1.37}$$

where $D(t)$ is the growth factor and $\delta(\mathbf{q})$ is the density field contrast in Lagrangian coordinates. From Eq. (1.36) we can derive the Jacobian of the transformation, that is $\mathcal{J} = \nabla_{\mathbf{q}} \vec{\Psi}(\mathbf{q}, t)$. Putting together the latter, and Eq. (1.37), and considering an overdensity in Eulerian coordinates $\bar{\rho}(1+\delta(x))\mathrm{d}x^3 = \bar{\rho}\mathrm{d}q^3$ we get the following solution:

$$1 + \delta(\mathbf{x}, t) = \frac{1}{(1 - D(t)\lambda_1)(1 - D(t)\lambda_2)(1 - D(t)\lambda_3)} . \tag{1.38}$$

where λ_i are the eigenvalues of the Jacobian matrix.

Being $D(t)$ positive, the sign of eigenvalues determine the way collapse proceed:

- all negative eigenvalues: no collapse;

- only one positive eigenvalue: the collapse happens only along one direction, forming bi-dimensional structures;

- two positive eigenvalues: filamentary structures form;

- all positive eigenvalues: the growth happens along all the axis, with matter that condensates in nodes.

Results from numerical simulations show that the collapse happens at most in filamentary structures, with large structures as groups of clusters that form at their intersections.

ZA led to a good approximation for the non-linear power spectrum, at least when sufficiently large scales are considered. It is also useful to *revert* the effect of the non-linear growth on the observed density field. This method is called the *reconstruction* technique (Eisenstein, Seo, and M. White, 2007).

1.3 Haloes

In this section we will describe the basic concepts on formation of collapsed DM structures, that is the haloes, and the connection with the underlying density field. We will start by reviewing the analytic treatment of the spherical collapse in § 1.3.1. The we will move to describe the main statistics of haloes in § 1.3.2, and their relation with the density field in § 1.3.3.

1.3.1 Spherical collape

Spherical collapse represents the simplest model of non-linear growth, and the only one with an exact analytic solution (Gunn and Gott, 1972; Lahav et al., 1991). This model describes the evolution of a spherical overdensity, that detaches from the background density field and possibly collapse in a finite timescale. The collapse follows three phases:

- expanding phase: the overdensity still follows the background dynamics, but decelerates due to the gravitational field attraction, and finally stops at the turnaround epoch, t_{ta};

- collapse: after reaching t_{ta}, the perturbation evolves independently from the background and starts to collapse;

- virialization: the collapse is stopped by the internal matter pressure; the structure is now formed in a typical timescale $t = t_c = 2t_{ta}$. The full virialization happens $t_{vir} = 3t_{ta}$.

At the time of collapse, the overdensity reaches the value $1 + \delta_{NL} \approx 178$. Extrapolate from linear theory, the corrisponding value of the overdensity is $\delta = 1.68$. We actually consider as collapsed all the fluctuations that reach this value of δ in the linear approximation. Despite its simplicity, this model then represents the starting point for the description of collapsed structures. (Press and Schechter, 1974).

1.3.2 Halo mass function

The spherical collapse describes how an overdensity eventually becomes high enough to detach from the background evolution and to collapse in a bound object, that we

call *haloes*. Their comoving number density is strictly related to cosmology, and is determined by the mass function:

$$\frac{\mathrm{d}n(M,z)}{\mathrm{d}M} = f(\sigma(M,z))\frac{\bar{\rho}}{M}\frac{\mathrm{d}\ln\sigma(M,z)^{-1}}{\mathrm{d}M} \ . \tag{1.39}$$

$f(\sigma(M,z))\bar{\rho}$ is the amount of mass contained in fluctuations of typical mass $M = \frac{4}{3}\pi R^3\bar{\rho}$, with $\bar{\rho}$ the average matter density and σ the density contrast for a fluctuation on scale R.

The simplest argument that can be invoked to derive this quantity analytically comes from the spherical collapse (§ 1.3.1): a perturbation is considered collapsed when it reaches the threshold value $\delta_c = 1.68$. Assuming that the probability distribution function for a perturbation on a scale M is a Gaussian with variance σ_M^2 (Eq. (1.31)), we can derive an analytic function for $f(\sigma)$:

$$f(\sigma(M)) = \sqrt{\frac{2}{\pi}}\frac{\delta_c}{\sigma(M)}\exp\left(-\frac{\delta_c^2}{2\sigma^2(M)}\right). \tag{1.40}$$

This results is the basis of the *Press-Schechter* theory (PS) (Press and Schechter, 1974). Subsequent works extended this theory by relaxing some of its assumptions, such as the spherical geometry. For instance, Sheth and Tormen (2002) proposed a more accurate model by considering an elliptical collapse.

A different approach is to compute the comoving number density of haloes from numerical simulations. (e.g. Angulo et al., 2012; Crocce et al., 2010; Jenkins et al., 2001; Reed et al., 2007; J. Tinker et al., 2008).

One of the fundamental characteristics of the mass function is that it decreases at large masses. The dependence on cosmology enters trough the smoothed density field term, that is $\sigma(M)$. Larger smoothing radii correspond to larger masses. this implies that bigger haloes trace the highest (and rarest) peaks of the density field. Thus, massive haloes are less abundant with respect to smaller ones in a fixed comoving volume.

From Eq. (1.39) it is straightforward to obtain the total number of haloes N_h above a certain mass threshold M_{min} in a volume V:

$$N_h = A \int_{z_{min}}^{z_{max}} \int_{M_{min}}^{\infty} \frac{\mathrm{d}V}{\mathrm{d}z}n(M,z)\mathrm{d}M\mathrm{d}z \ , \tag{1.41}$$

where A is the area, z_{min} and z_{max} are the redshift boundaries and $\frac{\mathrm{d}V}{\mathrm{d}z}$ is the comoving volume element.

1.3.3 Halo bias

The mass function provides the average abundance of haloes as a function of mass, that at a given redshift can be computed by counting the amount of matter in fluctuations large enough to collapse $\delta > \delta_c$ (Press and Schechter, 1974). The collapse is anyway

dependent also on the local density fluctuation. Assuming the PS formalism, the ratio between the number of collapsed haloes in a Lagrangian volume with respect to the mean value can be written as:

$$\delta_h^L = \frac{\delta n}{n} = \left(\frac{\nu^2 - 1}{\delta_c} \right) \delta_0 \ , \tag{1.42}$$

with δ_h^L and δ_0 the density contrast of haloes and matter respectively, and $\nu = \delta_c/\sigma_M$ with δ_c the critical density above which the collapse can happen and σ_M the typical root mean square of matter fluctuations. At fixed M (σ_M), if $\delta_0 > 0$ ($\delta_0 < 0$) the number of haloes is larger (lower) than the mean value. Varying M, if $\delta_c > \sigma_M$ ($< \sigma_M$) the number of haloes is larger (lower) than the mean value. At $M = M_*$ the number of haloes is equal to the average. Mapping to Eulerian coordinates one can write:

$$\delta_h = \frac{\delta n}{n} = \left(1 + \frac{\nu^2 - 1}{\delta_c} \right) \delta \ , \tag{1.43}$$

being δ_h and δ the overdensity of haloes and matter respectively and $\nu \propto \sigma(M)^{-1}$. The halo bias then becomes:

$$b_h = \left(1 + \frac{\nu^2 - 1}{\delta_c} \right) \ . \tag{1.44}$$

Thus in the PS formalism, the bias depends only on the mass, M, and the redshift and it is scale independent. It is easy to derive that the bias increases with M. Going to second order statistics, Eqs.(1.71b) and (1.44) give:

$$\xi_{hh} = \left(1 + \frac{\nu^2 - 1}{\delta_c} \right)^2 \xi_m = b^2(M, z)\xi_m \ . \tag{1.45}$$

It can be noticed that in case we are able to measure the halo mass function, both the bias and the correlation function depends on the DM density field; the bias is itself, in this case, a model prediction.

By assuming a model for the bias $b(M, z)$, it is possible to obtain the effective bias of a haloes sample above a certain threshold M_{min}:

$$b_{eff}(z) = \frac{\displaystyle\int_{M_{min}}^{\infty} n(M, z)b(M, z)\mathrm{d}M}{\displaystyle\int_{M_{min}}^{\infty} n(M, z)\mathrm{d}M} \ . \tag{1.46}$$

Being weighted by the mass function, the effective bias is almost equal to the bias of the smallest halos, as the latter dominate in number.

The first to introduce the bias argument was (Kaiser, 1984), which noticed the different clustering of galaxies and galaxy clusters. Rare objects such as clusters show and enhanced clustering signal with respect to the galaxy correlation. Their rarity is then the key to explain this effects, as they can only form at the highest peaks of DM density field.

1.4   The baryon acoustic oscillations

The early time Universe was denser and hotter with respect to the present day. According to the theory of *thermal history*, the one that describes the behaviour of the thermodynamic properties of the Universe as a function of its energy density content, it existed a phase in which the baryonic matter, mainly composed by H, He, and traces of light elements as a result of big bang nucleosynthesis, was completely ionized. This allowed frequent photon-electrons interactions via *Compton scattering*. The continuous energy exchanges made the two components *coupled*.

The baryon-photon fluid perturbations oscillate in the already formed DM potential wells, instead of directly collapse in them, due to the equilibrium between gravitational attraction and radiation pressure. The sound speed c_s can be computed assuming the balance between radiation pressure and gravitational inertia of the baryons; this quantity depends on the baryon-to-photon density ratio, via the relation:

$$c_s = \frac{c}{\sqrt{3(1 + 3\frac{\rho_b}{\rho_\gamma})}} \ . \tag{1.47}$$

The causal connection between the components stays until photon-electron scattering is efficient against the expansion of the Universe.

After $\sim 10^5$ years from the Big Bang, the decreased background temperature allowed atoms to recombine, consequently decreasing number density of free electrons. This made interactions between photons and baryons more and more inefficient, until the total *decoupling*, that happens at $z_{dec} = 1100$, at the *last scattering surface*.

The maximum distance a wave emitted from the centre of a potential well can reach is the sound horizon r_s:

$$r_s = \int_{z_{dec}}^{\infty} \frac{c_s}{H(z)} \mathrm{d}z \ . \tag{1.48}$$

The sound horizon scale is $\approx 150 \mathrm{Mpc}$.

After recombination, without the pressure support, baryons start to collapse into DM haloes and form structures. Photons instead streams away from them forming the radiation background we see today as the CMB.

In a very simplified picture, we can describe the Universe immediately after decoupling as filled with DM density perturbations surrounded by shells of baryons in stalling density waves at a typical distance of r_s. These waves can have constructive interference, increasing the density where crests are on top of each other, and generating a peak in the power spectrum, or either have destructive interference, where crests and troughs meet. Hence, one finds a harmonic pattern of oscillations in the matter power spectrum, and a peak in the correlation function, given the mathematical connection, at the sound-horizon scale.

The baryon-photon oscillations stay imprinted in both the baryon and photon energy density. Indeed they are clearly seen as temperature fluctuations in the CMB

and as oscillations in the power spectrum, called the *Baryon acoustic oscillations* (BAO).

How this signal is seen today depends on the properties of the universe components, from z_{dec} to the present day. Radiation does not interact with the other components: as a consequence the signal arrives *almost* unaltered. Baryons contributes to a minimal part to the total matter power spectrum, that is DM dominated. Nevertheless the oscillation amplitude in the matter power spectrum depends on the baryon fraction. Moreover, the BAO feature is influenced by the non-linear growth of perturbation too. Thought the latter has direct effects only at relatively small scales ($r > 10\,\mathrm{Mpc}\,h^{-1}$), they can actually impact also larger separation, including the BAO scale, causing a damping of the signal, and a shift of the peak (see e.g. Eisenstein, Seo, and M. White, 2007, and references therein).

The detection of the BAO peak was a fundamental success of the standard cosmological picture, as it confirmed thermal history of the Universe and the structure formation paradigm (Anderson et al., 2014; Beutler et al., 2011; Blake et al., 2011; Eisenstein, Seo, and M. White, 2007; Eisenstein et al., 2005; Kazin et al., 2014; Ross et al., 2015, 2016). Moreover, the BAO is itself one of the most powerful cosmological probe as it can be used to exploit the technique of the *standard ruler*, to map the distance-redshift relation (see § 1.1.3). We can write, in fact:

$$D_A(z) = \frac{r_s}{\Delta\theta(1+z)} \,, \tag{1.49a}$$

$$H(z) = \frac{c\Delta z}{r_s} \,. \tag{1.49b}$$

where r_s is the sound horizon, and $c\Delta z$ and $\Delta\theta$ are respectively its radial and angular sizes of the as seen in the matter distribution distribution.

1.5 Measuring the clustering of discrete samples

The clustering of matter is strictly linked to the Universe dynamics, as we showed in § 1.2. It complements distance-based cosmological probes, and will be at the centre of the future of cosmological analysis.

As described in § 1.2, the 2PCF and power spectrum describe statistics of the perturbed density field. As we move from theory to observation, we need to take into account the effects that link discrete tracers of the DM density field to the global statistical properties of the Universe. Measuring the clustering of galaxies, clusters, and other cosmic tracers is not the same as measuring the clustering of the density field, for the following reasons;

- we do not measure the punctual density contrast, $\delta(x)$. Indeed, by using discrete tracers we measure its smoothed version, computing number counts contrast in cells of finite volume;

- the number density contrast depends on observational systematics that modify the sources distribution on the sky; this effect is included in the so called *selection function*;

- tracers are biased with respect to the density field in a way not easy to model;

- the clustering measure depends on the observed tracers positions: distortions effects enter the measure since a) redshifts are not a pure distance indicator; b) a cosmology must be assumed to convert to physical coordinates;

- the measured covariance, $C_{i,j}$, must be estimated at very high precision in order to not bias the constraints.

We will describe these aspects in more details in this section, focusing mainly on clustering in configuration space. We will describe our choices on how to treat the bias, as well as geometric and dynamic distortions in § 1.5.1, 1.5.2, 1.5.3. We review the techniques used for 2PCF measures in § 1.5.4 and describe the modelling used in this Thesis to derive clustering constraints in § 1.6.

1.5.1 Bias

The main complication affecting clustering studies is the fact that all *particles* such as galaxies, galaxy clusters, AGN etc. do not exactly trace the DM density field. This complicates the modelling of the connection between matter overdensities and counts; the link between the matter density field δ_{DM}, and the number density contrast, δ_t, where the subscript t indicates a generic tracer, is a function of δ_{DM}:

$$\delta_t \equiv \frac{\delta n}{\bar{n}} = f\left(\delta_{DM}\right) \ . \tag{1.50}$$

A convenient choice is to assume a linear dependence in 1.50, parametrized by a bias factor, so that:

$$\delta_t = b\delta_{DM} \ , \tag{1.51}$$

from which it follows.

$$\xi_t(r) = b^2 \xi_{DM}(r) \ . \tag{1.52}$$

Theory and numerical simulations show that the bias is extremely complicated to model: it is stochastic, and it depends on galaxy properties such as luminosity, colour and/or morphological type. Moreover the linear relation Eq. 1.51 only holds on sufficiently large scales (Cacciato et al., 2013; Marulli et al., 2013, and references therein).

Our ignorance on the bias impacts the cosmological constraints we will be able to derive from clustering measurements. Specifically, the bias is highly degenerate with the amplitude parameters such as the initial power spectrum normalization or

the density fluctuations growth rate. A common strategy is to consider the bias as a nuisance parameter.

Informations complementary to the density field statistics are required to break this degeneracy. Halo mass proxies are one example. Haloes are biased tracers of the DM density field, and their bias is mass dependent (Bhattacharya et al., 2013; Sheth and Tormen, 1999; J. L. Tinker et al., 2010) as described in § 1.2. Combining number counts and clustering of massive objects, such as galaxy clusters, is thus a possible way to break degeneracies (see e.g. Mana et al., 2013; Sartoris et al., 2016).

1.5.2   Geometric distortions

Geometric distortions enter when a *fiducial* cosmology, instead of the true one, is assumed to convert observed coordinates to physical ones. This has the effect of altering the object distances differently in direction transverse and parallel to the line of sight.

The transformation can be written as:

$$\mathrm{d}^3 s = \left[(1+z)^2 D_A(z)^2 \frac{cz}{H(z)} \right] \mathrm{d}\Omega \mathrm{d}z \; , \tag{1.53}$$

where $\mathrm{d}^3 s$ and $\mathrm{d}\Omega \mathrm{d}z$ are respectively the volume elements in physical and observed coordinates, and the term in parenthesis is the Jacobian transformation. We define the volume-averaged distance as:

$$D_V(z) = \left[(1+z)^2 D_A^f(z)^2 \frac{cz}{H^f(z)} \right]^{1/3} \; , \tag{1.54}$$

where $D_A^f(z)$ and $H^f(z)$ are the angular diameter distance and the Hubble function computed in the fiducial cosmology, respectively. We can define a cosmology independent quantity: $\mathrm{d}s^3 / D_V^f(z)^3$, assuming that also the following relation holds, independently of the assumed cosmological model:

$$\mathrm{d}^3 s' = \left[\frac{D_V^{f'}(z)}{D_V^f(z)} \right]^3 \mathrm{d}^3 s \; , \tag{1.55}$$

where $D_V^{f'}(z) \, D_V^f(z)$ are the isotropic volume distance assuming two different cosmological models.

A statistic based on the position of discrete tracers such as the 2PCF, is clearly affected by the geometric distortions. In order to extract unbiased results, the relation in Eq. (1.55) must be taken into account. In Fig 1.1 we show the monopole of the 2PCF of a simulation computed with two different fiducial cosmologies. Left panel shows how the same signal is distorted by this difference in computing the distances. In the right panel it is clearly shown how geometric distortions can be modelled by performing the transformation $s \to y_s \equiv s/D_V^f(z)$ (see Sánchez et al., 2012, for further details).

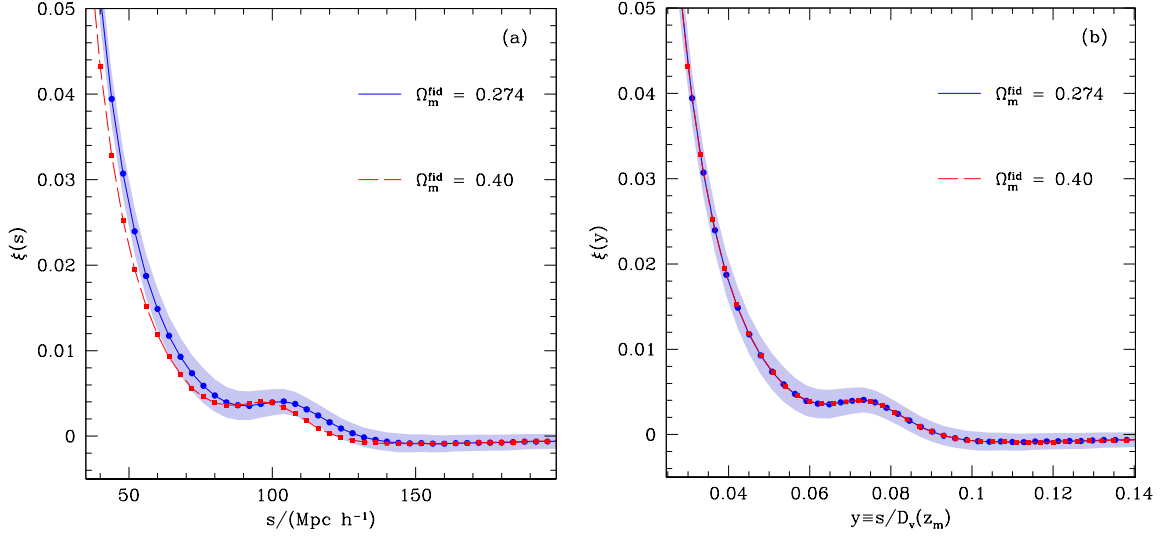**Figure 1.1:** *left panel*: measure of 2PCF monopole for a set of mocks using two different value of Ω_M^{fid} to convert observed coordinates, respectively $\Omega_M = 0.274$ (blue circles and line) and $\Omega_M = 0.4$ (red squares dashed lines). Shaded blue region is the typical variance of the data. *Right panel*: same measurements as the left panel, but expressed as a function of $y_s == \equiv s/D_V^f(z)$. This removes the dependence on the fiducial cosmology. Further details can be found in (Sánchez et al., 2012)

1.5.3 Redshift-space distortions

This kind of distortion enters the analysis when using the redshift as a distance proxy. In fact, the redshift encodes also information about the peculiar motions parallel to the line of sight:

$$z_{obs} = z_c + \frac{v_\parallel}{c}(1 + z_c) + \frac{\sigma_z}{c} , \qquad (1.56)$$

with c the speed of light, z_{obs} and z_c the observed and cosmological redshift respectively, $v_\parallel$ the parallel to the line of sight component of the object velocity, σ_z the error on the measurement.

There are two main source of peculiar velocities:

- the motion of structures generated by gravitational instabilities: this term depends on the density field itself and satisfies the following relation:

$$\vec{v} = \frac{2}{3}\frac{G\rho_{cr}a}{H}f(\Omega) , \qquad (1.57)$$

where $f \equiv \frac{\mathrm{d}\ln\delta}{\mathrm{d}\ln a}$ is the linear growth rate; a good approximation in standard ΛCDM+GR is to assume $f = \Omega_M^\gamma$, with $\gamma = 0.545$ for GR (Kaiser, 1987; Peebles, 1980);

- the random motion of galaxies inside virialized DM haloes. This term causes the so-called *fingers-of-God* effect: structures appear elongated along the line of sight.
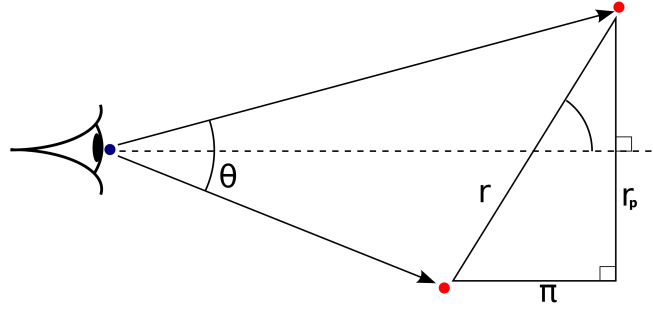
Figure 1.2: A sketch describing the coordinate convention used in this Thesis. The blue point represents the observer, while the red points represent a pair of objects separated by a distance r. r_p and π are the component of r transverse and perpendicular to the line of sight; $\theta = \pi/r$.

In § 1.5.3 we will describe in more detail how to treat these effects in clustering analyses, and discuss about the cosmological information that can be extracted from them.

1.5.4 Clustering measurements

In the following we will discuss the most important aspects and issues concerning the clustering measurement. We will discuss the 2PCF monopole estimators in § 1.5.4, and their extension for anisotropic clustering, $\xi r_p, \pi$ and multipole expansion in § 1.5.4. We will review the method to integrate over RSD by projecting and de-projecting $\xi(r_p, \pi)$ in § 1.5.4. We will review the technique to obtain the 2PCF covariance matrix in § 1.5.4. In Fig. 1.2, we report the convention for coordinate estimates used in this Thesis.

Two-point correlation function estimators

The 2PCF, $\xi(r)$, describes the joint probability $\mathrm{d}P_{12}$ of finding a pair of objects, in two volumes $\mathrm{d}V_1$ and $\mathrm{d}V_2$ separated by the distance r:

$$\mathrm{d}P_{12} = \bar{n}^2 \left[1 + \xi(r)\right] \mathrm{d}V_1 \mathrm{d}V_2 \,, \tag{1.58}$$

where $\bar{n}\mathrm{d}V_i$ is the stochastic probability of finding an object in $\mathrm{d}V_i$, being $\bar{n}$ the average object density. From this definition it is evident that $\xi(r) = 0$ means an exactly random distribution of points; $\xi(r) > 0$ a positive correlation and $-1 < \xi(r) < 0$ a negative correlation. From a practical point of view, one generally measure the quantity $\mathrm{d}P_{12}$ binned in shells of width Δr, as

$$\mathrm{d}P_{12} = \frac{DD(r)}{N_{DD}} \,, \tag{1.59}$$

with $DD(r)$ the total number of objects pairs separated by a distance $r \pm \Delta r$ divided by the total number of pairs in the sample $N_{DD} = N_D(N_D - 1)/2$. We should then provide the term $\bar{n}^2 \mathrm{d}V_1 \mathrm{d}V_2$. This term describes the uncorrelated probability of find a

pair of objects; it must encodes all the geometrical properties of the volume sampled by the data. The most common and straightforward way to take into account the latter is to extract a random sample from the survey volume and compute pairs as well as for data, obtaining (from Eq. (1.58) imposing $\xi(r) = 0$):

$$\bar{n}^2 \mathrm{d}V_1 \mathrm{d}V_2 = \frac{RR(r)}{N_{RR}} \; , \tag{1.60}$$

being $RR(r)$ and N_{RR} the analogous of $DD(r)$ and N_{DD} for a random collection of points. Simply comparing this two quantities, we obtain the Peebles and Hauser (1974) (PH) unbiased estimator of the correlation function:

$$\hat{\xi}_{PH}(r) = \frac{N_{RR}}{N_{DD}} \frac{DD(r)}{RR(r)} - 1 \; . \tag{1.61}$$

Being a statistics based on discrete counts of stochastic variables, its variance should scale as the inverse of number of pairs (Poissonian variance). Landy and Szalay (1993) (hereafter LS) demonstrated that PH is not a minimum variance 2PCF estimator, and proposed the following solution:

$$\hat{\xi}_{LS}(r) = \frac{N_{RR}}{N_{DD}} \frac{DD(r)}{RR(r)} - 2 \frac{N_{RR}}{N_{DR}} \frac{DR(r)}{RR(r)} + 1 \; , \tag{1.62}$$

where the $DR(r)$ term is the number of data-random cross pairs and $N_{DR} = N_D N_R$ is the total number of cross pairs. The LS estimator is unbiased and with minimum variance; it is widely used in studies involving clustering in configuration space and validated against distributions with known correlation signal (e.g. Hamilton, 1993; Labatie et al., 2010, and references therein). Finally, In order to have an estimate of the correlation function whose variance is not affected by discrete pair counts from the random sample, the random collection of point should be larger than the clustered one.

Anisotropic clustering estimate

Geometrical and dynamical distortions impact on the shape of the 2PCF introducing predictable anisotropic effects that can be disentangled by looking at 2D clustering at sufficiently large scales (Marulli et al., 2012). Analogously to the 1D 2PCF case (Eq. (1.62)), the 2D 2PCF estimator is:

$$\xi(r_p, \pi) = \frac{DD(r_p, \pi) + RR(r_p, \pi) - 2DR(r_p, \pi)}{RR(r_p, \pi)} \; , \tag{1.63}$$

where $DD(r_p, \pi)$, $RR(r_p, \pi)$. $DR(r_p, \pi)$ are the data-data, random-random, data random pairs, computed in bins of transverse and parallel to the line-of-sight separations, Δr_p, Δ_π respectively. In real space at the true cosmology $\xi(r_p, \pi) \equiv \xi(r)$, with $r = \sqrt{r_p^2 + \pi^2}$. In redshift space, the peculiar velocity term distorts the clustering signal along the line of sight in a predictable way; at small separations separations, random

motions cause the distortion known as fingers-of-God effect, while at larger separations linear velocities enhance the clustering signal. In order to reduce the number of bins, a more convenient strategy is to measure the moments of $\xi(r_p, \pi)$, by expanding on the Legendre polynomials:

$$\xi_l(r) = \frac{2l+1}{2} \int_0^1 \xi(r, \mu) \mathcal{L}_l \mathrm{d}\mu \, , \tag{1.64}$$

where l is the order of the Legendre polynomial expansion, $\mu = \pi/r$ is the cosine of angle between the object separation and the line of sight. Since the majority of the information is in $l \leq 4$ multipoles; the higher order multipoles can be generally neglected, moreover for l odd the multipoles are $= 0$ for symmetry reasons. Using the multipoles instead of the full 2D 2PCF increases the anisotropic signal and reduces the size of the covariance matrix, that enters in the 2PCF modelling.

A similar result can be achieved measuring the wedges of the 2D 2PCF (Kazin et al., 2014), that are defined as:

$$\xi_w(r) = \frac{1}{\delta\mu} \int_0^1 \xi(r, \mu) \mathrm{d}\mu \, . \tag{1.65}$$

Alleviating redshift space distortions

In order to alleviate the RSD effects, two statistics can be used: the *projected* 2PCF, $w_p(r_p)$, and the *deprojected* one. The projected 2PCF is defined as an integral of $\xi(r_p i, \pi)$ along the line of sight:

$$w_p(r_p) = \int_0^\infty \mathrm{d}\pi' \xi(r_p, \pi'), \tag{1.66}$$

where $\xi(r_p, \pi)$ is measured in bins of perpendicular, r_p, and parallel, π, separations with respect to the line-of-sight. Integrating along the direction parallel to the line-of-sight allows us to alleviate RSD distortions effects.

The real space correlation function can then be measured by deprojecting w_p, by using the Abel integral (Davis and Peebles, 1983; Saunders, Rowan-Robinson, and Lawrence, 1992):

$$\xi(r) = -\frac{1}{\pi} \int_r^\infty \frac{\mathrm{d}w_p}{\mathrm{d}r_p} \frac{\mathrm{d}r_p}{\sqrt{r_p^2 - r}} \, . \tag{1.67}$$

Eq. (1.67) strictly holds in the limit of integrating to infinity to obtain w_p. This procedure instead depends on the choice of the parameter π_{max}, the maximum scale at which the integral is performed. This parameter must be optimized, too small values

produce a noisy estimate of the projected 2PCF, too large values can introduce noise from large separation (Coil et al., 2008; Norberg et al., 2009; Zehavi et al., 2011).

Covariance matrix

The covariance matrix $C_{i,j}$ is a crucial ingredient for clustering analyses. It measures the variance and correlation between 2PCF bins. It can be directly estimated using mock catalogues extracted from numerical simulations (see e.g. Anderson et al., 2014; Kazin et al., 2014). and it is defined as follows:

$$C_{i,j} = \frac{1}{N-1} \sum_{k=1}^{N} (\xi_i^k - \hat{\xi}_i)(\xi_j^k - \hat{\xi}_j) \, , \tag{1.68}$$

where the subscripts i and j run over spatial bins of the correlation function and k refers to the 2PCF of the kth of N realizations; $\hat{\xi}$ is the mean 2PCF of the N realizations.

However, this method is very computational expensive since a large set of mocks have to be created and analysed. Alternatively, different statistical techniques can be exploited, that still provide fairly robust estimates of the covariance matrix. For our analysis, we consider the following approaches:

- internal error estimators: the covariance matrix can be estimated by subsampling the original catalogue and calculating the correlation function in all but one subsamples (jackknife), or in a random selection of them (bootstrap), recursively (see e.g. Norberg et al., 2009);. This technique has the clear advantage of being very fast in producing the covariance matrix, already including possible systematics effects and biases, as well as contributions from higher order correlations. On the other hand, this approach is limited by the survey volume and often produce a conservative estimates of the variance and noisy off-diagonal terms: aspects that has an impact on the modelling of the 2PCF;

- external error estimator, we consider *fast* methods to produce a large number of mocks, with a *target* 2PCF signal. The most famous of them is the lognormal density field technique, by Coles and Jones (1991). This method to infer the covariance matrix has been already used by several authors for clustering analyses (see e.g. Beutler et al., 2011; Blake et al., 2011; Chuang et al., 2015). An approach like that can give a very clear estimate of the covariance matrix, in a reasonable amount of time, but it lacks controls on the systematics that a full simulations can include.

Recovering the full information content from baryon acoustic oscillations

In § 1.4 we briefly reviewed physics of the BAO and their use in cosmology as *standard rulers* to constrain distances.

Also we noticed that non-linear growth has an impact on the BAO as well, smearing and shifting the peak, in configuration space or the oscillatory pattern in Fourier space.

Effect of non-linear growth cause a loss of the original information available from the BAO in the linear density field. A possible strategy is to recover the BAO peak selecting tracers able to trace a more linear density field such as structure with large bias (Angulo et al., 2014; Eisenstein, Seo, and M. White, 2007; Wang and Zhan, 2013).

Another methodology is to apply *reconstruction* techniques, that is aimed at revert the effects on the non-linear growth of the density perturbation; (see e.g. Padmanabhan et al., 2012; M. White, 2015, and references therein). To understand the way reconstruction works we consider *Zel'dovich* approximation (see § 1.2.2): the displacement field $\vec{\Psi}$ describing non-linear growths can be obtained from the density field itself. Thus, starting from a discrete sample and knowing its bias, $\vec{\Psi}$ can be computed by solving Eq. 1.37 and apply the displacements to positions of tracers, restoring their position in the linear density field.

Reconstruction is now a standard technique in the clustering analyses aimed at the BAO detection. It allows to improve the measured distance from the BAO position; nevertheless restoring the properties of the linear field results in a sharper BAO peak. Fig. 1.3 shows the 2PCF and $P(k)$ monopole of the galaxy sample obtained from the Baryon Oscillations Spectroscopic Sample (BOSS) (Anderson et al., 2014). Left and right panels show the 2PCF and the $P(k)$ respectively before and after the reconstruction (top and bottom panels, respectively). The original BAO signal, damped by the non-linear growth, is almost totally restored. The application of the reconstruction shrinks the BAO peak, located at $\approx 100\,\mathrm{Mpc}\,h^{-1}$, and a restore the original oscillation pattern BAO for the 2PCF and $P(k)$ respectively.

1.6 Modelling the clustering measures

In this section we will provide a description of the models used in this Thesis to model clustering signal and derive cosmological constraints. We will describe how to fit the bias by modelling the projected 2PCF (§ 1.6.1). We will present the de-wiggle template model Eisenstein, Seo, and M. White, 2007; Ross et al., 2012 for the fit of the BAO in the monopole of 2PCF in § 1.6.2. Finally, we will describe the dispersion model, aimed at modelling small scales anisotropic clustering (Davis and Peebles, 1983; Peacock and Dodds, 1996; Peebles, 1980) in § 1.6.3.

1.6.1 Bias from projected 2PCF

Projecting the 2D 2PCF along the line of sight reduces the effects of RSD on the 2PCF measurements. The model provided by Eq. (1.66) can thus be used, i.e. assuming that the 2D correlation function in isotropic it follows then:

$$w_p(r_p) = b^2 \int_{r_p^2}^{\sqrt{\pi_{max}^2 + r_p^2}} \mathrm{d}r \frac{2r\xi_{DM}(r)}{\sqrt{r^2 - r_p^2}} \,, \tag{1.69}$$
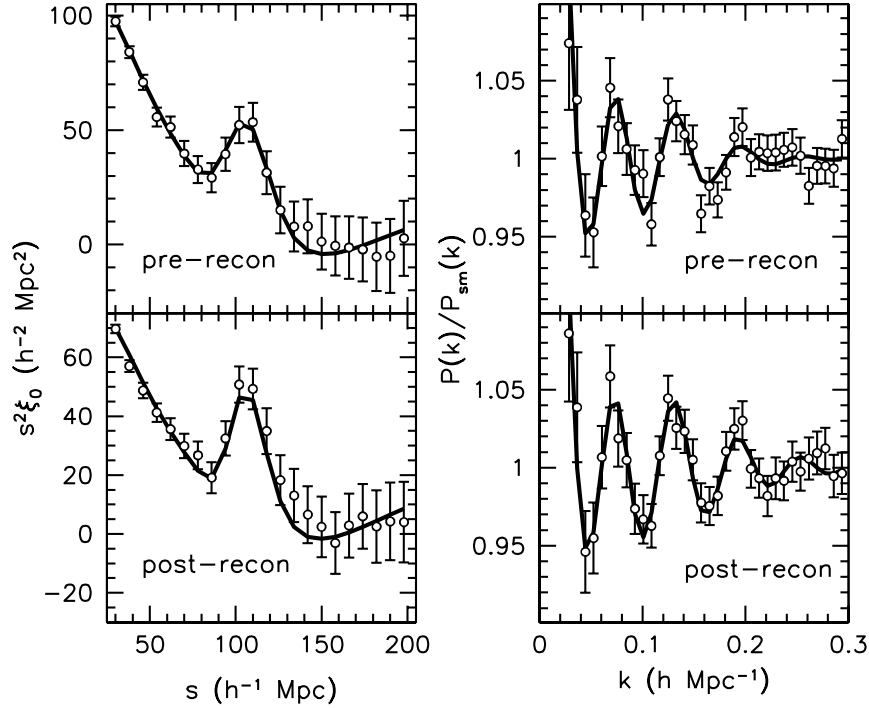
Figure 1.3: The BAO constraints obtained for the galaxy in the BOSS sample Anderson et al. (2014). The left panels show the measured 2PCF monopole before and after reconstruction of the density field. Right panels show the same, for the power $P(k)$. The reconstruction shrinks the BAO peak, restoring the linear pattern of the BAO for the 2PCF and the $P(k)$ respectively. Anderson et al. (From 2014)

where $\xi_{DM}(r)$ is the 2PCF. The linear bias b is then obtained by comparing this model with the data.

1.6.2 Baryon acoustic oscillations peak detection in the monopole

To obtain the distance constraints from the BAO peak, we adopt the following widely used and robust model (see Anderson et al., 2012, and reference therein):

$$\xi(r) = B^2 \xi_{DW}(\alpha r, \Sigma_{NL}) + A_0 + \frac{A_1}{r} + \frac{A_2}{r^2} , \tag{1.70}$$

where B factorises the difference between the DM 2PCF and the tracer 2PCF, α is the parameter that contains the distance information, and A_0, A_1 and A_2 are the parameters of an additive polynomial used to marginalize over small scales non-linear signals or systematics not fully taken into account. ξ_{DW} is the *de-wiggled* correlation function, obtained by Fourier transforming the *de-wiggled* DM power spectrum, P_{DW}

(Eisenstein, Seo, and M. White, 2007):

$$P_{DW}(k) = [P_{lin}(k) - P_{nw}(k)] \, e^{-k^2 \Sigma_{NL}^2/2} + P_{nw}(k) \, , \tag{1.71a}$$

$$\xi_{DW}(r) = \frac{1}{2\pi^2} \int \mathrm{d}k \, k^2 P_{DW}(k) \frac{\sin(kr)}{kr} \, , \tag{1.71b}$$

where P_{lin} is the linear power spectrum that can be computed e.g. with CAMB (Lewis and Bridle, 2002), while P_{nw} is the power spectrum without the BAO feature, that we will obtain by the parametric formula of Eisenstein, Seo, and M. White (2007). As can be noticed, the model ignore the small scales non linear effects, being focused in pinpointing the peak position. Effects of non-linear growth of structures at the BAO scales are controlled by the parameter Σ_{NL}, that describes the smearing of the BAO, and it is left free to vary. The model for $\xi_{DW}(r)$ is then obtained by Fourier transforming the power spectrum, (Eq. 1.71b). Fig. 1.4 shows the effects of the damping on the power spectrum and correlation function for for different values of $\Sigma_{NL} = \{0, 5, 10, 20\} \, \mathrm{Mpc} \, h^{-1}$.

The distance constraint is entirely contained in α (Eq. 1.70). That can be derived through the following by correcting for geometric distortions: approximation:

$$D_V(\bar{z}) = \alpha D_V^{fid}(\bar{z}) \left(\frac{r_s}{r_s^{fid}} \right) \, \mathrm{Mpc} \, . \tag{1.72}$$

Eq. (1.72) states that the distance constraint at the mean redshift of the catalogue is α times the distance at the fiducial cosmology, scaled to the ratio between the true and fiducial sound horizons. $D_V(\bar{z})$ is the isotropic volume distance calculated at the mean redshift of the catalogue, defined in Eq. (1.54). If we assume that the true value of the sound horizon is known, we can directly measure a distance; otherwise we can exploit an *uncalibrated* version of the standard ruler technique, measuring the ratio $d_z = D_V(z)/r_s$.

1.6.3   Modelling Redshift-Space distortions

The peculiar motion of structures are a consequence of the growth of matter perturbations. This peculiar velocity field is directly linked the density field itself, being $v \propto \dot{\delta}$. RSD at large scales are due to the infall of objects inside bigger structures, and causes a squashing of the correlation function contours. This signal is another strong cosmological probe (see e.g. de la Torre et al., 2013; Guzzo et al., 2008; Sanchez et al., 2016, and references therein); that is parametrized with the linear growth rate parameters, previously defined in § 1.5.3 (Peebles, 1980).

By assuming the coordinate transformation in Eq. (1.56) and the peculiar velocity v from linear theory, Kaiser (1987) derives the transformation to map the density field
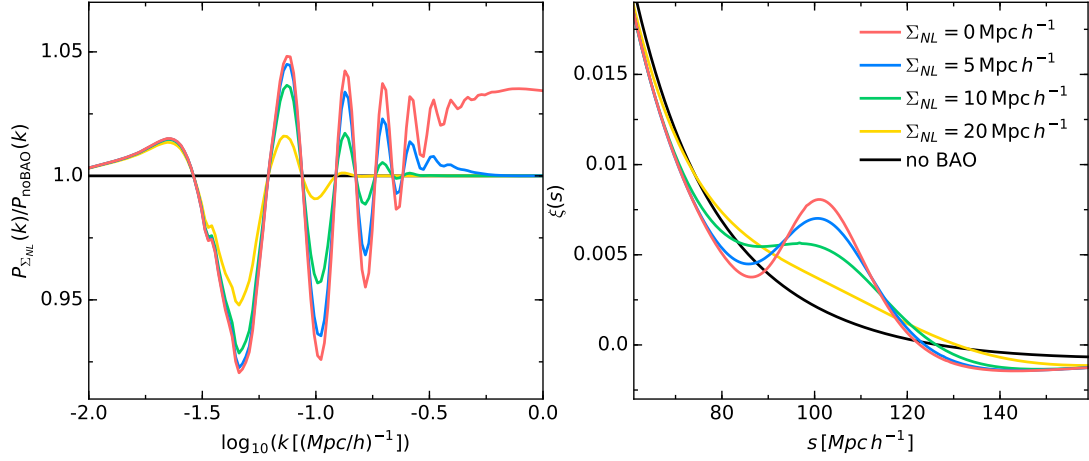
Figure 1.4: *left panel:* ratio of the power spectrum given by Eq. (1.71a), for different values of $\Sigma_{NL} = \{0, 5, 10, 20\}\,\mathrm{Mpc}\,h^{-1}$ and the power spectrum without the BAO feature. *Right panel:* Effects of the damping on the BAO peak in the 2PCF monopole, for the same values of Σ_{NL} as in left panel.

from real space to redshift space:

$$\delta_r(k) = (1 + f\mu^2)\delta_s(k) \; . \tag{1.73}$$

This implies that the linear redshift-space 2D power spectrum can be modelled in polar coordinates as follows:

$$P(k, \mu) = b^2 P_{\mathrm{DM}}(k)(1 + \beta\mu^2) \; , \tag{1.74}$$

with $\beta = f/b$.

Fisher, Scharf, and Lahav (1994) and Hamilton (1992) derive the linear redshift space 2PCF:

$$\xi(s, \mu) = \left[1 + f\left(\frac{\partial}{\partial\pi}\right)^2 \left(\nabla^2\right)^{-1}\right]\xi(r) \; , \tag{1.75}$$

where $\pi = s\mu$. Expanding the equation on a Legendre polynomial basis, we get:

$$\xi^{\mathrm{lin}}(s, \mu) = \xi_0(s)P_0(\mu) + \xi_2(s)P_2(\mu) + \xi_4(s)P_4(\mu) \; , \tag{1.76}$$

with:

$$\xi_0(s) = \left(1 + \frac{2}{3}\beta + \frac{1}{5}\beta^2\right) \cdot \xi(r) \tag{1.77a}$$

$$= \left[(b\sigma_8)^2 + \frac{2}{3}f\sigma_8 \cdot b\sigma_8 + \frac{1}{5}(f\sigma_8)^2\right] \cdot \frac{\xi_{\mathrm{DM}}(r)}{\sigma_8^2} \; , \tag{1.77b}$$

$$\xi_2(s) = \left(\frac{4}{3}\beta + \frac{4}{7}\beta^2\right)\left[\xi(r) - \overline{\xi}(r)\right] \tag{1.78a}$$

$$= \left[\frac{4}{3}f\sigma_8 \cdot b\sigma_8 + \frac{4}{7}(f\sigma_8)^2\right]\left[\frac{\xi_{\mathrm{DM}}(r)}{\sigma_8^2} - \frac{\overline{\xi}_{\mathrm{DM}}(r)}{\sigma_8^2}\right], \tag{1.78b}$$

$$\xi_4(s) = \frac{8}{35}\beta^2\left[\xi(r) + \frac{5}{2}\overline{\xi}(r) - \frac{7}{2}\overline{\overline{\xi}}(r)\right] \tag{1.79a}$$

$$= \frac{8}{35}(f\sigma_8)^2\left[\frac{\xi_{\mathrm{DM}}(r)}{\sigma_8^2} + \frac{5}{2}\frac{\overline{\xi}_{\mathrm{DM}}(r)}{\sigma_8^2} - \frac{7}{2}\frac{\overline{\overline{\xi}}_{\mathrm{DM}}(r)}{\sigma_8^2}\right], \tag{1.79b}$$

where P_l are the Legendre polynomials.

$\xi(r)$ and $\xi_{\mathrm{DM}}(r)$ are the real-space *undistorted* correlation functions of tracers and DM , respectively, whereas the *barred* functions are:

$$\overline{\xi}_{\mathrm{DM}}(r) \equiv \frac{3}{r^3}\int_0^r dr'\xi_{\mathrm{DM}}(r')r'^2, \tag{1.80}$$

$$\overline{\overline{\xi}}_{\mathrm{DM}}(r) \equiv \frac{5}{r^5}\int_0^r dr'\xi_{\mathrm{DM}}(r')r'^4. \tag{1.81}$$

Eq. (1.76)- (1.81) are derived in the distant-observer approximation, that is reasonable at the small scales.

Eqs. (1.77b)), (1.78b)) and (1.79b)) are derived from Eqs. (1.77a)), (1.78a) and (1.79a) respectively, assuming $\beta = f/b$. In the following analysis, $\xi_{\mathrm{DM}}(r)$ will be estimated by Fourier transforming the linear power spectrum computed with the software CAMB (Lewis and Bridle, 2002) for the cosmological model considered. Alternatively, the real-space 2PCF $\xi(r)$ can be estimated directly from the real-space mock samples, or computed with the deprojection technique shown in § 1.5.4 or from theoretical prediction assuming a value for the linear bias as shown in Eq. (1.67).

Eq. (1.76) is an effective description of RSD only at large scales, where non-linear effects are negligible. An empirical model that can account for both linear and non-linear dynamics is the so-called dispersion model (Davis and Peebles, 1983; Peacock and Dodds, 1996; Peebles, 1980), that describes the redshift-space correlation function as a convolution of the linearly-distorted correlation with the distribution function of pairwise velocities, $f(v)$:

$$\xi(s_\perp, s_\parallel) = \int_{-\infty}^{\infty} dv f(v)\xi\left(s_\perp, s_\parallel - \frac{v(1+z)}{H(z)}\right)_{\mathrm{lin}}, \tag{1.82}$$

where the pairwise velocity v is expressed in physical coordinates.

If redshift errors can be neglected, we use the exponential form for $f(v)$ (Marulli et al., 2012), namely:

$$f(v) = \frac{1}{\sigma_{12}\sqrt{2}} \exp\left(-\frac{\sqrt{2}|v|}{\sigma_{12}}\right) , \qquad (1.83)$$

(Davis and Peebles, 1983; Fisher, Scharf, and Lahav, 1994; Zurek et al., 1994). The quantity σ_{12} can be interpreted as the dispersion in the pairwise random peculiar velocities, and is generally assumed to be independent of pair separations (see e.g. Bianchi et al., 2012, for a detailed discussion). Other possible choices for $f(v)$ is the Gaussian form, typically used when large redshift errors contribute to the small scales RSD.

The dispersion model given by Eqs. (1.76)-(1.83) depends on three free quantities, $f\sigma_8$, $b\sigma_8$ and σ_{12} (since $\xi_{\mathrm{DM}} \propto \sigma_8^2$), and on the reference background cosmology used both to convert angles and redshifts into distances and to estimate the real-space DM 2PCF.

This model has been extensively tested against cosmological simulations (see e.g. Bianchi et al., 2012; Contreras et al., 2013; Marulli et al., 2015). In particular in Marulli, Veropalumbo et al. 2015 we tested the model to determine the best strategy to obtain unbiased results from the dispersion model. Fig. 1.5 shows the iso-correlation contours of the redshift-space 2PCF, corresponding to the values $\xi(s_\perp, s_\parallel) = [0.05, 0.1, 0.2, 0.4, 1, 3]$, (black contours) for clusters, in the range $\log(M_{500}[h^{-1}\,\mathrm{M}_\odot]) > 13$ and galaxies from the Magneticum simulation (Dolag et al, in prep.) at $z = 0.2$. The dot-dashed green and solid red contours show the best-fit model given by Eq. (1.82), with the real-space correlation function $\xi(r)$ measured directly from the simulation, and estimated from the CAMB power spectrum, respectively. The blue dashed contours show the linear best-fit model given by Eq. (1.76) with the CAMB real-space correlation function

1.6.4 Likelihood definition

All the cosmological constraints presented in the forthcoming sections of this Thesis are obtained with Bayesian inference method. These are based on the Bayes' theorem:

$$p(\vec{\theta} \,|\, \vec{X}) = \frac{p(\vec{X} \,|\, \vec{\theta})\, p(\vec{\theta})}{p(\vec{X})} , \qquad (1.84)$$

where $\vec{X}$ are the data, $\vec{\theta}$ are the model parameters, $p(\vec{\theta})$ is the prior probability distribution of the parameters, and $p(\vec{X} \,|\, \vec{\theta})$ and $p(\vec{\theta} \,|\, \vec{X})$ are the likelihood function and the parameter posterior probability distribution, respectively. $P(\vec{X})$ is the data prior, and it enters as a normalization constant.

Where not specified, we adopted for clustering modelling and cosmological constraints a standard Gaussian likelihood to describe the probability $p(\vec{X} \,|\, \vec{\theta})$. , $\mathscr{L}_{\mathrm{CL}} \propto$
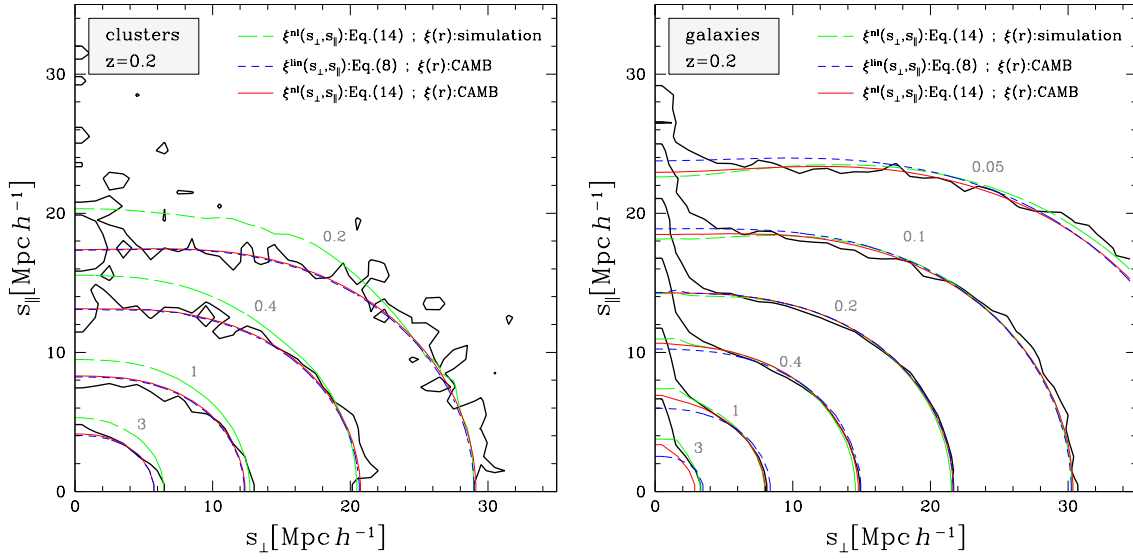
Figure 1.5: *left panel*: the iso-correlation contours of the redshift-space 2PCF, corresponding to the values $\xi(s_\perp, s_\parallel) = [0.05, 0.1, 0.2, 0.4, 1, 3]$, for clusters of the Magneticum simulation (Dolag et al, in prep.) with $\log(M_{500}[h^{-1}\,\mathrm{M_\odot}]) > 13$, at $z = 0.2$ (black contours). The dot-dashed green and solid red contours show the best-fit model given by Eq. (1.82), with the real-space correlation function $\xi(r)$ measured from the simulation, and estimated from the CAMB power spectrum, respectively. The blue dashed contours show the linear best-fit model given by Eq. (1.76) with the CAMB real-space correlation function. *Right panel*: Same as left panel, for galaxies with $\log(M_{\mathrm{STAR}}[h^{-1}\,\mathrm{M_\odot}]) > 10$, at $z = 0.2$

$\exp(-\chi^2_{\mathrm{CL}}/2)$, with

$$\chi^2_{\mathrm{CL}} = \sum_{i=0}^{n} \sum_{j=0}^{n} (\xi_i - \hat{\xi}_i) \mathbf{C}^{-1}_{ij} (\xi_j - \hat{\xi}_j) , \tag{1.85}$$

where ξ_i is the correlation function measured in the i-th spatial bin, $\hat{\xi}_i$ is the model and $\mathbf{C}^{-1}$ is the inverted covariance matrix.

Likelihood is generally not easy to be described; the most useful technique to sample that is to use the Monte Carlo Markov Chain (MCMC) procedure. This consists in sampling a target distribution using a correlated random walk: every step is extracted after a trial that depends only on the previous one (Markov process). The steps are collected in chains, that define marginalised posterior probability of the model parameters $p(\vec{\theta} \,|\, \vec{X})$.

1.7 Cosmological constraints from clustering

In order to provide precise estimates of the statistical properties of density field, clustering experiments aim to survey large volumes to extract cosmological information from both BAO and RSD.
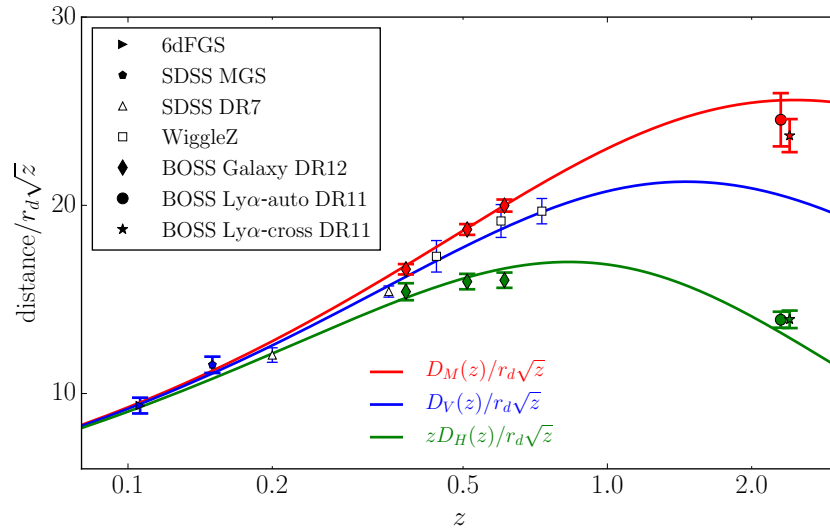
Figure 1.6: The *Hubble diagram* from a collection of BAO detections. Blue, red, and green points show BAO measurements of D_V/r_s, D_M/r_s, and zD_H/r_s, respectively, from BAO analysis of different surveys, as indicated in the legend. The latter can be compared to the corresponding coloured lines, which represent the predictions of the fiducial Planck ΛCDM model (Planck Collaboration et al., 2016). (From Alam et al., 2016).

An increasing number of clustering studies at local redshift ($z < 1$) has been performed in the last years such as Six degrees Field Galaxy survey (6dFGS Beutler et al., 2011), WiggleZ Dark Energy survey (Blake et al., 2011; Kazin et al., 2014), Sloan Digital Sky Survey I-II (SDSS Eisenstein et al., 2005), Baryon Oscillations Spectroscopic Survey (BOSS Anderson et al., 2014; Cuesta et al., 2016; Ross et al., 2016; Sanchez et al., 2016), VIMOS Public Extragalactic Redshift Survey (VIPERS) (Guzzo et al., 2014).

In particular Alam et al. (2016) presented the BOSS final constraints, obtained by combining all the clustering probes, after accurately estimating the covariance of the different methods.This provided the best ever clustering-based cosmological constraints.

Moreover, clustering is going to be one of the main cosmological probes also for the next future, with dedicated ongoing and planned experiments, such as Euclid (Amendola et al., 2013; Laureijs et al., 2011), eBOSS (Dawson et al., 2015), HETDEX (Stevans et al., 2014).

An large number of BAO distance measures has been obtained at local redshift, thanks to wide surveys of galaxies, (Anderson et al., 2014; Beutler et al., 2011; Cuesta et al., 2016; Kazin et al., 2014; Ross et al., 2016). Moreover, BAO can also be detected in the clustering pattern of other tracers, such as Lyα emitters (Delubac et al., 2015).

Their combination provides accurate constraints on the distance-redshift relation, that can be obtained by exploiting both the isotropic and anisotropic BAO standard ruler techniques (Aubourg et al., 2015). Fig.1.6 from Alam et al. (2016) shows a collection
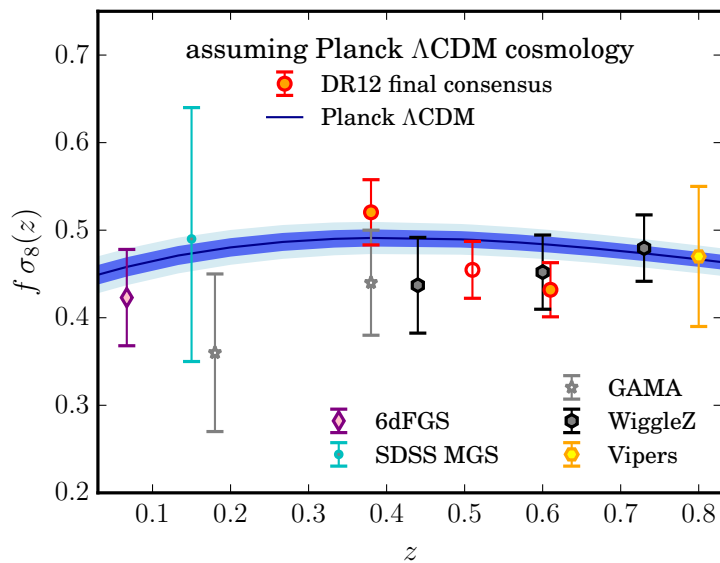
Figure 1.7: $f\sigma_8$ constraints as a function of redshift, from different galaxy surveys, as indicated in the legend. The blue shaded region is the predicted $f\sigma_8(z)$ from Planck ΛCDM background cosmology. (From Alam et al., 2016).

of constraints for D_V/r_s, D_M/r_s, cD_H/r_s in blue, red and green respectively from BAO detection in survey of galaxies and Lyα emitters.

Thanks to the advances in modelling the clustering properties, the measures of the linear growth rate $f\sigma_8$ can be constrained as well. Fig. 1.7 from Alam et al. (2016) shows a set of recent $f\sigma_8$ constraints from different galaxy surveys, compared to the Planck predictions; in particular the constraints shown are the one coming from the 2dfGRS (Percival et al., 2004), 6dFGS (Beutler et al., 2012), Galaxy and Mass Assembly survey (GAMA Blake et al., 2013), WiggleZ (Blake et al., 2012), Vimos VLT Deep Survey (VVDS Guzzo et al., 2008), and VIPERS (de la Torre et al., 2013) surveys, as well as the measurements from the SDSS-I and -II main galaxy sample (Howlett et al., 2015) and the SDSS-II Luminous Red Galaxy sample (Oka et al., 2014).

Probing the late time Universe with the BAO distance and linear growth rate, in synergy with early time constraints from CMB and from Supernova Luminosity distance measures (SN), allow us to measure with unprecedent precision dark energy-related cosmological parameters (i.e. Ω_Λ and w_{DE}), only marginally constrained from CMB measurements. As it can be seen in Figs. 1.6 and 1.7, BAO and RSD measurements are in reasonable agreement with predictions from the fiducial Planck cosmology (Planck Collaboration et al., 2016). As a further example, Fig.1.8 from Alam et al. (2016) shows the $1 - 2\sigma$ joint constraints on $\Omega_k - w$, from CMB data (green ellipses)and from CMB+BAO (grey ellipses). Combining CMB and the distance constraints has a huge impact on the parameter constraints. Moreover, adding constraints from full shape of the anisotropic 2PCF (FS) (red ellipses) and Supernova luminosity distance (Betoule et al., 2014) (blue ellipses), further improve the measured parameters, that appear fully
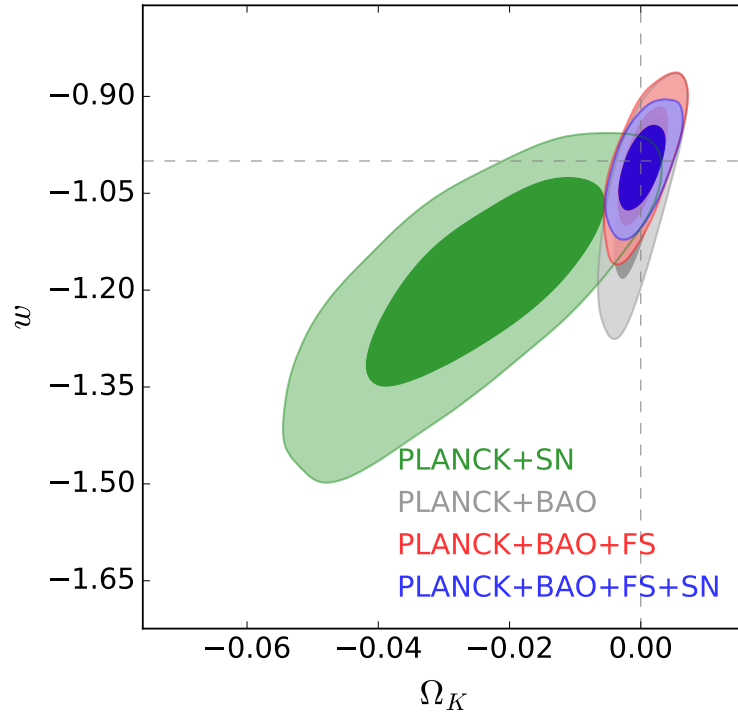
Figure 1.8: Parameter constraints for the owCDM cosmological models, comparing the results from BAO and BAO+FS to those with JLA SNe. One sees that the galaxy clustering results are particularly strong in the $\Omega_k - w$.

consistent with the ΛCDM predictions.

1.7.1 Clustering of galaxy clusters

The clustering of galaxy clusters contains the same information that can be extracted from galaxy clustering. Moreover, it can be combined to the mass function for cosmological studies. In the past, the main limitation was the small volume of the available cluster samples. The first cluster clustering measurements probed the high bias of these tracers (Bahcall, 1986; Bahcall and Soneira, 1983; Moscardini et al., 2000). The interest on the detection of the BAO in the clustering of galaxy cluster recently raised, thanks to large photometric and spectroscopic optical surveys such as the SDSS, which triggered the creation of photometric (Koester et al., 2007; Oguri, 2014; Wen and Han, 2015; Wen, Han, and Liu, 2009, 2012) and spectroscopic (Tempel et al., 2014) samples of galaxy clusters.

The first BAO detection from cluster clustering was claimed by Estrada, Sefusatti, and Frieman (2009) and Hütsi (2010), that measured the 2PCF and $P(k)$ for the MaxBCG sample (Koester et al., 2007) respectively. These works found a BAO detection at $\sim 2\sigma$ confidence level. The left panel of Fig. 1.9 shows the 2PCF of galaxy clusters from Estrada, Sefusatti, and Frieman (2009), while the right panel shows the power spectrum of the same sample measured by Hütsi (2010). Hong et al. (2012) used the spectroscopic
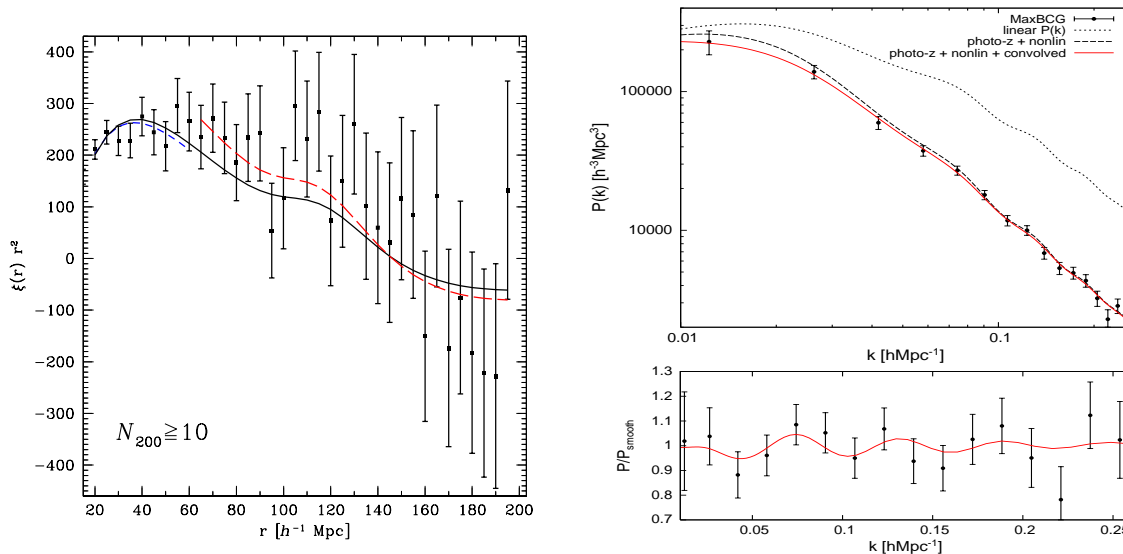
Figure 1.9: *left panel*: 2PCF of the MaxBCG sample obtained by Estrada, Sefusatti, and Frieman (2009). *Right panel:* the power spectrum of the same sample shown in the left panel, from the analysis of Hütsi (2010).

cluster sample from WHL09 Wen, Han, and Liu (2009), finding the first convincing BAO detection (1.10).

A powerful strategy is to use the 2PCF or power spectrum measurements of galaxy clusters in a joint analysis with mass function and weak lensing measurements (see e.g. Mana et al., 2013; Sartoris et al., 2016, and references therein).

The mass function is the most important cluster cosmology probe. It measures the comoving number density of haloes as a function of mass. It is very sensitive to cosmological parameters (e.g. Ω_Λ and σ_8), as it quantifies the capability of structures to form against the expansion of the Universe. Vikhlinin et al. (2009) and A. Mantz et al. (2010) used the mass function of X-ray selected galaxy clusters to constrain the main cosmological parameters; Rozo et al. (2010) measured the mass function of optically selected galaxy clusters, using the MaxBCG sample compiled by Koester et al. (2007). Constraints from the mass function break some of the degeneracies when combined with other cosmological datasets. For instance, Rozo et al. (2010) constrained $\Omega_M - \sigma_8$ by combining cluster and CMB measurements, showing an increase of precision of a factor of 2. Planck Collaboration et al. (2014c), using the Planck Sunyaev-Zeldovich clusters counts, found a $\sim 2\sigma$ tension with respect to the cosmological constraints coming from early time CMB data; after investigating all of the systematics possibly affecting the measure, they concluded that this could represent a hint for a modification of the standard cosmological paradigm, suggesting the intervention of late-time effects not fully accounted for in the modelling.

Galaxy clusters provide also another cosmological information: the baryon fraction. Due to their high masses, the baryon loss in galaxy clusters is almost negligible; the baryon fraction should then be the cosmological one: $f_{gas} = \Omega_b/\Omega_M$. Gonzalez et al. (2013) constrained this value using a sample of 12 X-ray selected galaxy clusters at
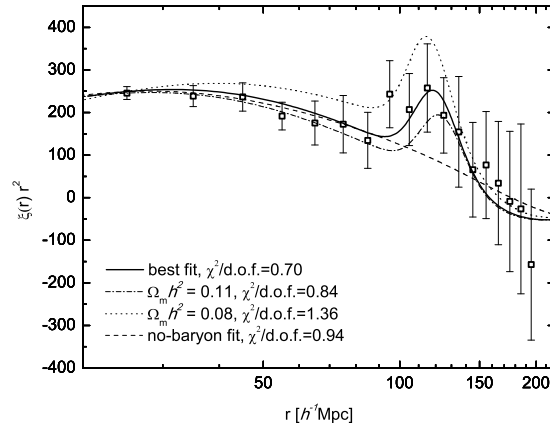
Figure 1.10: 2PCF of 13904 clusters from WHL09 in 18 bins from $20\,\mathrm{Mpc}\,h^{-1}$ to $200\,\mathrm{Mpc}\,h^{-1}$, together with the best-fit model curves with the BAO features (solid line) and without the BAO features (dashed line). (From Hong et al., 2012).

$z \sim 0.1$, finding results consistent with Planck predictions.

Chapter 2

The CosmoBolognaLib

We present the CosmoBolognaLib, a large set of Open Source C++ numerical libraries for cosmological calculations. CosmoBolognaLib is a living project aimed at defining a common numerical environment for cosmological investigations of the large-scale structure of the Universe. In particular, one of the primary focuses of this software is to help in handling astronomical catalogues, both real and simulated, measuring one-point, two-point and three-point statistics in configuration space, and performing cosmological analyses. In this chapter, we will discuss the main features of this software, providing an overview of all the available C++ classes implemented up to now. Both the CosmoBolognaLib and their associated doxygen documentation can be freely downloaded at `https://github.com/federicomarulli/CosmoBolognaLib`. *The description of the code we present in this chapter is based on Marulli, Veropalumbo, and Moresco (2016).*

2.1 Introduction

Numerical tools for cosmological calculations are one of the crucial ingredients in the increasingly ambitious investigations of the large-scale structure of the Universe. Several public libraries for astronomical calculations are nowadays available, in different languages, such as e.g. CfunBASE (Taghizadeh-Popp, 2010), CosmoPMC (Kilbinger et al., 2011), AstroML (Vanderplas et al., 2012), CUTE (Alonso, 2012), Astropy (Astropy Collaboration et al., 2013), Cosmo++ (Aslanyan, 2014), CosmoloPy[1], NumCosmo (Dias Pinto Viteni and Penna-Lima, 2014), TreeCorr (Jarvis, 2015).

Aiming at defining a common environment for handling extragalactic source catalogues, performing statistical analyses and extracting cosmological constraints, we implemented a large set of C++ libraries, called CosmoBolognaLib (hereafter CBL), specifically focused on numerical computations for cosmology, thus complementing the available software. In particular, the CBL provide highly optimised algorithms to measure 2PCF and three-point correlation functions (3PCF), exploiting a specifically designed parallel chain-mesh algorithm to count pairs and triplets. Several types of correlation functions can be computed, such as the angle-averaged 2PCF, the 2D 2PCF in both Cartesian and polar coordinates and its multipole moments, the angular, projected and deprojected 2PCF, the clustering wedges, the filtered 2PCF, and the connected and reduced 3PCF (see §2.4.1). Moreover, a large set of methods are provided to construct random catalogues, to estimate errors and to extract cosmological constraints

---

[1]http://roban.github.com/CosmoloPy/

from clustering analyses (see §2.4.3). These features represent the main novelty of the presented libraries. The CBL are fully written in C++. They can be included either in C++ codes or, alternatively, in high-level scripting languages through wrapping.

This effort can be considered as a *living project*, started a few years ago and intended to be continued in the forthcoming years. The following is the list of scientific publications that have been fully or partially performed using the presented libraries: Marulli, Baldi, and Moscardini (2012) and Marulli et al. (2011, 2012, 2013, 2015), Giocoli et al. (2013), Villaescusa-Navarro et al. (2014), Moresco et al. (2014, 2016), Veropalumbo et al. (2014, 2016), Sereno et al. (2015), Petracca et al. (2016), Cucciati et al. (2016). Thanks mainly to the adopted object-oriented programming technique, the CBL are flexible enough to be significantly extented.

In this chapter, we present the main features of the current version of the CBL, that is fully publicly available[2], together with the documentation obtained with doxygen[3]. A set of sample codes, that explain how to use these libraries in either C++ or Python software, is provided at the same webpage.

The paper is organised as follows. In § 2.2 we will describe the CBL class for cosmological computations. In § 2.3 we will present the classes implemented for handling catalogues of extragalactic sources. 2PCF and 3PCF can be measured and modelled with specific classes that will be described in § 2.4. § 2.5 presents the CBL methods for statistical analyses. In § 2.5 we will provide a brief description of the other CBL functions used for several generic calculations.

2.2   Cosmology

The CBL provide a versatile implementation of different cosmological models. The list of customizable parameters is the following: the matter density, that is the sum of the density of baryons, CDM and massive neutrinos (in units of the critical density) at z=0, Ω_{matter}; the density of baryons at z=0, Ω_{baryon}; the density of massive neutrinos at z=0, Ω_{ν}; the effective number of relativistic degrees of freedom, N_{eff}; the number of massive neutrino species; the density of dark energy at z=0, Ω_{DE}; the density of radiation at z=0, $\Omega_{\mathrm{radiation}}$; the Hubble parameter, $h = H_0/100$; the initial scalar amplitude of the power spectrum, A_s; the primordial spectral index, n_{spec}; the CPL parameters of the DE equation of state (Eq. (1.13); Chevallier and Polarski, 2001; Linder and Jenkins, 2003), w_0 and w_a; the non-Gaussian amplitude, f_{NL}; the non-Gaussian shape – local, equilateral, enfolded, orthogonal (Fedeli et al., 2011); the model used to compute distances (used only for some specific interacting DE models, see Marulli, Baldi, and Moscardini 2012); a variable called *unit*, used to choose between physical units or cosmological units (that is in unit of h). If the above parameters are not specified when creating an object of this class, default values from Planck cosmology will be used

---

[2] https://github.com/federicomarulli/CosmoBolognaLib and
http://apps.difa.unibo.it/files/people/federico.marulli3
[3] www.doxygen.org

(Planck Collaboration et al., 2014b). In any case, each cosmological parameter can be set individually, when required.

Once the cosmological model has been chosen by setting the parameters described above, a large set of cosmological functions can then be used. We provide here a brief overview of the main functions of the class. The full explanation of the whole set of class members can be found in the DOXYGEN documentation at the CBL webpage.

Several functions are available to estimate the redshift evolution of all the relevant cosmological parameters, to compute the lookback and cosmic times, to estimate cosmological distances and volumes, and to convert redshifts into comoving distances and viceversa.

There are methods to estimate the number density and mass function of DM haloes (see § 1.3.2). Specifically, the code implements the equations to compute the halo mass function (Eq. (1.39)) : at the moment, the implemented mass function models are the following: Angulo et al. (2012), Jenkins et al. (2001), Pan (2007), Press and Schechter (1974), Reed et al. (2007), Shen et al. (2006), Sheth and Tormen (1999), J. Tinker et al. (2008), and Warren et al. (2006).

Methods to estimate the effective linear bias of DM haloes are provided as well (Eq. (1.46)). The available parameterisations are: Sheth, Mo, and Tormen (2001), Sheth and Tormen (1999), and J. L. Tinker et al. (2010).

A large set of functions is provided to estimate the real-space and redshift-space power spectra and 2PCF. To estimate the DM power spectrum and all the derived quantities, such as the mass variance used to compute the mass function and bias, the user can choose between one of the following external codes: CAMB (Lewis, Challinor, and Lasenby, 2000), MPTbreeze (Crocce, Scoccimarro, and Bernardeau, 2012), CLASS (Blas, Lesgourgues, and Tram, 2011; Lesgourgues, 2011), Eisenstein&Hu code (Eisenstein and Hu, 1998, 1999). The latter will be exploited authomatically by the CBL via specific functions used to set the parameter files conveniently. Finally the code implements algorithms to asses the cosmic mass accretion history (Giocoli et al., 2013).

2.3 Catalogues

The CBL can be used to handle samples of astronomical objects, with specific support for different kind of object catalogues: galaxies, clusters of galaxies, voids, DM haloes and generic mock objects. Moreover, the code structure is sufficiently versatile to easily include new objects or to extend the present ones, e.g. by adding new properties. Once the catalogue is created, several operations can be performed, such as estimating the distribution of any property of the object members, dividing the catalogues in sub-samples, or creating a smoothed version of the original catalogue. Moreover, a catalogue can be used to estimate 2PCF and 3PCF (see § 2.4.1), or to assess errors through the jackknife or boostrap techniques (see § 2.4.2). Catalogues can also be added together, or they can be enlarged by adding new single objects.
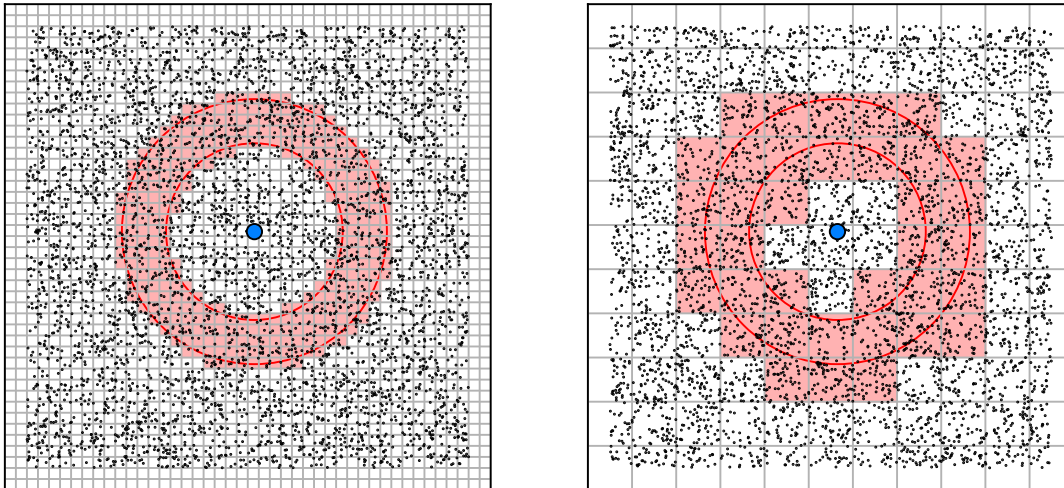
Figure 2.1: illustrative figure of the chain-mesh technique. For a given point, (blue dot) we highlight the pairs falling in the $r - \mathrm{d}r$, $r + \mathrm{d}r$ region (red continuos curves), identified by the algorithm for two different cell sizes (shaded red region), shown in the two panels as an example case.

For a fast spatial search of objects in the catalogues, we implemented a highly optimised chain-mesh method, specifically designed for counting object pairs and triplets in a specified range of scales. The algorithm implements a pixelization scheme, similar to the one described in Alonso (2012). First, the catalogue is divided into cubic cells, and the indexes of all the objects in each cell are stored in vectors. Then, to find all the objects close to a given one, the search is performed only on the cells in the chosen scale range, thus minimising the amount of useless counts of objects at too large separations. In this way, the efficiency of the method depends primarily on the ratio between the scale range of the searching region and the maximum separation between the objects in the catalogue. This is particularly useful when measuring 2PCF and 3PCF (see § 2.4). The chain-mesh method is illustrated in Fig. 2.1. For alternative searching algorithms, such as kd-tree and ball-tree methods, see e.g. Jarvis (2015).

The chain-mesh method is designed to handle chains in 1, 2 and 3 dimensions. An example that shows how to create and use objects of these classes is provided at the CBL webpage.

2.4 Clustering

One of the main focuses of the CBL is to provide functions to measure and model the clustering properties of astronomical sources. In this section, we present a general description of the main features of the current version of CBL methods for clustering analyses.

2.4.1 Measurements

The CBL provide estimators to measures all the following clustering functions:

- the angle-averaged 2PCF, $\xi(r)$ (Eq. (1.62));

- the 2D 2PCF in both Cartesian and polar coordinates (Eq. (1.63));

- the projected 2PCF (Eq. (1.66));

- the deprojected 2PCF(Eq. (1.67));

- the multipole moments of the 2PCF (Eq. (1.64));

- the wedges of the 2PCF (Eq. (1.64));

- the angular 2PCF, $w(\theta)$, where θ is the angular separations.

The CBL provide also methods both to construct random catalogues with different geometries and to read them from files, in case they have been already computed. Specifically, there are functions for both cubic and conic geometries, in order to construct random catalogues both for cubic simulation snapshots, and for mock or real catalogues in light-cones.

Analogously to the 2PCF, the 3PCF can be computed as well. The 3PCF $\zeta(r_{12}, r_{23}, r_{31})$, is defined as $dP_{123} = n^3[1 + \xi(r_{12}) + \xi(r_{23}) + \xi(r_{31}) + \zeta(r_{12}, r_{23}, r_{31})]dV_1 dV_2 dV_3$, where n is the average density of objects, and V_i are comoving volumes. To calculate it the CBL implement the Szapudi and Szalay (1998) estimator:

$$\zeta(r_{12}, r_{23}, r_{31}) = \frac{DDD - 3DDR + 3DRR - RRR}{RRR}, \tag{2.1}$$

where DDD, RRR, DDR, and DRR are the normalised numbers of data triplets, random triplets, data-data-random triplets, and data-random-random triplets, respectively.

The algorithms to measure the above clustering functions use the chain-mesh method described in §2.3. The code exploits also multi-threaded parallelism. Specifically, all the loops to count the number of object pairs and triplets are parallelized via OpenMP[4]. The code performances scale almost linearly with the number of threads.

These functions have been deeply tested with both simulated catalogues (Marulli, Baldi, and Moscardini, 2012; Marulli et al., 2011, 2012, 2015; Moresco et al., 2014; Petracca et al., 2016; Villaescusa-Navarro et al., 2014), and real catalogues of galaxies (Marulli et al., 2013; Moresco et al., 2016) and galaxy clusters (Sereno et al., 2015; Veropalumbo et al., 2014, 2016). Examples can be found at the CBL webpage.

2.4.2 Errors

The CBL provide specific functions to estimate the covariance matrix defined in Eq. (1.68). The latter can be estimated with three alternative methods (see e.g. Norberg et al., 2009):

---

[4] http://openmp.org/wp/

- *analytic errors*: 2PCF errors can be estimated analytically, assuming Poisson statistics. The CBL contain functions to compute analytic errors used to set the diagonal elements of $C_{i,j}$;

- *internal errors*: the CBL provide functions to estimate errors by sub-sampling the data catalogue and measuring the 2PCF for all but one region – *jackknife*, or for a random extraction of regions – *bootstrap*. The volume can be partitioned either in cubic sub-regions, useful e.g. when analysing simulation snapshots, or in sub-regions of generic geometry using the external software MANGLE to reconstruct the angular mask (Swanson et al., 2008);

- *external errors*: the CBL can generate lognormal mock catalogues (Coles and Jones, 1991), with a specified power spectrum, from which the covariance matrix can be estimated.

Analogous methods for the 3PCF will be included in a forthcoming version of the CBL.

2.4.3   Models

The CBL implement the following facilities to model the 2PCF signal:

- the angle-averaged 2PCF of cosmic tracers, $\xi(r)$, can be modelled both in real space and in redshift space. In real space, we implement the model in Eq. (1.52): this is used to measure the bias b or when exploiting the *standard ruler technique* fitting (Veropalumbo et al., 2014). To model the angle-averaged 2PCF in redshift space, we compute the Fourier anti-transform of the damped redshift-space power spectrum. The implement also models for the de-wiggled power spectrum and correlation function (Eq. (1.70)), used to describe the non-linear damping effects at BAO scales. In this case, the dependence on non-linear effects is explicit, via the Σ_{NL} parameter (Eisenstein, Seo, and M. White, 2007).

- the redshift-space 2D 2PCF and its multipole moments can be modelled via the so-called *dispersion model*, that is currently implemented for both the linear and non-linear regimes (Eqs. (1.76)-(1.83)). Both exponential and Gaussian functions can be used to model the distribution function $f(v)$ (see e.g. Marulli et al., 2012). More accurate models for RSD will be included in a forthcoming version of the CBL.

- the projected 2PCF is modelled using Eq. (1.69).

Methods to model the angular 2PCF and the 3PCF are not yet available and will be added in a future version of the CBL.

2.5 Tools for statistical analyses

We implemented generic classes to model measured quantities and derive cosmological constraints. Input data and models are fully customizable. The CBL provide also Bayesian inference methods based on the Bayes' theorem (Eq. (1.84)). In particular, they provide CBL provide methods to perform the MCMC ikelihood sampling technique. The latter consists in sampling a target distribution using a correlated random walk: every step is extracted after a trial that depends only on the previous one (Markov process). The steps are collected in chains, that define marginalised posterior probability of the model parameters $p(\vec{\theta} \,|\, \vec{X})$. We implemented two MCMC algorithms:

- the Metropolis-Hastings algorithm (Hastings, 1970). It consists of a single-particle sampling of the parameter space. At each step, t, the proposed parameter vector, $\vec{\theta}'$, is extracted from the distribution $q(\vec{\theta}'|\vec{\theta}(t))$, centered on $\vec{\theta}(t)$;

- the stretch-move algorithm (Goodman and Weare, 2010). It represents a multi-particle approach. At each step, t, the proposed position $\vec{\theta}'_i$ for the $i-th$ particle is located on the line connecting $\vec{\theta}_i(t)$ and $\vec{\theta}_j(t)$, where the latter is randomly extracted from the particle ensemble. This allows an exchange of information between particles in the cloud.

The current version of the CBL implements Gaussian priors, though minor modifications are required to include different parameterisations. Examples of scientific results obtained using the implemented Bayes methods are provided e.g. in Veropalumbo et al. (2014, 2016).

2.6 Other functions

In addition to the classes described above, a large set of generic functions are included in the libraries. Among them, the set includes: i) functions of generic use, such as to handle errors and warning messages or endian conversions; ii) functions to manipulate vectors and matrices; iii) functions for statistical analyses; iv) functions to calculate distances; v) special functions (e.g. Legendre polynomials). A full documentation can be found at the CBL webpage.

Chapter 3

Cosmological constraints from a sample of optically selected galaxy clusters

In this chapter we will describe the clustering properties of a spectroscopic sample of 69035 clusters selected from the Sloan Digital Sky Survey. Galaxy clusters, as tracers of massive dark matter haloes, are highly biased structures. The linear bias of the sample considered in this work, that we estimate from the projected correlation function, is $b\,\sigma_8 = 2.00 \pm 0.03$. Thanks to the high signal in the cluster correlation function and to the accurate spectroscopic redshift measurements, we obtained a $\sim 4\sigma$ detection of the BAO peak, providing an uncalibrated distance estimate $D_v/r_s = 9.58\pm^{0.22}_{0.24}$, and a calibrated distance $D_v = 989\pm^{22}_{25}$ Mpc h^{-1} by combining with sound horizon from CMB data. The results are robust and insensitive to the reconstruction technique. We model the monopole full shape, finding $\Omega_M h^2 = 0.116\pm^{0.010}_{0.009}$. The measurement presented in this work thus provides a new strong confirmation of the concordance cosmological model and demonstrates the power and promise of galaxy clusters as key probes for cosmological applications based on large scale structures. This work expands the analysis presented in Veropalumbo et al. (2014), updating the dataset and modelling techniques.

3.1   Introduction

In this chapter we investigate the possibility of using clustering of clusters as a cosmological probe. The chapter is organized as follows. In § 3.2 we will describe the cluster sample used in this analysis. We will describe the clustering measures and covariance matrix estimates in § 3.3 and 3.4 respectively. We will provide results on the sample bias in 3.5, on the BAO detection in§ 3.6, on the cosmological constraints from the monopole modelling in § 3.7 and on small scale clustering in § 3.8. In § 3.9, we will compare our results with expected features of cluster clustering, focusing in particular on the BAO detectability.

3.2   Data

The catalogue analysed in this chapter consists of optically selected clusters of galaxies that have identified by Wen, Han, and Liu (2012, WHL12) [1] from the Sloan Digital Sky Survey III (Aihara et al., 2011, SDSS-III, Data Release 8) .

The WHL12 catalogue consists of 132683 galaxy clusters on a sky area of ~ 15000 square degrees, spanning a redshift range $0.05 < z < 0.8$. The cluster identification is based on a friends-of-friends procedure (Huchra and Geller, 1982). This approach has been already exploited to find groups and clusters, using volume-limited spectroscopic samples of galaxies (see e.g. Berlind et al., 2006; Tempel et al., 2014), at low redshift ($z < 0.2$). The WHL12 cluster sample extends the technique on photometric redshift samples of galaxies, allowing the detection of over-densities of galaxies around the Brightest Cluster Galaxy (BCG) at higher redshift.

The optical richness is defined as $R_{L_*} = \tilde{L}_{200}/L_*$, where $\tilde{L}_{200}$ is the total r-band luminosity within an empirically determined radius $\tilde{r}_{200}$ and L_* is the evolved characteristic galaxy luminosity (Blanton et al., 2003). N_{200} is the number of member candidates within $\tilde{r}_{200}$. The subscript 200 denotes quantities measured in a sphere whose mean density is 200 times the critical density at the halo redshift. The cluster photometric redshift reported in the catalogue is the median value of the photometric redshifts of the galaxy members. A candidate cluster is included in the catalogue if $R_{L_*} \geq 12$ and $N_{200} \geq 8$. These thresholds correspond to a mass of $\sim 0.6 \times 10^{14} M_\odot$ (WHL12 Covone et al., 2014).

According to WHL12, the sample is complete for $M_{200} \gtrsim 2 \cdot 10^{14} M_\odot$ in the redshift range $0.1 < z < 0.42$, while the detection rate decreases down to $\sim 75\%$ for the minimum mass of the sample, $M_{200} = 6 \cdot 10^{13} M_\odot$ (see WHL12 for more details on the detection algorithm adopted). WHL12 also quantified the false cluster detection to be at the level of 6% for $R_{L_*} = 12$, decreasing to $< 1\%$ for cluster of richness $R_{L_*} \geq 23$.

3.2.1   Building the spectroscopic cluster sample

A precise estimate of the redshift is crucial when reconstructing statistical properties of the large-scale distribution of matter. Large redshift errors, as in photometric redshift surveys, lead to severe distortion effects that reflect in the 2PCF measurement, complicating its analysis and cosmological interpretation (see e.g. Marulli et al., 2012; Sereno and Ettori, 2014). In order to construct spectroscopic cluster samples, we take advantage of the spectroscopic data from the SDSS. focusing on the SDSS DR7 (Abazajian et al., 2009) and on the final spectroscopic data release from BOSS (Alam et al., 2015; Dawson et al., 2013), part of the SDSS III program. This survey measured the spectra for millions of galaxies. We assign redshift to WHL12 clusters by cross-matching with the spectroscopic galaxy sample [2]. The total cluster sample with spectroscopic information is made of 72518 objects, spanning a redshift range $0 \lesssim z \lesssim 1$. We cut the sample using

---

[1] The latest version of the WHL12 catalogue *cluster_dr9sz.dat* is publicly available at http://zmtt.bao.ac.cn/galaxy_clusters/.

[2] The match has been done using th OBJID entry.
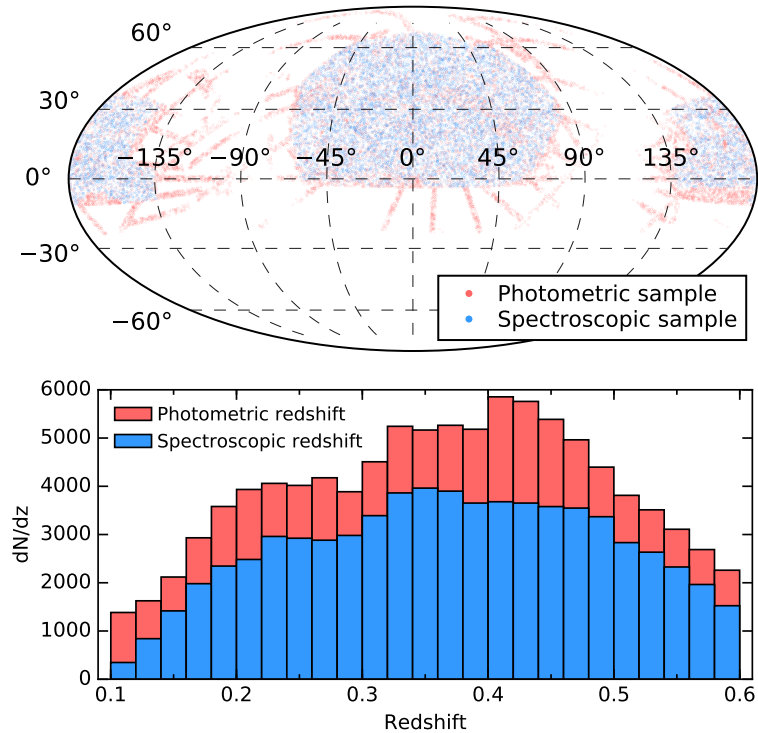
Figure 3.1: *Left Panel.* Angular distribution of the WHL12 sample. In red all the clusters in the sample, in blue only the cluster whose BCG has a redshift in the $0.1 < z < 0.6$ range. *Right Panel.* Redshift distribution of clusters with photometric (in red) and spectroscopic (blue) redshift in the range $0.1 < z < 0.6$. Only clusters in the BOSS window are considered here. Nearly 70% of clusters have a BCG with spectroscopic information.

only those clusters with a spectroscopic redshift in the range $0.1 \lesssim z \lesssim 0.6$; the number of remaining BCG is then 69035, with a median redshift of 0.37, covering an area of $\sim 10800 \deg^2$.

The top panel of Fig. 3.1 shows the angular distribution of photometric and spectroscopic cluster samples (red and blue dots respectively); the bottom panel shows the redshift distribution of the same samples.

Hereafter, we make no distinction between galaxy clusters and BCGs because, by construction, the position of each cluster is entirely determined by the coordinates of its BCG. Clusters with no spectroscopic information for their BCG are discarded, even in the case that members galaxies have a measured spectroscopic redshift. We made this choice to reduce contamination from non linear dynamics in virialized haloes.

3.3 Clustering Measure

In this section, we will recall the basics of the clustering measure technique, applied for this case of study. More information on clustering measures can be found in § 1.5.4.

We choose to measure clustering in configuration space, measuring the 2PCF. According to its definition (Eq. 1.62), it quantifies the excess or defect of probability of finding pairs separated by a certain comoving distance Δr, with respect to a random distribution of points. From a practical point of view, the only operation needed is the computation of numbers of data-data, random-random, data-random pairs in bins of physical separation. A fiducial cosmology must be assumed to convert observed coordinates into comoving coordinates. In this work the fiducial cosmology is a ΛCDM model with $\Omega_M = 0.3$, $h = 0.7$. All the measurements have been performed with the CBL software (§ 2 Marulli, Veropalumbo, and Moresco, 2016).

3.3.1 Weights

We apply a weight to each cluster to correct for mass and redshift incompleteness (see WHL12 for further details). We take into account the dependence on seeing and stellar density of targets on the celestial sphere, as introduced in Anderson et al. (2012), to obtain a more consistent estimate of the 2PCF at large scales. This weighting scheme lowers the 2PCF normalization by $< 10\%$. Thus, it can be considered as a minor effect considering the 2PCF uncertainties at the BAO scales, and does not impact peak determination.

3.3.2 Random Sample

According to the Eq. (1.62), a random sample has to be provided to evaluate the 2PCF taking into account geometrical selection effects. A random catalogue contains in fact the information on the selection function of the data sample, that are used to balance spurious effects affecting the pair counting. The selection function can be safely reproduced by separating it into the angular and radial parts. We generate random catalogues almost 20 times larger than the reference cluster samples to limit shot noise effects.

We generate random points using publicly available survey footprints for the BOSS survey [3] and the MANGLE software (Swanson et al., 2008). We mask the random points falling in the veto regions, as done for the data. We consider two methods to assign redshifts to the random collection of objects:

- random extraction from the smoothed redshift distribution; the parameters involved are the size of the redshift bin and the size of the Gaussian kernel;

- random shuffling the galaxy cluster redshifts (see Ross et al., 2012); a redshift is extracted from the data and assigned to a point in the random sample.

We verified that all the results are robust independently of the method and parameters adopted. In the following, we will show the results obtained with the first method, grouping the cluster redshift distribution in 100 bins and smoothing with a Gaussian kernel three times larger than the bin size.

---

[3] the mask is available at footprint is available at http://data.sdss3.org/sas/dr9/boss/lss/.

3.4 Covariance matrix

We estimate the covariance of the 2PCF measurements via internal estimator techniques. In particular, we choose the jackknife resampling technique; we recall the covariance matrix equation, already introduced in § 1.5.4:

$$C_{ij} \; = \; \frac{N_{sub} - 1}{N_{sub}} \sum_{k=1}^{N} (\xi_i^k - \bar{\xi}_i)(\xi_j^k - \bar{\xi}_j) \, , \tag{3.1}$$

where the subscripts i and j refers to the spatial bins of the 2PCF and k refers to the 2PCF of the kth of N sub-samples; for the jackknife this consist in the whole sample except for the kth region. Finally $\hat{\xi}$ is the mean 2PCF of the N realizations.

We divide the sample in 100 subregions, keeping the number of object per region constant. As verified directly, the value of N_{sub} adopted here is large enough to assure the convergence of the results and at the same time to keep size of regions large enough compared to the scales considered (see e.g. Beutler et al., 2011). In the left panel of Fig. 3.2 we compare the diagonal elements of the two matrices. The jackknife error estimate at separations larger than $50 \, \mathrm{Mpc} \, h^{-1}$ are a factor $\sim \sqrt{2}$ larger to the analytic ones. This result is consistent with expected errors obtained directly from mocks. We extensively test the jackknife algorithm exploited in this work using the LasDamas mock catalogues (McBride et al., 2009), finding that the quoted errors are conservative estimates. In the right panel of Fig. 3.2 we show the correlation matrix from the jackknife compared to the one obtained with the Gaussian analytic model presented by Grieb et al. (2016). The jackknife estimate of the covariance is very scattered, as also expected. This scatter propagates into the likelihood and on the final posterior probabilities of the parameters. Anyway we do not consider in this work corrections to these effects.

3.5 Cluster bias

We use the projected correlation function to estimate the linear bias, b, of the galaxy clusters used in this sample, following the procedure described in § 1.6.1. Thanks to the large signal at small separation, we measure the projected correlation function in comoving radial bins of $2 \, \mathrm{Mpc} \, h^{-1}$, testing several values of π_{max} used to perform the line-of-sight integration. In particular, we considered the range $20 \, \mathrm{Mpc} \, h^{-1} \leq \pi_{max} \leq 90 \, \mathrm{Mpc} \, h^{-1}$. The projected correlation function covariance is obtained via jackknife resampling of 100 angular regions, as specified in § 3.4. We assume different values of Ω_M when computing the projected correlation function model. In Fig. 3.3, left panel, we show the projected correlation function, obtained for $\pi_{max} = 50 \, \mathrm{Mpc} \, h^{-1}$ (black dots), and the best fit models for three different values of Ω_M, $\Omega_M = 0.25$ (dashed red line), $\Omega_M = 0.3$ (blue continuos line), $\Omega_M = 0.35$ (green dot-dashed line).
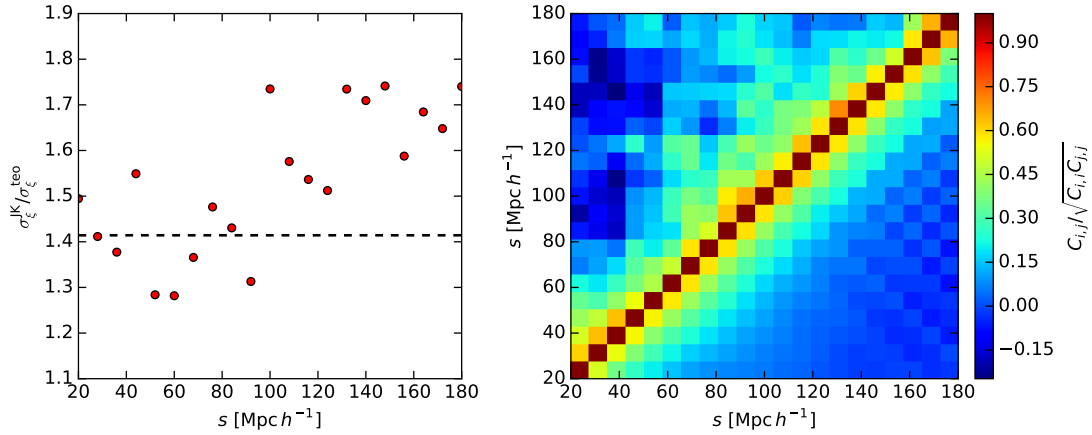
Figure 3.2: *Left panel*: comparison of the monopole errors computed with Jackknife and with theoretical prescription. The jackknife error results to be a factor $\sim \sqrt{2}$ larger at scales larger than $50\,\mathrm{Mpc}\,h^{-1}$, making our final constraints conservative. *Right Panel*: correlation matrix of the 2PCF monopole, as obtained via the jackknife resampling (upper diagonal elements) and with the analytic Gaussian formula (Eq (3.5)). The jackknife correlation results noisy; this effect propagates on the parameter posteriors, increasing the parameter variance.

We find $b\sigma_8 = 2.03 \pm 0.03$ for $\Omega_M = 0.25$, $b\sigma_8 = 2.27 \pm 0.03$ for $\Omega_M = 0.30$ and $b\sigma_8 = 2.48 \pm 0.04$ for $\Omega_M = 0.35$. The fit has been performed in the range $10\,\mathrm{Mpc}\,h^{-1} < r_p < 35\,\mathrm{Mpc}\,h^{-1}$.

The right panel of Fig. 3.3 shows the values of the bias for different values of π_{max}. The results are very stable with respect to this parameter. The main effect is a slight increase in the bias error ($\sim 10\%$) when going to high values of π_{max}. This is due to the fact that signal at large separation along the line of sight add noise to the estimate of the projected correlation function, that propagates into the bias measure. Changing the fit boundaries does not effect significantly the constrained value of $b\sigma 8$

This demonstrates that the cluster selection adopted in this work provides a sample of high biased tracers as expected, with values of the bias compatible with expectation from the cluster masses in the sample. Anyway this match has no statistical significance. We plan to quantify the impact of cluster richness information on the clustering measurements in a future work.

3.6 Baryon acoustic oscillations

We look at the BAO peak in the clustering of galaxy clusters, measuring the monopole of the 2PCF using the LS estimator (Landy and Szalay, 1993), in bins of $\Delta s = 8\,\mathrm{Mpc}\,h^{-1}$. We constrain the BAO peak applying the model described in § 1.6.2, and deriving marginalized constraints on the parameter using a MCMC approach, sampling the Gaussian likelihood function described by Eq. 1.85. For the 2PCF monopole we use the de-wiggle template described in Eq. 1.70: It models the shape of the correlation
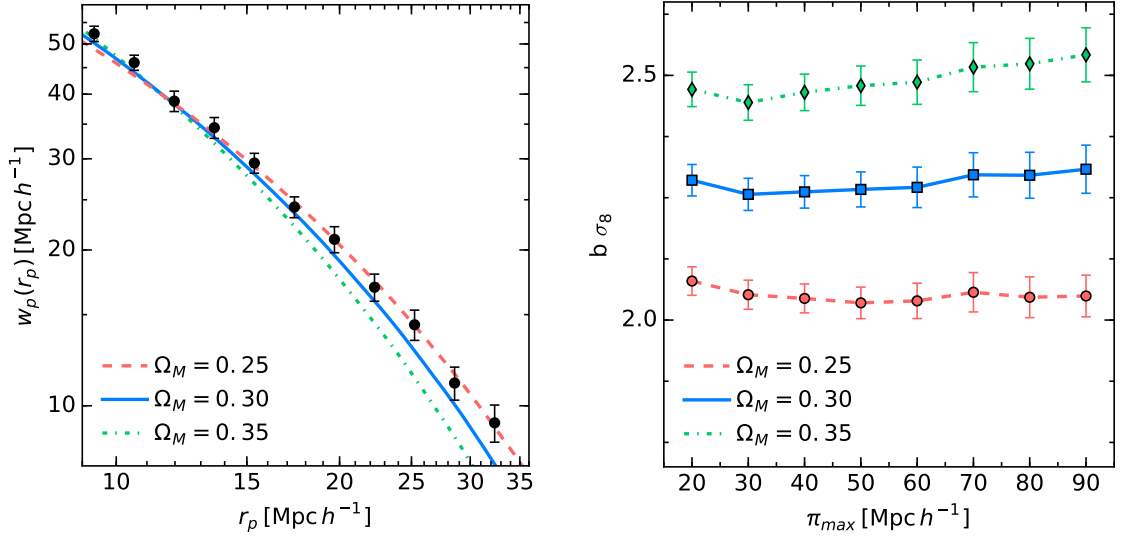
Figure 3.3: *Left panel.*Projected correlation function for the galaxy cluster sample (black points). Here are shown best fit model for $\Omega_M = 0.25$ (red dashed line), $\Omega_M = 0.3$ (blue line) and $\Omega_M = 0.35$ (green dot-dashed line), for $\pi_{max} = 50\,\mathrm{Mpc}\,h^{-1}$. The model with $\Omega_M = 0.25$ seems slightly preferred, by looking at χ^2 residuals. Geometrical distortions only have a little impact on the results . Anyway no conclusion on cosmological parameters should be drawn as geometrical distortions are not taken into account in the model. For this reason we took as our reference $b\sigma_8 = 2.27 \pm 0.03$, obtained for $\pi_{max} = 50\,\mathrm{Mpc}\,h^{-1}$ and $\Omega_M = 0.3$. *Right panel.* Bias as a function of π_{max} for different values of Ω_M. There is a clear difference in $b\sigma_8$ varying Ω_M; on the other hand the model is almost insensitive to different values of π_{max}, this demonstrates the robustness of this method in alleviating redshift space distortion effects.

function with a bias factor B and polynomial terms $\frac{A_0}{r^2} + \frac{A_1}{r} + A_2$, aimed at constrain the small-scales non linear effects as well as large-scales systematics not fully accounted for in the random. The BAO peak is modelled by an extra-parameter, Σ_{NL}, that describes its shape.This parameter is kept fixed in the analysis. The only parameter of the model of cosmological interest is then α, that measure the shift of the BAO peak with respect to the position predicted by the fiducial model, and provides the distance information, as Eq. 1.72 shows. The median redshit of the sample is $\bar{z} = 0.37$. Using this approach the true value of the sound horizon should be known a priori. For this analysis we use $r_s = 147.34 \pm 0.65\,\mathrm{Mpc}$ from Planck Collaboration et al., 2014b. The alternative approach is to not assume any value for this quantity, providing the *un*calibrated distance $D_V/r_s = \alpha D_V^{fid}(\bar{z})/r_s^{fid}$. For the fiducial cosmology assumed here, $D_V^{fid}(0.37) = 980.6\,\mathrm{Mpc}\,h^{-1}$ and $r_s^{fid} = 145.7\,\mathrm{Mpc}$.

The BAO peak is very clearly detected; we find the distance $D_v = 968\pm^{23}_{25}\,\mathrm{Mpc}\,h^{-1}$, and its uncalibrated version $D_v/r_s = 9.38\pm^{0.22}_{0.24}$, corresponding to a 2.5% distance error. This is a great result, that demonstrates that the BAO signal can be easily detected also from galaxy clusters. It is worth to be noticed that our covariance matrix estimate is
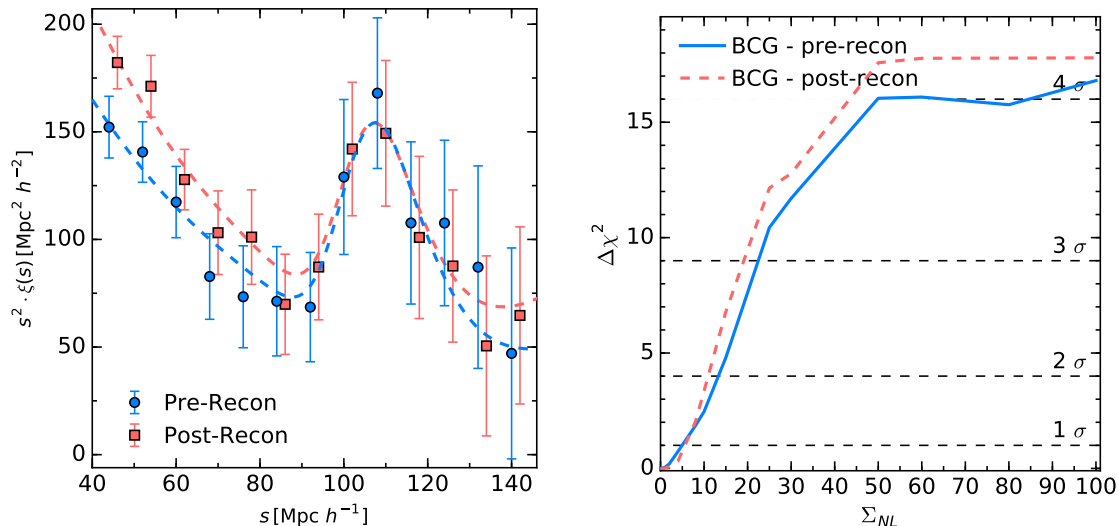
Figure 3.4: *Left panel*: the monopole of the 2PCF of the galaxy clusters sample, before (blue circles) and after(red squares) reconstruction. The best-fit models from the fitting procedure described in § 3.6 are also shown, blue dashed line for the pre-reconstruction fit and red dashed line for the post-reconstruction respectively. For galaxy cluster, the BAO signal does not improve significantly after the reconstruction is applied. *Right panel:* The values of $\Delta\chi^2$ as a function of Σ_{NL}. The values span from a linear power spectrum ($\Sigma_{NL} = 0 \ \mathrm{Mpc}\,h^{-1}$) to a power spectrum model with no BAO ($\Sigma_{NL} \to \infty$). Detections of the BAO is 4σ. The shape of the peak is consistent with linear theory, considering the error estimates from our clustering measurements.

conservative, and so is our estimate of the distance. We test the impact of different choices for the binning and for the fitting ranges, finding that the results are robust with respect to these choices. Hong, Han, and Wen (2016) recently detected the BAO from the same sample of galaxy clusters finding a comparable result.

We also reconstruct the galaxy clusters density field using the Zel'dovich approximation, following the procedure described in § 1.5.4. The goal of the reconstruction is to *reverse* non-linear growth of structures, by moving haloes to their position and thus shrinking the BAO peak to a shape closer to the one predicted by linear theory. For this case we find the distance $D_v = 989\pm^{22}_{25} \ \mathrm{Mpc}\,h^{-1}$, and the uncalibrated distance $D_v/r_s = 9.58\pm^{0.22}_{0.24}$. The results for the two case are very well compatible, and in perfect agreement with prediction for ΛCDM cosmology. Moreover, no improvement comes from applying this technique considering the error estimates, differently from the case of galaxy clustering, where a strong improvement on BAO peak detection comes after reconstruction is applied (Anderson et al., 2012).

In the left panel of figure 3.4 we show the monopole of the cluster correlation function before (blue circles) and after reconstruction (red squares).

This is made clear by looking at the shape of the BAO peak. In the right panel of figure 3.4 we show the $\Delta\chi^2$ value for the model described in Eq. 1.70 as a function of Σ_{NL}. As already discussed in § 1.6.2, Σ_{NL} describes the damping of the BAO caused

by the non linear growth. A null value of this parameter means that the BAO shape is described by linear theory; with $\Sigma_{NL} \to \infty$ the BAO signal is completely dumped. The best fit value of Σ_{NL} is $0 \, \mathrm{Mpc} \, h^{-1}$ both before *and* after reconstruction, suggesting that the density field probed by large collapsed structure is negligibly influenced by non-linear growth. This makes the application of reconstruction procedure unnecessary considering the actual measurements uncertainties. Similar results have been obtained by Prada et al., 2016; Sánchez, Baugh, and Angulo, 2008; Wang and Zhan, 2013 who analysed the shape of the BAO feature in bias-dependent study of the correlation function, finding that a shaper BAO peak is detected from more massive haloes. The results are robust for changing in the reconstruction parameters; that is the sample bias and the smoothing parameters. This also implies that galaxy clusters show a very sharp and strong BAO signal, detected at a very high significance despite the paucity of the sample (detection $> 4\sigma$).

3.7 Constraints from the monopole full shape

In order to infer more information from the clustering signal, we also choose to model the full shape of the 2PCF pre-reconstructed monopole in redshift space; this allows to combine the geometrical information coming from the BAO peak, with the information coming from the clustering shape. This method has already been used in previous galaxy clustering works (see e.g. Beutler et al., 2011; Blake et al., 2011; Eisenstein et al., 2005), as well as for smaller sub-sample of galaxy clusters (Hong et al., 2012; Veropalumbo et al., 2014).

We consider a theoretical model that includes both the cluster bias and the effects of RSD and geometric distortions due to a possible incorrect assumption of the fiducial cosmology. The adopted model is the following:

$$\xi_{cl}(s) = b^2 \left(1 + \frac{2}{3}\beta + \frac{1}{5}\beta^2 \right) \xi_{DM}(\alpha s) , \tag{3.2}$$

where b is the linear bias factor, α is the ratio between the test and fiducial values of D_V, used to model geometric distortions, and $\beta = f/b$ is the linear distortion parameter, that is the ratio of the linear growth rate f and the bias b. Based on results showed in the previous section, we use the linear dark matter correlation function, ξ_{DM}, computed using the software CAMB (Lewis and Bridle, 2002).

To compare with previous studies, we derive also other parameters such as $y_s(z) = r_s/D_V(z)$ (see also §1.6.2), and the acoustic parameter $A(z)$, defined as follows:

$$A(z) \equiv \frac{100 D_V(z) \sqrt{\Omega_M h^2}}{cz} . \tag{3.3}$$

Cosmological information are encoded in $\Omega_M h^2$, in the linear bias, b, and in the shift
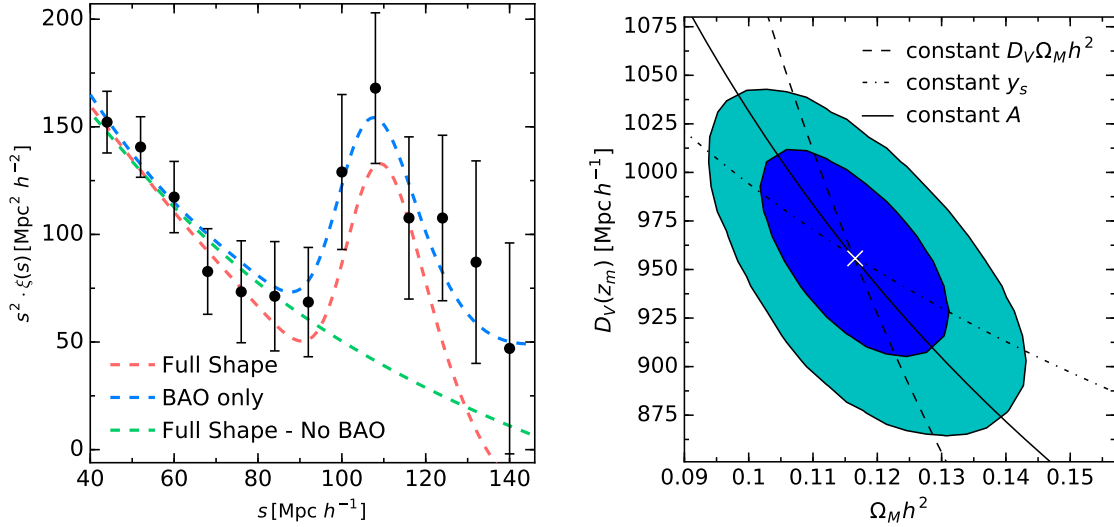
Figure 3.5: *Left panel*: the pre-reconstruction monopole of the 2PCF for the galaxy cluster sample (black dots) described in § 3.3, compared to the best fit full-shape models with and without the BAO feature (red and green dashed curves respectively) and to the best-fit model from § 3.6 locating the BAO position (blue curve). The results of the two methods are in agreement, leading to a similar BAO peak detection. *Right panel:* $1 - 2\sigma$ confidence contours for the parameters $\Omega_M h^2$, $D_V(z = 0.37)$, obtained from the fit of the model given in Eq. (3.2). Following the degeneracies directions, the fit is driven both by the BAO peak geometrical information and by the monopole shape constraints.

parameter, α, that traces the geometrical distortions. All the other cosmological parameters are kept fixed to the Planck values: $H_0 = 67.4 \, \mathrm{km \, s^{-1} \, Mpc^{-1}}$, $\Omega_b = 0.02207 h^2$, $n_s = 0.96$ and $\sigma_8 = 0.83$ (Planck Collaboration et al., 2014b).

The best-fit parameters are summarized in Table 3.1. The reported values are the medians of the MCMC parameter distributions, while the 1σ errors span from the $16th$ to the $84th$ percentiles. The dashed red line in the left panel of Fig. 3.5 shows the result of the fit obtained using the CAMB software to estimate $\xi_{DM}(r)$, while the green one has been obtained using the fitting formula given by Eisenstein and Hu (1999) with no BAO. We show by comparison the best-fit curve from BAO-only model, (see § 3.6). The BAO feature is detected with a $\sim 3.5\sigma$ confidence level, in good agreement with previous results.

We estimate a distance measure of $D_V = 955 \pm^{32}_{34} \, \mathrm{Mpc} \, h^{-1}$. Constraints on the distortion parameters y_s are of the order of 2.6%, in good agreement with the value obtained with the modelling used §3.6. Fitting in the range $20 < s[\mathrm{Mpc} \, h^{-1}] < 180$, we obtain a 8% constraint on the mass density parameter, $\Omega_M h^2 = 0.116 \pm^{0.01}_{0.009}$, after marginalizing over the other two model parameters α and b. This significantly improves the results obtained in Veropalumbo et al., 2014.

The right panel of Fig. 3.5 shows the 1 and 2σ marginalized probability contours in the $\Omega_M h^2 - D_V$ plane. The dotted line indicates the points with constant y_s, i.e. it

represents the degeneracy direction between parameters the that would occur if the fit was driven by the BAO feature only. The dashed line (constant $\Omega_M h^2 D_V$) shows the complementary case in which the fit is driven only by the shape of the 2PCF. As it can be seen, the orientation of the parameter degeneracy obtained in this work lies approximately in the middle between these two extremes, closely following the solid line of constant A (Eq. 3.3). In Table 3.1 we report the best-fit values of the cosmological parameters, as well as the estimated uncertainties derived from the MCMC analysis after marginalizing over all the free parameters of the fit. As it can be seen, the estimated value of b is consistent with the one derived in § 3.5 by fitting the projected correlation function at smaller scales. Reducing the fitting range has the effect of worsening the constraints: the precision drop of a 30% factor when changing the lower limit of the fit to $40\,\mathrm{Mpc}\,h^{-1}$. Also the degeneracies direction indicates that the fit becomes dominated by the BAO when increasing the lower fit boundary.

3.8 Redshift space distortions

In this section we measure the RSD of the galaxy clusters. The goal is to assess the detectability of the Fingers-of-God signal in the anisotropic clustering of BCGs, to test the hypothesis that I described in § 1.7.1.

To do so, we measure the 2D cartesian 2PCF $\xi(r_p, \pi)$ for the galaxy cluster sample, up to $r_{max} = 50\,\mathrm{Mpc}\,h^{-1}$, with a bin width of $2\,\mathrm{Mpc}\,h^{-1}$. Figure 3.6 shows the iso-correlation contours of $\xi(r_p, \pi) = \{5, 2, 1, 0.5, 0.3, 0.15\}$. Other approaches consist in measuring multipoles of the anisotropic 2D correlation function, or wedges (see § 1.5.4); we plan to use also these technique in future works. In this case we only consider the diagonal elements of the covariance matrix; this approximation can be considered as a lower limit to the precision on parameters modelling the non-linear small scale signal. We consider the dispersion model (Hamilton, 1992; Kaiser, 1987) to infer the small-scales redshift space distortion signal; the free parameters are the linear growth rate, $f\sigma_8$, the cluster bias, $b\sigma_8$, and the σ_{12}, the parameter tuning the fingers-of-God. This effect enters the model as the convolution of the parallel to the line-of-sight part of the correlation function and a velocity distribution; here we assumed the latter to be an exponential (Eq. (1.83)).

More details on the model are described in § 1.6.3. The best fit results are shown in Figure 3.6; we show the models with the values of σ_{12} both free (blue dashed line) and fixed to 0 (red dashed line), plotted at same iso-correlation levels as for the data. Constraints on σ_{12} are very weak; from the marginalized posterior $\sigma_{12} = 430\pm_{250}^{370}$. This suggests a $< 2\sigma$ detection of the fingers-of-God signal. The same can be seen by comparing the residuals of the best fit in the two case of free and fixed σ_{12}; with a reduced χ^2 of 1.26 and 1.34 respectively: the difference between the models is almost undetectable. Other best fit model parameter values are: $f\sigma_8(0.37) = 0.33\pm_{0.19}^{0.28}$, $b\sigma_8(0.37) = 2.0\pm_{0.1}^{0.1}$.

Measure	Model	Parameter
$\xi(s)$	BAO only Pre Reconstruction	$D_V = 968\pm^{23}_{25}$ Mpc h^{-1} $D_V(r_s^{fid}/r_s) = 957\pm^{23}_{25}$ Mpc h^{-1} $D_V/r_s = 9.6\pm^{0.2}_{0.2}$
	BAO only Post Reconstruction	$D_V = 989\pm^{22}_{25}$ Mpc h^{-1} $D_V(r_s^{fid}/r_s) = 978\pm^{22}_{25}$ Mpc h^{-1} $D_V/r_s = 9.6\pm^{0.2}_{0.2}$
	Full shape	$\Omega_M h^2 = 0.117\pm^{0.01}_{0.009}$ $D_V(r_s^{fid}/r_s) = 956\pm^{32}_{35}$ Mpc h^{-1} $b\sigma_8 = 2.0\pm^{0.1}_{0.1}$
$w_p(r_p)$	$\Omega_M = 0.25$	$b\sigma_8 = 2.03 \pm 0.03$
	$\Omega_M = 0.30$	$b\sigma_8 = 2.27 \pm 0.03$
	$\Omega_M = 0.35$	$b\sigma_8 = 2.48 \pm 0.04$
$\xi(r_p, \pi)$	Dispersion Model	$f\sigma_8(z) = 0.33\pm^{0.3}_{0.2}$ $b\sigma 8 = 2.0\pm^{0.1}_{0.1}$ $\sigma_{12} = 430\pm^{370}_{250}$ km/s

Table 3.1: Best-fit parameters obtained from modelling the projected, the monopole and the cartesian 2D correlation functions. The median redshift is $z = 0.37$
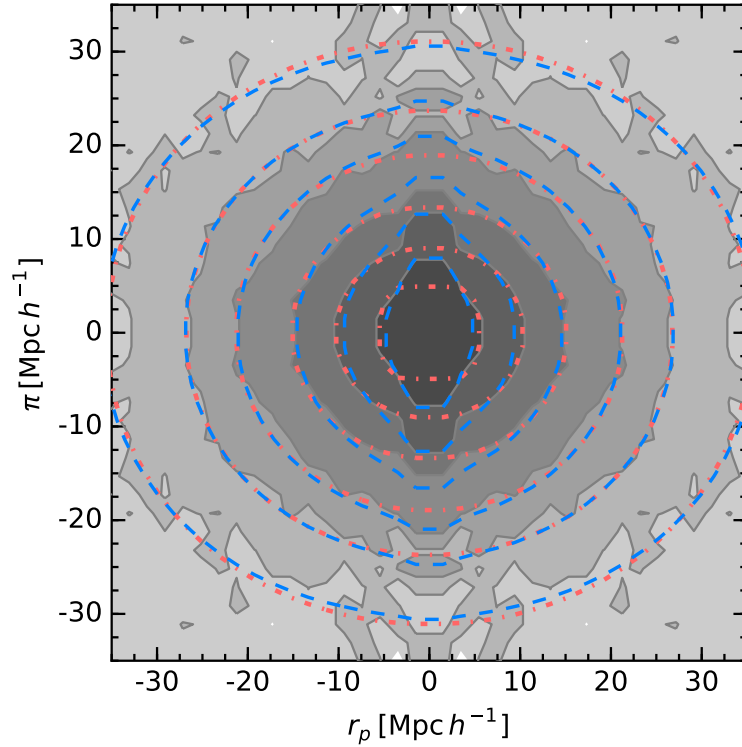
Figure 3.6: The Two-dimensional 2PCF of the galaxy cluster sample. The solid lines show iso-correlation contours at $\xi(r_p, \pi) = \{0.15, 0.3, 0.5, 1, 2, 5\}$. The other lines show the results from the dispersion model are shown, as described in 3.8: the red lines refer to the linear dispersion model, while the blue owes to the non linear model, which includes the Fingers-of-God effect.

3.9 Discussion

The results presented in previous sections showed that galaxy clusters are powerful cosmological probes for the detection of BAO, even with a fairly limited statistics, and highly competitive with respect to galaxies. Future large surveys such as Euclid (Amendola et al., 2013; Laureijs et al., 2011) and eROSITA (Merloni et al., 2012) will allow this approach to be fully exploited in several open key questions (e.g. the dark energy equation of state). Accurate forecasts on the cosmological constraints achievable by these future cluster surveys will be provided in a future work. Moreover, significantly improvements can be made by combining this rich of information statistics with other cosmological probes from galaxy clusters, such as the mass function and stacked gravitational lensing.

In this section we describe the expected cluster clustering signal, focusing in particular on the BAO detection, as a function of the bias and number of haloes, and the influences from small scales non linear dynamics.

3.9.1   Detection of the BAO peak in clustering of haloes

Galaxy clusters are the largest bound structures in the Universe and the more biased tracers of the dark matter density field. Their number density is strictly cosmology dependent, via the mass function expressed in § 1.3.2.

By choosing a mass threshold M_{min} and a volume, Eqs. (1.41), (1.46) provide the total number of haloes N_h and their effective bias b_{eff}. It can be noticed that the for fixed volume, the number of haloes decreases with mass, while b_{eff} increases. It is then clear that both clustering signal and noise change when selecting haloes at different M_{min}. We are interested in understanding the impact of this changes on the BAO detection. To do so, we construct mock monopole signal and covariance starting from three basic quantities: a) the survey volume, V_s, b) the haloes number density $n = N_h/V_s$ and c) the effective bias b_{eff}.

We use the Kaiser model for the monopole obtained from Fourier anti-trasforming the monopole of the anisotropic power spectrum $P(k, \mu)$ (Kaiser, 1987):

$$\xi_0(s) = b_{eff}^2(1 + \frac{2}{3}\beta + \frac{1}{5}\beta^2)\xi_{DM}, \tag{3.4}$$

where β is the ratio of the linear growth rate f and b_{eff}. We model the monopole covariance matrix $C_{i,j}$ following the analytic prescription given by Grieb et al., 2016:

$$C_{i,j} = \frac{1}{2\pi^2} \int_0^\infty k^2 \left[\frac{1}{V_s} \int_{-1}^1 \left[P(k,\mu) + \frac{1}{\bar{n}} \right]^2 d\mu \right] \bar{j}_0(ks_i)\bar{j}_0(ks_j) dk, \tag{3.5}$$

where $\bar{n} = N_h/V_s$.

In order to reproduce the cluster sample we described in § 3.2, we fix a redshift range $0.1 < z < 0.6$, with a median redshift $z = 0.37$ and an area $A \approx 10000 \deg^2$: the total survey model is $V_s \approx 4\mathrm{Gpc}^3 h^{-3}$.

We then compute monopole signal $\xi_0(s)$ and covariance matrices $C_{i,j}$ for combinations of of (N_h, b_{eff}), and constrain the BAO signal using the model described in § 1.6.2.

Results are shown in left panel of Fig. 3.7. The black curve connects pairs $\{N_h, b_{eff}\}$ obtained from Eqs. 1.41, 1.46 using the same M_{min}; the grey area above this line is then a *forbidden* region for these choices of volume and redshift; the white area below the line represents a region in which incomplete halo samples should fall. Red curves correspond to line with same percentage precision for α. Smaller highly biased samples perform severally worse than large samples with smaller clustering signal. Anyway the bias still plays a role as the iso-precision lines are not parallel to the bias axis. These trends are in agreement with results from mock halo catalogues by Angulo et al., 2005.

For the value of the bias and the number of clusters in our sample, the expected BAO precision should be of the order of 1.5%. This confirms that clusters are a very good candidate for BAO analysis. This also confirms that our results are conservatives.

For cluster clustering studies aimed at extracting cosmological information from the BAO feature, it is worth focusing on complete highly biased samples of clusters
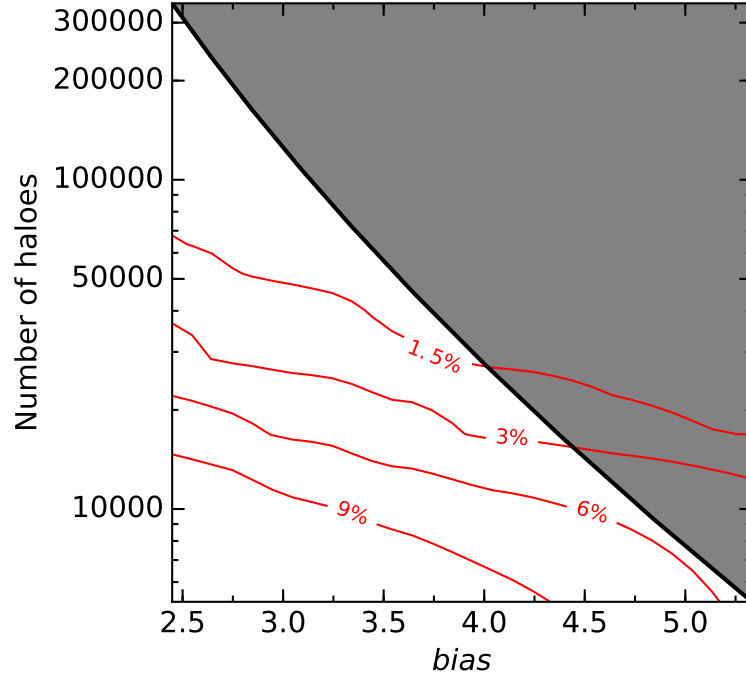
Figure 3.7: Error on α as a function of bias and number of haloes for a fixed choice of volume. Results have been obtained for a mock survey with volume $\sim 4\mathrm{Gpc}^3 h^{-3}$ and $13.5 < \log M_{min} h^{-1} < 14.5$. The black line connect values of $\{N_h, b_{eff}\}$ obtained from Eqs. (1.41), (1.46) with the same M_{min}. Red lines connect instead mock realizations for which the precision on the shift parameter α is $1.5, 3, 6, 9\%$. The number of haloes available is the leading parameter. The bias anyway plays a role helping in detecting BAO feature for sample less populated but with a large clustering signal.

as these can constraint the peak as well as larger but incomplete less-biased samples. Moreover, complete samples are easily to be treated when combined with other probes, such as the mass function; since it help in building a joint mass function-clustering likelihood.

3.9.2   Non linear dynamics

Identifying a galaxy cluster coincides, in principle, with identifying the coordinates of the centre of its potential well. This implies that the redshift of the galaxy cluster should be unaffected by the fingers-of-God effect, the latter coming from random motions of cluster members. This provide a clustering signal not distorted, in particular at the BAO scales since small scales random motions can influence also very large separations. To qualitative look the impact of fingers-of-God on the correlation function, we consider a model from the monopole of the anisotropic power spectrum $P_0(k)$:

$$P_0(k) = \int_0^1 P(k, \mu)\mathrm{d}\mu. \tag{3.6}$$
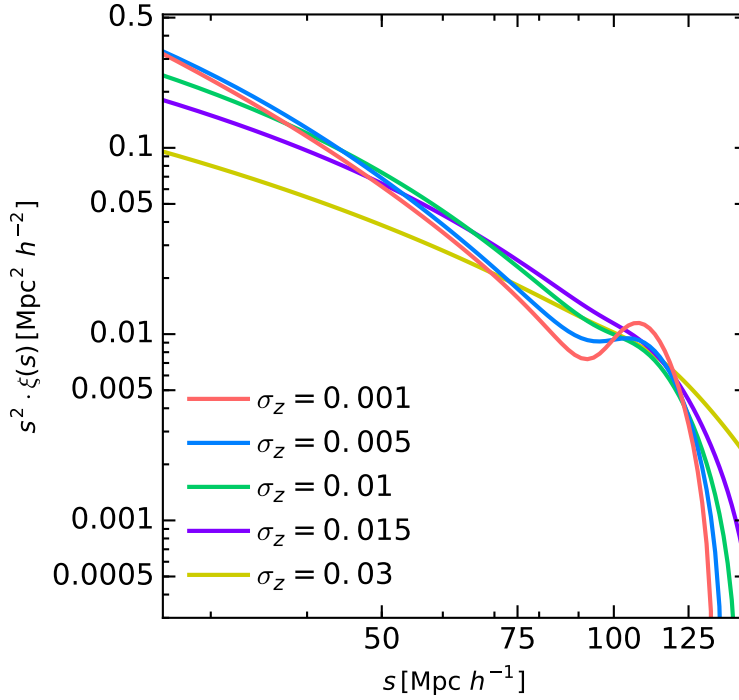
Figure 3.8: Shape of the monopole of the 2PCF for different redshift error. Here we kept fixed the bias $b = 2.5$.

$P(k, mu)$ is modelled using the following prescription:

$$P(k, \mu) = (b + f\mu^2)^2 \exp(-k^2\mu^2\sigma^2)P_{DM}(k), \qquad (3.7)$$

with $P_{DM}(k)$ the matter power spectrum, b the bias, f the linear growth rate and $\exp(-k^2\mu^2\sigma^2)$ the cut-off term describing the random perturbations of the redshifts that wash out the signal over a typical scale $k \sim 1/\sigma$, thus causing a scale-dependent effect. Both non-linear stochastic motions and redshift errors contribute to the value of σ

The right panel of Fig.3.7 shows how the clustering signal is modified when adding non-linear redshift space contributions, here shown as redshift error. In the case of optically selected galaxy clusters structures are detected by looking at galaxy distributions. The most common assumption made in this case is that the cluster centre is occupied by a galaxy often identified as the BCG (e.g. Koester et al., 2007; Wen, Han, and Liu, 2012). It follows that the cluster positions coincides with the coordinates of a sub sample of galaxies, that probe the highest peaks of the density field and with a redshift in principle not affected by Fingers-of-God. However, this selection is very difficult to obtain, for both physical reasons, (clusters can be in unrelaxed dynamical states) and technical reasons, especially when the cluster selection is extended down to low massive, and then poor haloes, where BCG can easily be misidentified. Anyway the analysis of samples of galaxy clusters detected in different ways is beyond the scope of this thesis and will be part of a future analysis.

Chapter 4

Distance-redshift relation from galaxy clusters BAO detection

After providing in § 3 a BAO detection for the whole cluster sample, in this chapter we will provide observational constraints on the distance-redshift relation from BAO as detected from the monopole of the 2PCF of galaxy clusters. The cluster samples considered in this work have been extracted from the SDSS III in three redshifts bins, ($\bar{z} = 0.2$, $\bar{z} = 0.3$, and $\bar{z} = 0.5$). The number of objects is 12910, 42215, and 11816, respectively. We detect the peak of BAO for all the three samples. The derived distance constraints are: $r_s/D_V(z = 0.2) = 0.18 \pm 0.01$, $r_s/D_V(z = 0.3) = 0.124 \pm 0.004$ and $r_s/D_V(z = 0.5) = 0.080 \pm 0.002$. Combining these measurements with the sound horizon scale measured from the CMB, we obtain robust constraints on cosmological parameters. The results are in agreement with the standard ΛCDM. These results have been published in Veropalumbo et al. (2016).

4.1 Introduction

Galaxy clusters reveal to be a suitable tracer for the matter distribution. The main advantages in using these objects in a clustering analysis have been described and demonstrated in § 3: clusters have a large clustering signal, due to high bias and a very negligible contribution from RSD. Moreover, the BAO signal detected from the cluster clustering is compatible with prediction from linear theory, and BAO reconstruction methods are not required to improve the signal. All this aspects counterbalance the larger measurements uncertainties on clustering estimates compared to galaxies, coming from the fact that massive haloes are limited in numbers for a fixed volume.

The main goal of this chapter is to obtain a multi-redshift distance constraint by measuring the BAO peak in the 2PCF of three spectroscopic samples of galaxy clusters and obtain cosmological constraints from the distance measurements. This allows us to understand the amount of information coming from a purely geometric cosmological probe obtained with this relatively small, but peculiar, collection of objects. This is a part of the general picture, that is using cluster catalogues to perform a joint analysis of the mass function and clustering, to further tighten the cosmological constraints.

The chapter is organised as follows. We will present our cluster samples in § 4.2, and in § 4.3 we will show our results on clustering measurements. We will describe cosmological constraints in § 4.4 Finally, in 4.5 we will compare our results with BAO detection from galaxy surveys .

4.2 Data

This section describes the data used for the clustering analyses. More details on the methods exploited to detect the galaxy clusters and to construct the spectroscopic samples can be found in Wen, Han, and Liu (2012) and are described in § 3.2.

4.2.1 Sample selection

By cross-matching the photometric sample of BCG with the spectroscopic galaxy sample from SDSS DR12 final release, we have ~ 65000 galaxy clusters with a spectrocopic redshift in $0.1 < z < 0.6$.

Thanks to this high abundance , we can split the catalogue in three subsamples at different redshifts, according to the type of target each BCG is assigned in the SDSS program (Anderson et al., 2014; Ross et al., 2015). For details on the targeting selection, we refer to Dawson et al. (2013). We choose this method instead of a simple redshift bin cut of the sample presented in 3.2.1 because before the public release of the combined sample there was no way to create a correct random sample accounting for all the spectroscopic data (Alam et al., 2016). We consider three types of targets: the *Main Galaxy Sample*, formed of luminous galaxies ($r < 17.77$) at $z < 0.3$; the *LOWZ sample*, that targets Luminous Red Galaxies up to a redshift $z < 0.43$; the *CMASS sample*, focused on high-redshift galaxies in the range $0.43 < z < 0.7$; the latter samples are part of the BOSS selection.

The derived spectroscopic cluster catalogues are the following:

- the Main Galaxy Cluster Sample (Main-GCS), consisting of 12910 BCGs, part of the Main Galaxy sample in the north galactic cap;

- the LOWZ Galaxy Cluster Sample (LOWZ-GCG), with 42215 BCGs in the LOWZ sample;

- the CMASS Galaxy Cluster Sample (CMASS-GCS), with 11816 BCGs in the north galactic cap of the CMASS sample.

We restrict the redshift ranges to *i*) $0.1 \leq z \leq 0.3$ for the Main-GCS, *ii*) $0.1 \leq z \leq 0.43$ for the LOWZ-GCS, and *iii*) $0.43 \leq z \leq 0.55$ for the CMASS-GCS. We have chosen the redshift cut at $z = 0.43$ so that the CMASS-GCS and the LOWZ-GCS are independent samples. On the other hand, a significant fraction of clusters is in common between the Main-CGS and the LOWZ-CGS samples. We choose this sample splitting to maximize the number of clusters in each redshift bin and to simplify the creation of random catalogues. We discuss the covariance between samples in § 4.3.2. Table 4.1 reports the main properties of the selected samples, while in Fig. 4.1 we show their angular (upper panels) and redshift distributions (lower panels). We apply the same weighting scheme described in § 3.3.1; this slightly lowers the 2PCF normalization; thus, it can be considered as a minor effect considering the 2PCF uncertainites at the BAO scales.
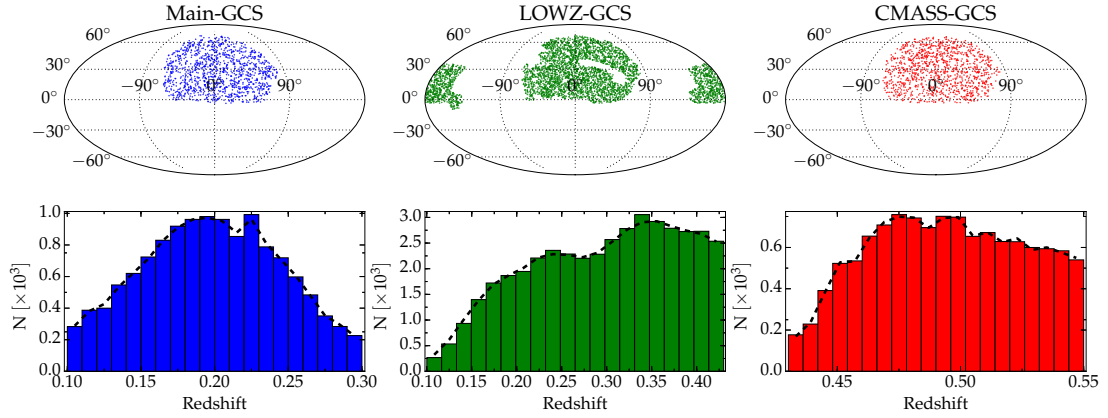
Figure 4.1: The angular (top panels) and redshift distributions (bottom panels) of the three selected galaxy cluster catalogues: Main-GCS (blue), LOWZ-GCS (green) and CMASS-GCS (red). The black dashed curves in the bottom panels are the reconstructed redshift distributions used for the construction of random catalogues.

Sample name	Number of clusters	Redshift range	Median redshift	bias
Main-GCS	12910	$0.1 \leq z \leq 0.3$	0.20	2.00 ± 0.05
LOWZ-GCS	42115	$0.1 \leq z \leq 0.43$	0.30	2.42 ± 0.02
CMASS-GCS	11816	$0.43 \leq z \leq 0.55$	0.50	3.05 ± 0.07

Table 4.1: The main properties of the cluster samples used for the clustering analysis. The bias has been obtained by modelling the projected correlation function in the scale range $5 < r\,[\mathrm{Mpc}\,h^{-1}] < 20$.

4.2.2 Random catalogues

We generate random points using publicly available survey footprints [1] and the MAN-GLE software (Swanson et al., 2008). For the three cluster samples we used the following masks:

- Main-GCS: the SDSS DR7 survey footprint, using the window provided by the NYU Value-Added Galaxy Catalogue (NYU-VAGC) (Blanton et al., 2005), a cross-matched collection of galaxy catalogues aimed at clustering and galaxy formation studies;

- Lowz-GCS: the BOSS survey footprint, excluding regions afflicted by the wrong targeting selections due to slightly different colour cuts assumed (Reid et al., 2016). (these excluded regions are identified via the spectroscopic tiles ID TILEID> 10324);

- CMASS-GCS: the Northern Galactic Cap of BOSS survey footprint.

---

[1] the SDSS DR7 window is available at http://sdss.physics.nyu.edu/vagc/; the BOSS survey footprint is available at http://data.sdss3.org/sas/dr9/boss/lss/.

Random points falling in the veto regions that consider bad photometry and stars are masked, as done for the data.

As already described in § 3.3.2, we assigned redshifts to the random points from a random sampling of the smoothed cluster redshift distribution. We grouped the cluster redshift distribution in 100 bins and smoothed the redshift distribution with a Gaussian kernel three times larger than the bin size. In bottom panels of Fig.4.1 we show the smoothed redshift distribution used in random creation (black dashed lines).

4.2.3   Covariance matrix

To compute the covariance matrix we use both jackknife/bootstrap and lognormal mock samples to compute the covariance matrix, more details are described in § 1.5.4.

We compare the internal error estimates described above with the ones assessed through the lognormal density field technique (Coles and Jones, 1991). This method to infer the covariance matrix has been already used by several authors for clustering analyses (see e.g. Beutler et al., 2011; Blake et al., 2011; Chuang et al., 2015).

We create the density field realizations using the redshift-space monopole model:

$$P_{model}(k) = b^2 \left(1 + \frac{2}{3}\beta + \frac{1}{5}\beta^2 \right) P_{DM}(k) \,, \tag{4.1}$$

where P_{DM} is the linear matter power spectrum obtained with the CAMB software (Lewis and Bridle, 2002), b is the bias constrained from the galaxy cluster projected correlation function at the small scales, and β is the ratio between the linear growth rate function $f = \Omega_M(z)^{0.545}$, as predicted by General Relativity, and the bias b. The value of the bias has been obtained fitting the projected correlation function with the jackknife covariance. The covariance matrix used for the fit is the one derived with the sub-sampling approach. The estimated values of the bias and its standard deviation for each sample are reported in Table 4.1.

The density fields are generated in boxes large enough to contain the survey volumes, with a regular grid of steps half the size of the bins used to estimate the 2PCF. The survey selection function is taken into account in the random catalogues. Once the mock clusters are extracted according to the density distribution, the covariance matrix can be directly estimated by measuring the 2PCF for each mock sample.

4.3   Clustering measurements

In the top panel of Fig. 4.3 we present the measured 2PCF for the three galaxy cluster samples considered. We used LS estimator for the 2PCF (Eq. (1.62)), with bins of $8 \, \mathrm{Mpc} \, h^{-1}$ for the Main-CGS and LOWZ-CGS and of $10 \, \mathrm{Mpc} \, h^{-1}$ for CMASS-CGS. Error bars shown are the ones computed with the lognormal mock method. The measures are robust when changing the modelling of the radial selection function. The clustering signal is well determined despite the sparseness of the samples. The measured 2PCFs are all consistent with each other in terms of the BAO peak position,
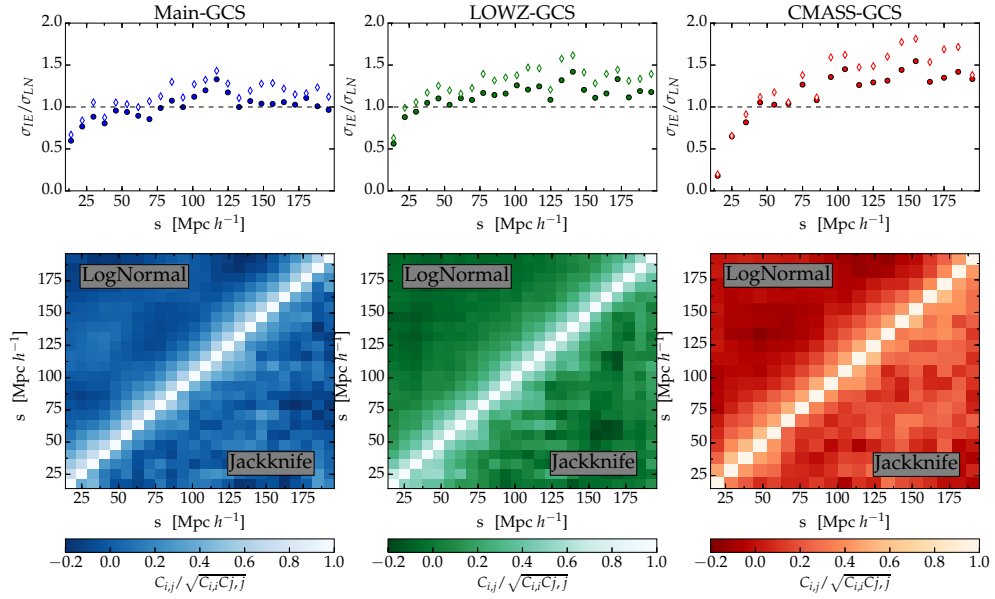
Figure 4.2: *Upper panels*: ratio of internal error (jackknife: filled circles, bootstrap: open diamonds) and lognormal principal diagonal square roots. At the scales of interest for the fit, internal error methods provide a conservative error estimate. *Lower panels*: correlation matrices ($C_{i,j}/\sqrt{C_{i,i}C_{j,j}}$) from lognormal realizations (upper diagonal part) and from jackknife estimates (lower diagonal part). The 1000 lognormal mocks provide a less scattered covariance matrix with respect to the jackknife method. This is due mainly to the low number of bins (50) used when resampling the catalogue.

though a significant difference in the bias is measured (see Table 4.1). As already pointed out in § 4.2.3, we consider different methods to compute the covariance matrix. In the case of internal errors, we divide each cluster catalogue in 50 samples to get the jackknife estimate, and re-sample them 200 times to exploit the bootstrap technique. We use instead 1000 lognormal mock realizations. Results are shown in Fig. 4.2. In the top panels we compare internal estimates (filled circles for jackknife, open diamonds for bootstrap) and lognormal mock estimates of the square root of the principal diagonal values of the covariance matrix. Internal methods provide conservative estimates of the errors, that become less biased for larger number of objects. Both the jackknife and bootstrap estimates are robust when changing the number of subsamples, or resamplings. Nevertheless, a large number of realizations makes the covariance matrix less scattered. This can be seen in the bottom panels of Fig. 4.2: the covariance matrix obtained with lognormal mocks is smoother compared to the jackknife one. In the following we adopt the lognormal mock estimate of the covariance matrix as the reference. Covariance matrices from internal estimators will be used to check for consistencies in the parameter determination and BAO peak detection.
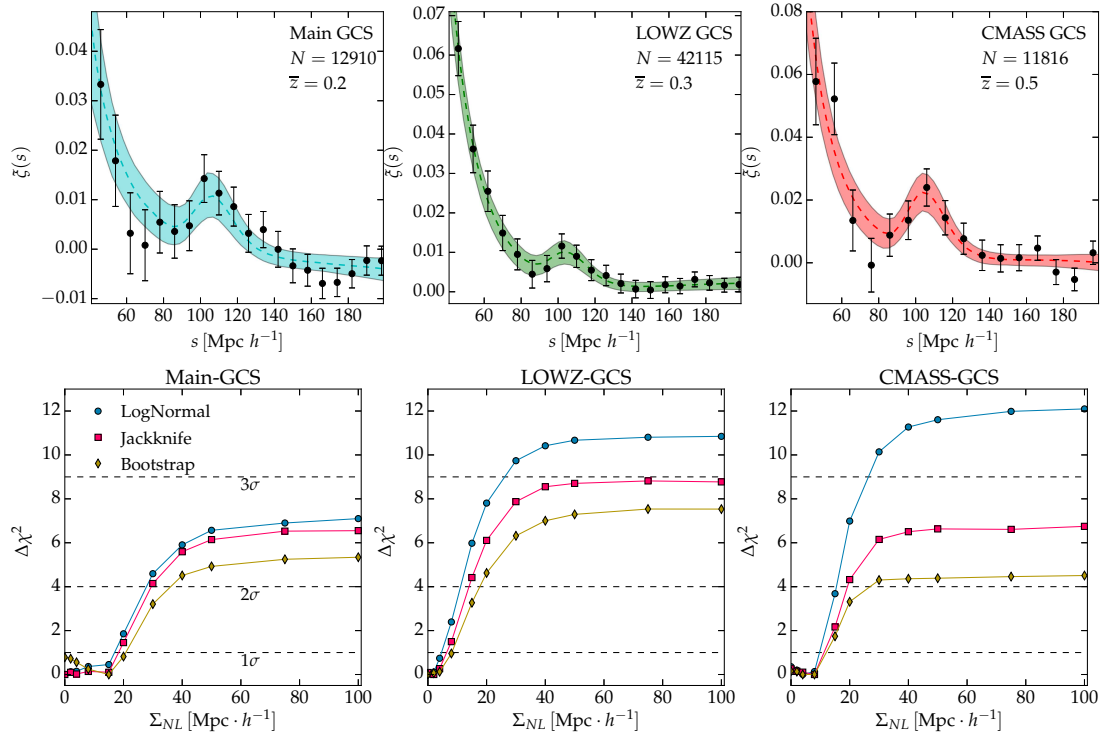
Figure 4.3: Top panel. The redshift-space 2PCF of galaxy clusters, respectively Main-GCS (left panel), LOWZ-CGS (central panel) and CMASS-CGS (right panel). The errorbars are computed with the lognormal mock method. The dashed line shows the best-fit model from Eq. 1.82. The shaded area represents the 68% posterior uncertainties provided by the MCMC analysis. Bottom panel. The values of $\Delta\chi^2$ as a function of Σ_{NL} for the three cluster samples – Main-GCS (left panel), LOWZ-GCS (centeral panel), and CMASS-GCS (right panel) – and for the three covariance matrix definitions – lognormal mocks (blue filled circles), jackknife (red squares) and bootstrap (yellow diamonds). The values span from a linear power spectrum ($\Sigma_{NL} = 0 \mathrm{\ Mpc}\,h^{-1}$) to a power spectrum model with no BAO ($\Sigma_{NL} \to \infty$). Detections of the BAO are well over 2σ in all cases.

4.3.1   Distance constraints

We get distance constraints by fitting the BAO peak position in the measured 2PCF at different redshifts. The BAO feature is clearly detected for all samples. Results of the fits using the different definitions of the covariance matrix are reported in Table 4.2. The α values estimated in the three redshift bins are all consistent. The precision in the detection degrades when using jackknife or bootstrap covariance matrices, as expected. As already described in § 1.6.2, and applied in § 3.6, the model depends on the parameter Σ_{NL}, that describes the degradation of the BAO feature in the power spectrum. The bottom panel of Fig. 4.3 shows the values of $\Delta\chi^2$ as a function of Σ_{NL}. Each point represents the difference between the minimum χ^2 at each Σ_{NL} and the absolute minimum of the curve. We do this for all the three samples and

Sample Name	LogNormal	Jackknife	Bootstrap
Main-GCS	0.97 ± 0.06	0.97 ± 0.08	0.98 ± 0.08
LOWZ-GCS	0.99 ± 0.03	0.99 ± 0.04	0.99 ± 0.05
CMASS-GCS	0.99 ± 0.03	0.99 ± 0.06	0.99 ± 0.08

Table 4.2: Values of the shift parameter α for the three catalogues, obtained using covariance matrices from lognormal mocks, jackknife and bootstrap subsampling, from column 2 to column 4. All the results have been obtained by fitting the 2PCF from $40 \, \mathrm{Mpc} \, h^{-1}$ to $200 \, \mathrm{Mpc} \, h^{-1}$, and fixing $\Sigma_{NL} = 4 \, \mathrm{Mpc} \, h^{-1}$.

for the three error definitions. This allows us to determine the significance of our detections. The significance of the BAO detections result to be well above 2σ for all the considered samples. Also in this case we cannot distinguish between models with $\Sigma_{NL} < 8 \, \mathrm{Mpc} \, h^{-1}$, that are all consistent within 1σ. Nevertheless, Fig. 4.3 clearly indicates that galaxy clusters have a more limited non-linear contribution at the BAO scales with respect of other tracers, such as galaxies (the $\Delta\chi^2$ minima are in some cases at $\Sigma_{NL} = 0 \, \mathrm{Mpc} \, h^{-1}$). Again, a practical consequence is that the density field reconstruction seems not crucial in the BAO distance constraints from galaxy clusters, as already pointed out in § 3.6. Hereafter we consider the lognormal results with $\Sigma_{NL} = 4 \, \mathrm{Mpc} \, h^{-1}$ as our reference distance constraint.

We measure the following values: $D_V(z = 0.2)(r_s^{fid}/r_s) = 545 \pm 31 \, \mathrm{Mpc} \, h^{-1}$, $D_V(z = 0.3)(r_s^{fid}/r_s) = 806 \pm 24 \, \mathrm{Mpc} \, h^{-1}$ and $D_V(z = 0.5)(r_s^{fid}/r_s) = 1247 \pm 53 \, \mathrm{Mpc} \, h^{-1}$. Fig. 4.4 shows the distance-redshift diagram. The coloured points are the isotropic distance estimates for the Main-GCS (blue), the LOWZ-GCS (green) and the CMASS-GCS (red) sample, respectively. We also show the point obtained for the full sample of clusters (yellow circles). The other black symbols show D_V estimates for galaxy samples from literature: 6dFGS survey (Beutler et al., 2011, black star), Main galaxy sample (MGS) from SDSS DR7 (Ross et al., 2015, black diamond), BOSS LOWZ and CMASS DR12 (Cuesta et al., 2016, black square and pentagon, respectively) and WiggleZ (Kazin et al., 2014, black cross). The black curve is the theoretical prediction for the Planck ΛCDM cosmology (Planck Collaboration et al., 2014b). As it can be seen, our results are fully consistent with previous measurements from galaxy surveys, and with standard ΛCDM predictions. Results are fully consistent with constraints for the whole galaxy cluster sampl,e as showed in § 3.6.

4.3.2 Sample covariance

As already pointed out in section 4.2.1, the Main-GCS and the LOWZ-GCS catalogues have a large fraction of data in common ($\sim 2/3$ of galaxy clusters in the Main-GCS). Thus distance constraints from these two samples are not independent. To estimate the sample correlation, we construct 100 lognormal mocks of both Main-CGS and LOWZ-GCS, according to their sample selection functions. The mocks share the same
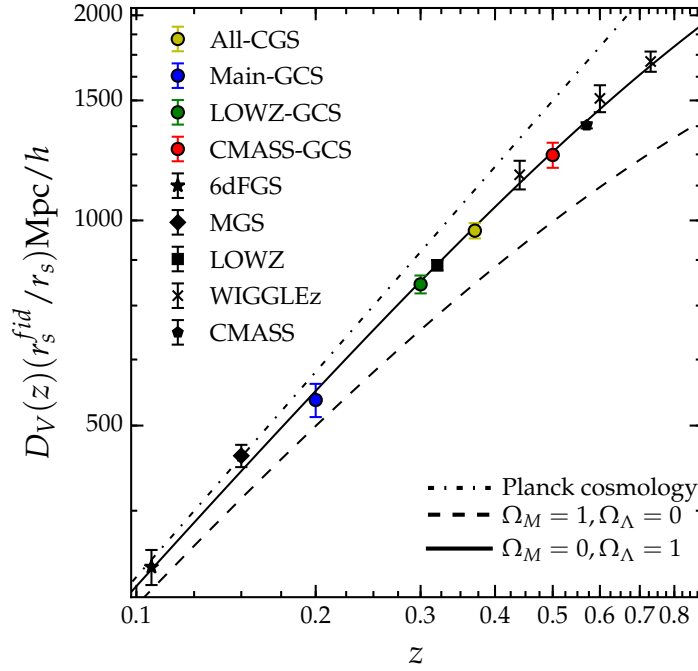
Figure 4.4: The distance $D_V(z)/(r_s^{fid}/r_s)$ – redshift relation. The coloured points show our measurements at redshifts $0.2, 0.3, 0.5$. The distance estimates from Main-GCS and LOWZ-GCS (blue and green dot, respectively) are not independent: the correlation factor between the two samples is $\approx \rho = 0.4$ (see § 4.3.2). We also show the BAO distance constraint of the whole cluster sample (yellow circles). Other black symbols correspond to other distance constraints from galaxy surveys: 6dFGS (Beutler et al., 2011, star), MGS (Ross et al., 2015, diamond) , BOSS LOWZ and CMASS (Cuesta et al., 2016, square and pentagon, respectively) and WiggleZ (Kazin et al., 2014, crosses). The black curve is the $D_V(z)$ prediction for the ΛCDM cosmology with the Planck parameters (Planck Collaboration et al., 2014b). We also show distance prediction in a flat, matter-only Einstein-De Sitter universe (black dashed curve) and for a De Sitter universe with $\Omega_\Lambda = 1$ (black dot-dashed curve)

fraction of data as in the real case. we measure the 2PCF of each realization, and fit the measurements with a two-parameter model:

$$\xi(r) = b^2 \xi_{DM}(\alpha r) , \tag{4.2}$$

where b is the bias factor and α is the shift parameter. We then calculate the covariance matrix, $C_{i,j}$, for the derived values of α:

$$C_{i,j} = \frac{1}{N_{mock}-1} \sum_{k=1}^{N_{mock}} (\alpha_i^k - \hat{\alpha_i})(\alpha_j^k - \hat{\alpha_j}) , \tag{4.3}$$

where i and j run over Main-CGS and LOWZ-CGS α measurements, respectively. The correlation is defined as

$$\rho = \frac{C_{i,j}}{\sqrt{C_{i,i}C_{j,j}}} \ .$$

(4.4)

The correlation is moderate, with $\rho = 0.402$.

4.4 Cosmological implications

We can use the distance measurements described above to derive constraints on cosmological parameters. Using only the three measures obtained with our cluster samples, we do not expect to get constraints competitive with the ones obtained by combining larger galaxy samples with different probes. The aim here is just to check the consistency of our measurements with the predictions of the standard cosmological framework, and to quantify the amount of information available from this kind of analysis using clustering of galaxy clusters.

As reported in § 1.6.2, We consider two methods to derive cosmological constraints, that is the *calibrated* and the *uncalibrated* distance estimators. In the first case, we use the Planck value of the sound horizon, $r_s = 147.34 \pm 0.65 \, \mathrm{Mpc}$, to calibrate the BAO distance measure. We have $D_v(z = 0.2) = 800 \pm 50 \, \mathrm{Mpc}$, $D_V(z = 0.3) = 1183 \pm 35 \, \mathrm{Mpc}$ and $D_V(z = 0.5) = 1832 \pm 55 \, \mathrm{Mpc}$. In the second approach the sound horizon is a function of cosmological parameters, through the interpolation formula given by Anderson et al. (2014). In this case we get $r_s/D_V(z = 0.2) = 0.18 \pm 0.01$, $r_s/D_V(z = 0.3) = 0.124 \pm 0.004$ and $r_s/D_V(z = 0.5) = 0.080 \pm 0.002$. The value of Ω_b is kept fixed to the best-fit Planck value (Planck Collaboration et al., 2014b): $\Omega_b = 0.049$.

We use the full covariance matrix to get cosmological constraints. The only non-diagonal term comes from the cross-correlation between the Main-CGS and LOWZ-CGS samples, as described in § 4.3.2. We tested the robustness of our results when using only the diagonal terms of the covariance matrix. As expected, we get constraints $5 - 10\%$ narrower with respect to the full covariance case. The effect is however small, considering the estimated uncertainties.

With both the methods we test some cosmological scenarios. Specifically, we constrain the cosmological parameters that enter the Hubble function, $H(z)$. In fact, the quantity D_V is a function of $H(z)$ and of the angular diameter distance $D_A(z)$, which in turn depends on the comoving distance $D_C(z) = \int_0^z \mathrm{d}z' c/H(z')$ (Eq. (1.54)).

4.4.1 ΛCDM models

The simplest model we test is the flat ΛCDM Universe (equation of state $w = -1$), with a negligible contribution of radiation. In this case the Hubble function reads:

$$H^2(z)/H_0^2 = \Omega_M(1 + z)^3 + \Omega_\Lambda \ .$$

(4.5)

ΛCDM		Distance	
		D_V	d_z
H_0 $[\,\mathrm{km\,s^{-1}Mpc^{-1}}\,]$	Prior	$\mathcal{U}(30, 120)$	$\mathcal{U}(30, 120)$
	Posterior	71^{+14}_{-14}	64^{+17}_{-8}
Ω_M	Prior	$\mathcal{U}(0, 1)$	$\mathcal{U}(0, 1)$
	Posterior	$0.32^{+0.22}_{-0.15}$	$0.33^{+0.24}_{-0.16}$

Table 4.3: Summary of the cosmological parameters obtained by fitting the calibrated BAO distance D_V and the uncalibrated BAO distance d_z for ΛCDM cosmology. We report priors used in the fitting procedures.

Since the curvature $\Omega_k = 1 - \Omega_M - \Omega_\Lambda - \Omega_r$ is fixed to zero, Ω_Λ is a function of Ω_M. We fit our distance constraints against the pair $\{\Omega_M, H_0\}$. We impose a large uniform prior on both parameters: $\mathcal{U}(0, 1)$ for Ω_M and $\mathcal{U}(30, 120)$ for H_0. Here $\mathcal{U}(a, b)$ is the uniform distribution, equal to 0 outside prior limits a, b. We find $\Omega_M = 0.32^{+0.22}_{-0.15}$ and $H_0 = 71^{+14}_{-14}$ $\mathrm{km\,s^{-1}Mpc^{-1}}$ for the calibrated distance indicator, and $\Omega_M = 0.33^{+0.24}_{-0.16}$ and $H_0 = 64^{+17}_{-8}$ $\mathrm{km\,s^{-1}Mpc^{-1}}$ for the uncalibrated case. Results are summarized in Fig. 4.5 (upper left panel), where we show the $1 - 2\sigma$ confidence contours for the parameters $\Omega_M - H_0$. The Planck cosmology is well compatible with our results, in both cases. Our constraints are broad, due to our distance uncertainties and to our limits in redshift. As we will show in particular for the next cases, high-redshift distance measures significantly help in measuring the geometry of the Universe.

4.4.2 $o\Lambda$**CDM models**

Here we test our measurements against a non-flat Universe with CDM and cosmological constant. In this case the Hubble equation becomes:

$$H^2(z)/H_0^2 = \Omega_M(1 + z)^3 + \Omega_\Lambda + \Omega_k(1 + z)^2; . \qquad (4.6)$$

We fit the combination of parameters $\{\Omega_M, \Omega_\Lambda, H_0\}$, using a flat prior for Ω_Λ, and broad Gaussian priors, $\mathcal{N}(\mu, \sigma)$, for Ω_M and H_0, with mean values, μ, set from Planck ($\Omega_M = 0.31$ and $H_0 = 67\,\mathrm{km\,s^{-1}Mpc^{-1}}$), and standard deviations, σ, of 0.3 and $20\,\mathrm{km\,s^{-1}Mpc^{-1}}$, respectively. See Tab. 4.4 for more information on the adopted priors. We find $\Omega_k = -0.00^{0.44}_{-0.48}$ for the D_V fit and $\Omega_k = 0.01^{+0.34}_{-0.33}$ for the fit using r_s/D_V. In Fig. 4.5 (upper right panel) we show the $1 - 2\sigma$ confidence contours for the combination $\Omega_M - \Omega_\Lambda$, marginalized over H_0. we confirm at 1σ the necessity of a negative pressure component in the cosmological model. The different degeneracy directions obtained with the two methods are due to the introduction of the cosmological dependence of the sound horizon, that depends only on $\Omega_M h^2$ and $\Omega_b h^2$.

$o\Lambda$CDM		Distance	
		D_V	d_z
H_0 $[\,\mathrm{km\,s^{-1}Mpc^{-1}}\,]$	Prior	$\mathcal{N}(67, 20)$	$\mathcal{N}(67, 20)$
	Posterior	70^{+12}_{-10}	64^{+13}_{-12}
Ω_M	Prior	$\mathcal{N}(0.3, 0.3)$	$\mathcal{N}(0.3, 0.3)$
	Posterior	$0.35^{+0.21}_{-0.18}$	$0.34^{+0.15}_{-0.11}$
Ω_Λ	Prior	$\mathcal{U}(0, 1.5)$	$\mathcal{U}(0, 1.5)$
	Posterior	$0.65^{+0.34}_{-0.34}$	$0.64^{+0.34}_{-0.36}$

Table 4.4: Same as table 4.3, for $o\Lambda$CDM cosmology.

wCDM		Distance	
		D_V	d_z
$H_0[\,\mathrm{km\,s^{-1}Mpc^{-1}}\,]$	Prior	$\mathcal{N}(67, 20)$	$\mathcal{N}(67, 20)$
	Posterior	67^{+12}_{-11}	60^{+13}_{-8}
Ω_M	Prior	$\mathcal{U}(0, 1)$	$\mathcal{U}(0, 1)$
	Posterior	$0.40^{+0.17}_{-0.17}$	$0.38^{+0.21}_{-0.14}$
w	Prior	$\mathcal{U}(-2, 0)$	$\mathcal{U}(-20)$
	Posterior	$-1.12^{+0.46}_{-0.55}$	$-1.06^{+0.49}_{-0.52}$

Table 4.5: Same as table 4.3, for wCDM cosmology.

4.4.3 w**CDM models**

We now test our data against a flat Universe with CDM and dark energy, with dark energy density changing with time. We parametrize the dark energy density time dependence with constant equation of state w. The Hubble equation in this case is:

$$H^2(z)/H_0^2 = \Omega_M(1 + z)^3 + \Omega_{DE}(1 + z)^{3(1+w)} \,. \tag{4.7}$$

This model turns into standard ΛCDM cosmology imposing $w = -1$. We fit the combination of parameters $\{\Omega_M, w, H_0\}$, since, as in the ΛCDM case, the value of Ω_{DE} at the present time is fixed by the relation $\Omega_{DE} = 1 - \Omega_M$. we assume a flat prior on Ω_M and w and a broad Gaussian prior on H_0, centered at the Planck value $67\,\mathrm{km\,s^{-1}Mpc^{-1}}$, with a standard deviation of $20\,\mathrm{km\,s^{-1}Mpc^{-1}}$. We find $w = -1.12^{+0.46}_{-0.55}$ for the calibrated distance fit, and $w = -1.06^{+0.49}_{-0.52}$ for the uncalibrated one. contours up to 2σ for the pair $\Omega_M - w$ are shown in Fig. 4.5 (lower left panel), while the best-fit corresponding value of α is reported in the third row of Fig. 4.5.

owCDM		Distance	
		D_V	d_z
H_0 $[\,\mathrm{km\,s^{-1}Mpc^{-1}}\,]$	Prior	$\mathcal{N}(67,2)$	$\mathcal{N}(67,2)$
	Posterior	$67.0^{+1.5}_{-1.5}$	$60.0^{+1.4}_{-1.4}$
Ω_M	Prior	$\mathcal{N}(0.31,0.02)$	$\mathcal{N}(0.31,0.02)$
	Posterior	$0.31^{+0.01}_{-0.01}$	$0.32^{+0.01}_{-0.01}$
Ω_{DE}	Prior	$\mathcal{U}(0,1.5)$	$\mathcal{U}(0,1.5)$
	Posterior	$0.67^{+0.45}_{-0.25}$	$0.68^{+0.44}_{-0.25}$
w	Prior	$\mathcal{U}(-1.5,0)$	$\mathcal{U}(-1.5,0)$
	Posterior	$-0.87^{+0.23}_{-0.38}$	$-0.88^{+0.24}_{-0.37}$

Table 4.6: Same as table 4.3, for owCDM cosmology.

4.4.4 ow**CDM models**

The most general case we consider is the one with a non-flat Universe with time-dependent dark energy density:

$$H^2(z)/H_0^2 = \Omega_M(1+z)^3 + \Omega_{DE}(1+z)^{3(1+w)} + \Omega_k(1+z)^2 \ . \tag{4.8}$$

We vary the parameters $\{\Omega_M, \Omega_{DE}, w, H_0\}$, keeping totally free Ω_{DE} and w, and assuming a Gaussian prior for Ω_M, centered on 0.31 with a standard deviation of 0.02, and for H_0 centered on $67\,\mathrm{km\,s^{-1}Mpc^{-1}}$ with a small standard deviation of $2\,\mathrm{km\,s^{-1}Mpc^{-1}}$, respectively. In the case of the uncalibrated distance measure, the strong priors on Ω_M and H_0 resume in an almost constant value for the sound horizon. Since the central values for these two parameters are the ones from Planck, the value of the sound horizon is centered on the Planck value too. This explains the similarity in the bottom row of Fig. 4.5 (lower right panel) that shows the degeneracy between the parameters Ω_{DE} and w. Even with the assumption of these strong priors, no clear constraint can be extracted in this case. As we verified, the impact of the assumed priors on our results is small, considering the uncertainties in our measurements. For instance, changing the mean value of the Gaussian prior on Ω_M in the range $\{0.29, 0.33\}$, the derived mean values of the posteriors of Ω_{DE} and w_0 change in the ranges $\{0.63, 0.68\}$, and $\{-0.91, -0.94\}$, respectively. In Table 4.6 we report the $16-84th$ percentile intervals of the parameter posterior distributions.
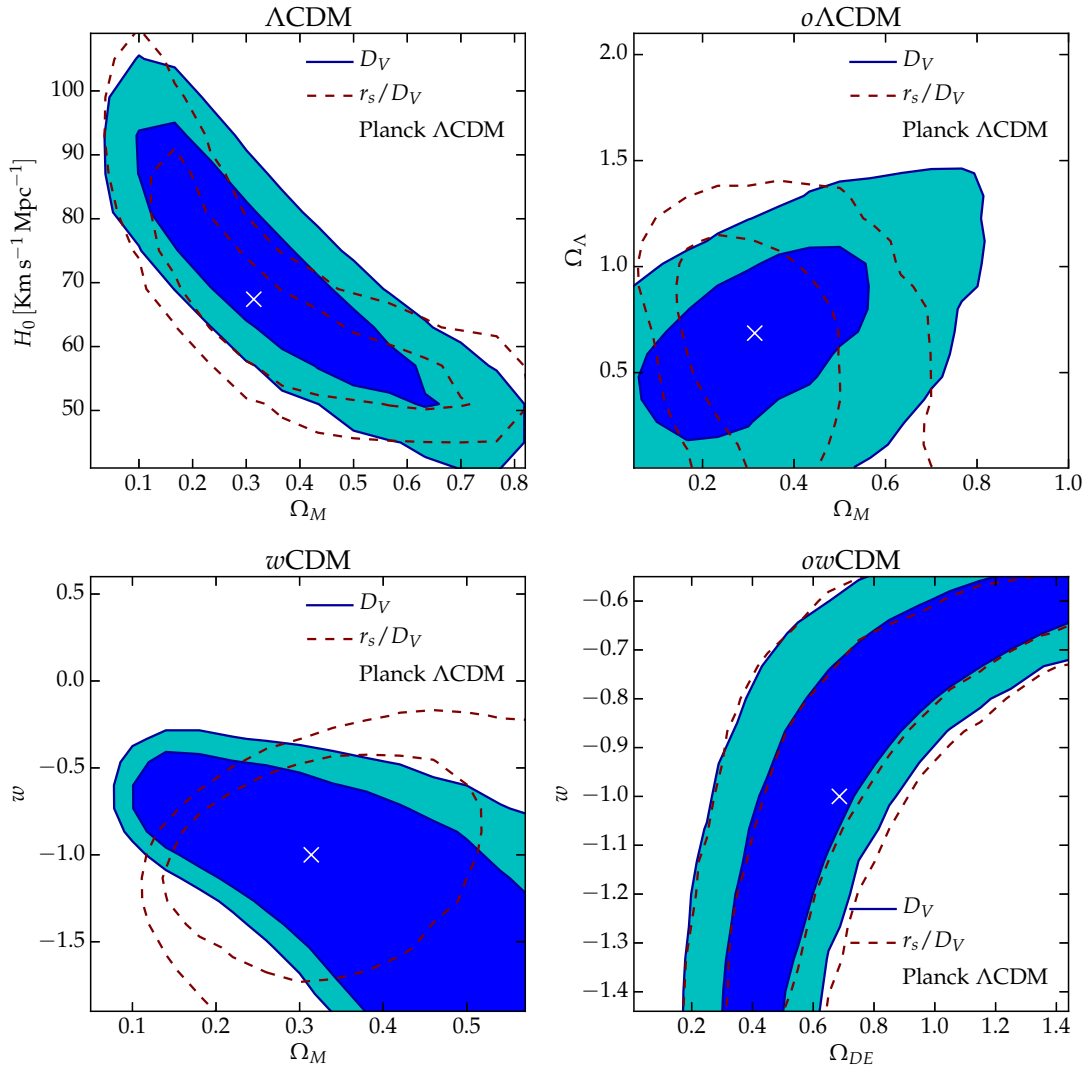
Figure 4.5: $1 - 2\sigma$ confidence contours for parameters assuming different cosmological models: Ω_M-H_0 plane in the ΛCDM model (upper left panel), $\Omega_M - \Omega_\Lambda$ plane in the $o\Lambda$CDM model (upper right panel), $\Omega_M - w$ plane in the wCDM model (lower left panel) and $\Omega_{DE} - w$ plane in the owCDM model(lower right panel). The red dashed contours show results from the uncalibrated distance r_s/D_V, the blue for the calibrated distance D_V. The best fit value for Planck ΛCDM cosmology is also reported (white cross).
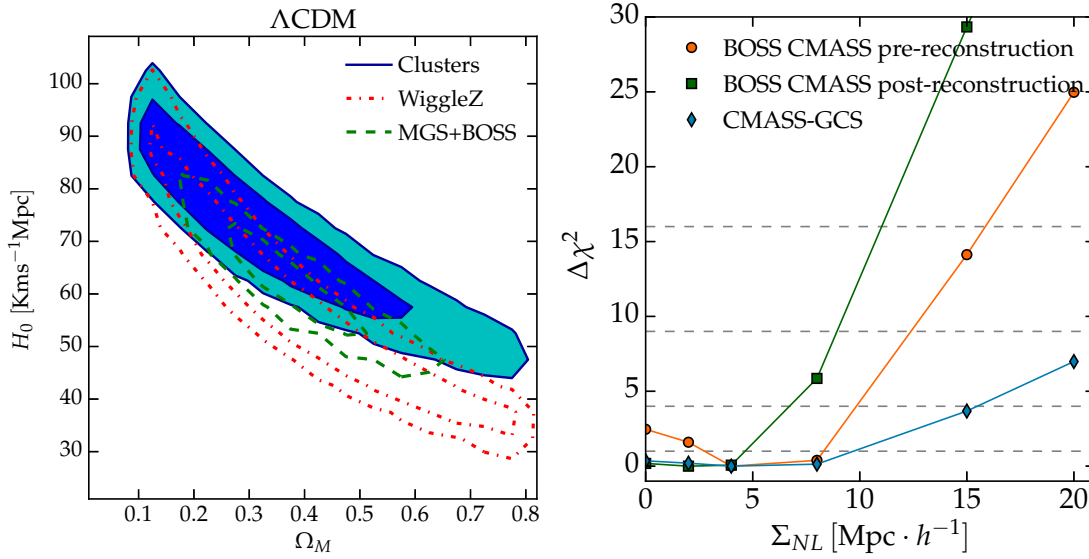
Figure 4.6: left Panel: comparison of the $1 - 2\sigma$ confidence contours in the $\Omega_M - H_0$ plane between our work (blue filled contours) and previous measurements from galaxy samples – WiggleZ (red dot-dashed contours) and MGS+BOSS (green dashed contours). Right panel The same as bottom panel of Fig. 4.3 but for BOSS CMASS before (orange filled circles) and after reconstruction (green filled squares) (Cuesta et al., 2016) and CMASS-GCS, with lognormal mock covariance matrix (blue filled diamonds). The high significance of the BAO detection is evident for galaxies, compared to our results. The reconstruction process helps in reducing non-linear effects, shifting the $\Delta\chi^2$ minimum to $4\,\mathrm{Mpc}\,h^{-1}$ in the post-reconstruction measurement.

4.5 Comparison with previous measurements

The left panel of Fig. 4.6 shows the posterior $1 - 2\sigma$ confidence contours of Ω_M–H_0 parameters, obtained with the calibrated distance estimators (see § 4.3.1) from the BAO of the galaxy cluster samples considered in this work, and of the galaxy samples of MGS+BOSS Anderson et al., 2014; Cuesta et al., 2016; Ross et al., 2015 and WiggleZ (Kazin et al., 2014). As one can see, our constraints are consistent with previous estimates. Our uncertainties appear slightly better than the ones obtained by modelling the post-reconstruction WiggleZ clustering (Kazin et al., 2014), despite the paucity of our samples, while they are broader with respect to the ones from the BOSS survey (Anderson et al., 2014; Cuesta et al., 2016). This is expected, since our BCGs represent a subsample of the BOSS galaxy survey. Indeed, the measurements obtained with these BOSS galaxy catalogues provide the best BAO distance constraints to date, both in term of accuracy and of BAO reconstruction and modelling techniques[2].

Compared to clusters, we find a lower value of the bias factor for the BOSS galaxies.

---

[2]the 2PCF for the galaxies of the CMASS sample pre- and post-reconstruction, together with covariance matrices, are publicly available https://www.sdss3.org/science/boss_publications.php.

This result is expected and implies that our cluster catalogues cannot be simply considered as random sub-samples of the galaxy catalogue, but they identify the highest peaks of the density field, confirming our previous results (Veropalumbo et al., 2014).

Finally, we reanalyze the BOSS CMASS clustering data with the method described in § 1.6.2. Right panel of Fig. 4.6 shows the values of $\Delta\chi^2$ as a function of Σ_{NL} for the BOSS CMASS pre- and post-reconstruction samples, and for our CMASS-GCS sample. Firstly, our estimated value of the BAO detection significance for the BOSS CMASS data is consistent with the value claimed by Anderson et al. (2014). Moreover, this analysis highlights the impact of the density field reconstruction technique, that shifts the best-fit value of Σ_{NL} from $8\,\mathrm{Mpc}\,h^{-1}$ to $4\,\mathrm{Mpc}\,h^{-1}$ and lower, improving BAO distance constraints. On the other hand, galaxy clusters trace a more linear density field with respect to galaxies. Thus, as it has been proved in § 3.6, the reconstruction is be not necessary for galaxy clusters, as it does not improve significantly the BAO peak detection.

This study clearly demonstrates that galaxy clusters are powerful tracers of the cosmic density field and can be efficiently exploited for BAO analyses. Despite the paucity of cluster samples, with respect to generally larger galaxy samples, the higher values of cluster bias and the fact that their redshifts are less distorted by random motions improve the clustering signal, that results almost insensitive to non-linear dynamical distortions. This reflects in a sharper BAO peak in the 2PCF, close to the prediction of linear theory. To further tighten the cosmological constraints obtained in this work, we plan to combine these clustering measurements with estimates of the cluster mass function. These investigations will be presented in a forthcoming work.

Chapter 5

Joint cosmological analysis of galaxy clusters clustering and weak lensing

The joint analysis of clustering and stacked gravitational lensing of galaxy clusters in large surveys can constrain the formation and evolution of structures and the cosmological parameters. On scales outside a few virial radii, the halo bias, b, is linear and the lensing signal is dominated by the correlated distribution of matter around galaxy clusters. We will discuss a method to measure the power spectrum amplitude σ_8 and b based on a minimal modelling. Using same clusters for measuring both lensing and clustering, the estimate of σ_8 does require neither the mass-richness relation, nor the knowledge of the selection function, nor the modelling of b. With an additional theoretical prior on the bias, we obtain $\sigma_8 = 0.75 \pm 0.08$. This chapter is based on the analysis presented in Sereno, Veropalumbo et al. (2015).

5.1 Introduction

Stacked gravitational lensing is the cross-correlation between foreground deflector positions and background galaxy shears. Weak gravitational lensing depends on the total matter density (including dark matter) via the deflection of light due to intervening matter along the line of sight, which both magnifies and distorts galaxy shapes. Stacked lensing can then be used to measure the galaxy-mass cross-correlation. On the other hand, galaxy clustering recovers the auto-correlation of galaxy positions.

Galaxies are biased tracers of the underlying mass distribution (Bhattacharya et al., 2013; Sheth and Tormen, 1999; J. L. Tinker et al., 2010). This severely limits the constraining power of either galaxy clustering or stacked lensing on the matter power spectrum amplitude. Constraints from the two probes have to be combined to break degeneracies and to recover the matter correlation function (Baldauf et al., 2010; Cacciato et al., 2013; Mandelbaum et al., 2013; Miyatake et al., 2015; More et al., 2015; Oguri and Takada, 2011).

Theory and numerical simulations shows that the galaxy bias is extremely complicated to model: it is stochastic, it depends on galaxy properties such as luminosity, colour and/or morphological type, and it is scale dependent on small scales (Cacciato et al., 2013; Marulli et al., 2013; Sheth and Tormen, 1999, and references therein). The proper treatment of how galaxies populate dark matter haloes, assembly bias, and

baryonic effects on the matter power spectrum on small scales requires a very accurate modelling. If the adopted scheme is too restrictive and fails to account for some important features, the constraining power on cosmological parameters is limited and the results can be severely biased.

Galaxy bias contains very valuable information regarding galaxy formation, mainly on small scales, but at the same time it is difficult to model it properly. Complementary approaches have been proposed to deal with bias in joint clustering plus lensing analyses. At one extreme, methods can be optimised to study the bias. Physically motivated models based on the halo occupation distribution (HOD) have been considered to simultaneously solve for cosmology and galaxy bias (Cacciato et al., 2013; Leauthaud et al., 2012; J. L. Tinker et al., 2012; Yoo et al., 2006). Using the small scale lensing signals enhances the signal-to-noise ratio (SNR) and consequently reduces the statistical errors. However, problems connected to theory interpretation, arbitrary bias modelling, and observational uncertainties are more pronounced on small scales and they can cause additional systematic uncertainties which are difficult to ascertain.

At the other extreme, galaxy bias can be seen as a nuisance when attempting to determine cosmological parameters (1.5.1). The information from galaxy clustering and galaxy-galaxy lensing can then be retained only above scales equal to a few times the typical dark matter halo virial radius, where the treatment of the bias is simplified (Baldauf et al., 2010; Mandelbaum et al., 2013; Yoo and Seljak, 2012).

Most of the previous studies which combine clustering and lensing have focused on galactic scales. These studies can be optimised to estimate σ_8. Mandelbaum et al. (2013) recently constrained cosmology and galaxy bias using measurements of galaxy abundances, galaxy clustering and galaxy-galaxy lensing taken from the SDSS DR7. In the framework of the cold dark matter model with a cosmological constant (ΛCDM), they found $\sigma_8 = 0.76 \pm 0.06$. More et al. (2015) measured the clustering and abundance of the BOSS (Baryon Oscillation Spectroscopic Survey) galaxies from the SDSS-III DR11, and their galaxy-galaxy lensing signal with the CFHTLenS to find $\sigma_8 = 0.79 \pm 0.05$.

In the era of precision cosmology, the development of independent methods to measure cosmological parameters is crucial to test possible failures of the standard ΛCDM model. The tension between the lower values of σ_8 inferred from clusters counts (Planck Collaboration et al., 2014b, and references therein) and higher estimates from measurements of the primary Cosmic Microwave Background (CMB) temperature anisotropies (Planck Collaboration et al., 2014a) may reflect either the need to extend the minimal ΛCDM model or some hidden systematics.

The Planck Collaboration et al. (2014b) measured $\sigma_8 = 0.75 \pm 0.03$ and $\Omega_{\mathrm{M}} = 0.29 \pm 0.02$ using number counts as a function of redshift of 189 galaxy clusters from the Planck Sunyaev-Zel'dovich catalogue. However, the values of the cosmological parameters obtained from cluster abundance are degenerate with any systematic error in the assumed scaling relation between mass and the observed quantity. This problem can be solved in the context of joint experiments alike that considered in this work. In fact, the combination of cluster observables (number counts and cluster-cluster

correlation functions) and stacked weak lensing enables secure self-calibration of important systematic errors inherent in these measurements, including the source redshift uncertainty and the cluster mass-observable relation (Oguri and Takada, 2011).

Analyses of the primary CMB temperature anisotropies have provided higher estimates of the power spectrum amplitude. The Planck Collaboration et al. (2014a) found $\sigma_8 = 0.83 \pm 0.02$ assuming a standard flat ΛCDM model. Estimates of cosmological parameters with CMB experiment are very accurate but highly degenerate, since only one source redshift can be observed. Results are then model dependent.

Measurements of the cosmic shear, i.e., the auto-correlation of galaxy shape distortions due to intervening matter along the line of sight, can constrain the amplitude and growth of matter fluctuations. Using non-linear models of the dark-matter power spectrum, Kilbinger et al. (2013) estimated $\sigma_8 = 0.84 \pm 0.03$ for a flat ΛCDM model with $\Omega_M = 0.3$ from 2D large-scale structure weak gravitational lensing in the CFHTLenS. This method is not affected by halo bias but since it relies on auto-correlations rather than shear cross-correlations, coherent additive errors in galaxy shapes (such as those induced by seeing or distortions in the telescope) may be difficult to remove from the analysis (Mandelbaum et al., 2013). Moreover, intrinsic alignments with the local density field anti-correlate with the real gravitational shear and can contaminate cosmic shear measurements (Hirata and Seljak, 2004).

Here we propose a novel method based on the joint analysis of clustering and lensing of clusters of galaxies. The focus on clusters of galaxies is intended for a much simpler discussion. Clusters of galaxies trace the biggest collapsed structures and produce a very clean lensing signal. The stacked lensing technique has been highly successful in measuring the average masses of galaxy clusters down to the less massive haloes (Covone et al., 2014; Ford et al., 2015; Johnston et al., 2007; Mandelbaum, Seljak, and Hirata, 2008). Furthermore, galaxy clusters are more strongly clustered than galaxies. Measurements of the 2PCF of galaxy clusters have already provided detections of the BAO peak(Estrada, Sefusatti, and Frieman, 2009; Hong et al., 2012; Hütsi, 2010; Veropalumbo et al., 2014). For extended informations see § 3, 4.

The novelty of the method is that: *i)* we track clusters of galaxies rather than galaxies; *ii)* we consider the same clusters for both lensing and clustering; *iii)* we determine bias and σ_8 based exclusively on the large-scale signal. Even though some of these elements were separately considered by previous papers, their combination makes for a new approach with minimal modelling.

The method strongly relies on using the same cluster population for both stacked lensing and clustering. If we correlate the positions of the lenses, the galaxy bias for the considered sample can be directly measured without any demanding theoretical modelling. Instead of being a systematic uncertainty, the information on the bias can be extracted to constrain structure formation and evolution. We relate the bias to the observed cluster population rather than trying to model the bias as a function of the halo mass, which would require the problematic calibration of the mass against the observable property the clusters were selected for (Sereno and Ettori, 2014; Sereno,

Ettori, and Moscardini, 2015). At the same time, σ_8 can be estimated without the knowledge of the selection function of the clusters.

The simultaneous analysis of stacked lensing and clustering is further simplified by keeping only the information well beyond the virial radius. Even at large scales, the proper treatment of the connection between galaxies and dark matter requires the modelling of the halo occupation statistics as a function of galaxy luminosity through the conditional luminosity function, combined with the halo model, which describes the non-linear matter field in terms of its halo building blocks (Mandelbaum et al., 2013). The modelling of halo bias from very massive haloes is instead much easier to perform on a theoretical ground (J. L. Tinker et al., 2010).

We focus on the determination of the amplitude of the power spectrum, σ_8, in a reference flat ΛCDM model with matter density parameter $\Omega_M = 0.3$, baryonic density parameter $\Omega_B = 0.04$, spectral index $n_s = 1$ and Hubble constant $H_0 = 100 \, h \mathrm{km \, s^{-1} Mpc^{-1}}$ (Planck Collaboration et al., 2014a). When necessary, we assume $h = 0.7$.

The structure of the chapter is as follows. In § 5.2 we will present the basics of how the combination of galaxy clustering and stacked lensing can determine the amplitude of the power spectrum and the halo bias. In § 5.3, we will introduce the cluster catalogueand the data-sets. Sections 5.4 and 5.5 will detail how we performed the analysis of clustering and stacked lensing, respectively. The joint analysis and the cosmological constraints will be presented in § 5.6. § 5.7 will forecast the performance of the method with Euclid data.

5.2 Overview

As already specified in § 1.3.3, clustered haloes are biased tracers of the underlying mass distribution (Kaiser, 1984; J. L. Tinker et al., 2010).

Auto-correlation functions between either matter or halo density fields depend on the halo bias in different ways. In principle, we can break degeneracies with proper combinations of correlation functions and we can infer at the same time the cosmological parameters and the halo bias.

The matter auto-correlation function is

$$\xi_{mm}(\mathbf{r}) = \langle \delta_m(\mathbf{x})\delta_m^*(\mathbf{x} + \mathbf{r}) \rangle, \tag{5.1}$$

where δ_m is the matter density contrast. The analogous auto-correlation function for the halo density field is $\xi_{hh}(\mathbf{r})$, which is related to the matter statistics through the halo bias b as

$$\xi_{hh}(r) = b^2(r)\xi_{mm}(r). \tag{5.2}$$

On the large scales probed by clusters of galaxies, the cross-correlation coefficient between the matter and halo fluctuations is one and the bias is linear, i.e., $b(r) =$

constant (Mandelbaum et al., 2013). For a given cosmological model, b depends on the mass and the redshift of the haloes hosting the galaxies through the peak height (Bhattacharya et al., 2013; Sheth and Tormen, 1999; J. L. Tinker et al., 2010).

Finally, the cross-correlation function is

$$\xi_{\rm hm}(\mathbf{r}) = \langle \delta_{\rm g}(\mathbf{x}) \delta_{\rm m}^*(\mathbf{x} + \mathbf{r}) \rangle. \tag{5.3}$$

On the observational side, $\xi_{\rm hh}$ and $\xi_{\rm hm}$ can be measured through clustering and stacked lensing, respectively. If we focus on the bias and σ_8, we can single out simple proportionality factors,

$$\xi_{\rm mm} \propto \sigma_8^2, \ \ \xi_{\rm hm} \propto b\,\sigma_8^2, \ \ \xi_{\rm hh} \propto b^2\sigma_8^2. \tag{5.4}$$

In the regime where the bias is linear, b and σ_8 can then be determined as

$$b \propto \frac{\xi_{\rm hh}}{\xi_{\rm hm}}, \ \sigma_8 \propto \sqrt{\frac{\xi_{\rm hm}^2}{\xi_{\rm hh}}}. \tag{5.5}$$

5.3 Data

For the computation of the 2PCF, we consider a subsample of 69527 galaxy clusters from WHL12 sample (see 3.2) selected on a contiguous area of $\sim 9000\ {\rm deg}^2$ in the Northern Galactic Cap obtained including all the SDSS stripes between 10 and 37. Clusters are identified via Friends-of- Friends as overdensities of galaxies in photometric space. The minimum cluster richness is $R_{L_*} = 12$.

This selection is used to ease the reconstruction of the visibility mask. Nevertheless, its impact on the final results is negligible, considering the uncertainties in the measurements.

To optimise the lensing signal, we consider a redshift limited subsample (median redshift $z = 0.365$), wherein 123822 clusters lie (93.3 per cent of the whole sample). The upper redshift limit enabled us to perform a robust separation between the lensing and the background population (Covone et al., 2014).

For the lensing sample, we consider the 1176 clusters centred in the four fields of the Canada-France-Hawaii Telescope Lensing Survey (CFHTLenS, Heymans et al., 2012), covering about 154 square degrees in optical $ugriz$ bands. The public archive[1] provides weak lensing data processed with THELI (Erben et al., 2013), shear measurements with *lensfit* (Miller et al., 2013), and photometric redshift measurements with accuracy $\sim 0.04(1 + z)$ and a catastrophic outlier rate of about 4 per cent (Benjamin et al., 2013; Hildebrandt et al., 2012). Full details on the shear measurements can be found in Heymans et al. (2012). Since we took all clusters in the CFHTLenS fields without any further restriction, the lensing clusters we considered are a small but unbiased subsample of the total catalogue. This was verified with a Kolmogorov-Smirnov test.

---

[1]http://www.cfht.hawaii.edu/Science/CFHLS.

The optical richness (redshift) distributions are compatible with a probability of 49.0 (39.4) per cent.

The CFHTLenS is at the same time much deeper and much smaller than the SDSS. As far as the signal-to-noise ratio of the stacked haloes is concerned, these effects counterbalance each other and lensing results are comparable (Brimioulle et al., 2013; Covone et al., 2014; Ford et al., 2014, 2015; Hudson et al., 2015; Johnston et al., 2007; Mandelbaum, Seljak, and Hirata, 2008; Mandelbaum et al., 2013; Oguri, 2014; Velander et al., 2014). A similar choice of data-sets for a joint analysis of galaxy clustering and galaxy-galaxy lensing was recently made by More et al. (2015).

Since the cluster catalogue and the shape measurements we considered are extracted from completely different data-sets, the SDSS and CFHTLenS data respectively, we are assured that the distribution of lens galaxies is uncorrelated with residual systematics in the shape measurements (Miyatake et al., 2015).

5.4   Clustering

This section provides a general description of the methods used in this work to measure the halo clustering, to estimate the observational uncertainties, and to constrain the linear bias and σ_8. We refer to § 1.5 for further details. We estimate the 2PCF monopole using the LS estimator, (Eq. 1.62) (Landy and Szalay, 1993) We compute clustering for the whole sample and for four richness bins, with 29130 objects in the richness range $12 \leq R_{L_*} < 16$, 21047 for $16 \leq R_{L_*} < 21$, 11962 for $21 \leq R_{L_*} < 30$ and 7388 for $R_{L_*} \geq 30$. The number density decreases as increasing the richness, as expected. This has an impact on our constraint of clustering parameters, as the error increase when diluting the sample.

5.4.1   Random catalogues

To construct the random catalogues, we reproduce separately the angular and redshift selection functions of the cluster sample. This method provides a fair approximation of the full distribution as already described in 3.3.2 (Veropalumbo et al., 2016). The main differences are a) we limit the analysis to the Northern galactic cap, b) we are using the photometric redshifts. We associate redshifts to the random objects by drawing from the observed redshift distribution of the cluster samples. The latter was assessed grouping the data in 100 redshift bins and applying a Gaussian convolution with a kernel three times larger than the bin size (Marulli et al., 2013). Reducing the bin size has the effect of lowering the clustering signal along the line of sight. However, the impact of this effect is negligible considering the measurement uncertainties, as we verified. To minimise the impact of the shot noise at small scales, for each sample considered in this work, we generated a random catalogue 20 times larger.

5.4.2 Error estimates

We use the *jackknife* re-sampling technique to estimate the covariance matrix of the correlation function measurements (Eq. (3.1)).

The *jackknife* subsamples are constructed following the SDSS geometry. With respect to previous analysis, described in § 3.4, we divide the original catalogue in fractions of SDSS stripes (5 regions in each of the 28 considered SDSS stripes, $N_{\mathrm{sub}} = 140$ subvolumes in total) and excluding recursively one of them. As tested, the number of subsamples is large enough to ensure convergence and stability of the covariance matrix estimate.

5.4.3 Modelling the redshift-space cluster clustering

2PCF is affected by *geometric* and *dynamic* distortions (§ 1.5). In particular, the precision of redshift measurements influences the estimate of line-of-sight distances (Marulli et al., 2012). With respect to modelling used in § 1.5, 4, we choose to model the 2PCF monopole with a Gaussian damping term, to introduce the redshift error effect:

$$\exp(-k^2\mu^2, \sigma^2). \tag{5.6}$$

The exponential cut-off term describes the random perturbations of the redshifts caused by both non-linear stochastic motions and redshift errors. It washes out the signal over a typical scale $k \sim 1/\sigma$, thus causing a scale-dependent effect.

To derive the monopole of the correlation function, we integrate Eq. ((3.7)) over the angle μ, and then Fourier anti-transformed. The solution can be written as follows

$$\xi(s) = b^2\xi'(s) + b\xi''(s) + \xi'''(s). \tag{5.7}$$

The main term, ξ', is the Fourier anti-transform of the monopole $P'(k)$:

$$P'(k) = P_{\mathrm{DM}}(k)\frac{\sqrt{\pi}}{2k\sigma}\mathrm{erf}(k\sigma), \tag{5.8}$$

that corresponds to the model given by Eq. ((3.7)) when neglecting the dynamic distortion term. The ξ'' and ξ''' terms are the Fourier anti-transforms of

$$P''(k) = \frac{f}{(k\sigma)^3}P_{\mathrm{DM}}(k)\left[\frac{\sqrt{\pi}}{2}\mathrm{erf}(k\sigma) - k\sigma\exp(-k^2\sigma^2)\right], \tag{5.9}$$

and

$$P'''(k) = \frac{f^2}{(k\sigma)^5}P_{\mathrm{DM}}(k)\left\{\frac{3\sqrt{\pi}}{8}\mathrm{erf}(k\sigma) - \frac{k\sigma}{4}\left[2(k\sigma)^2 + 3\right]\exp(-k^2\sigma^2)\right\}, \tag{5.10}$$

respectively.

In our case, photo-z errors perturb the most the distance measurements along the line of sight. Indeed, as already verified in § 3.8 , the BCGs identified as cluster centres
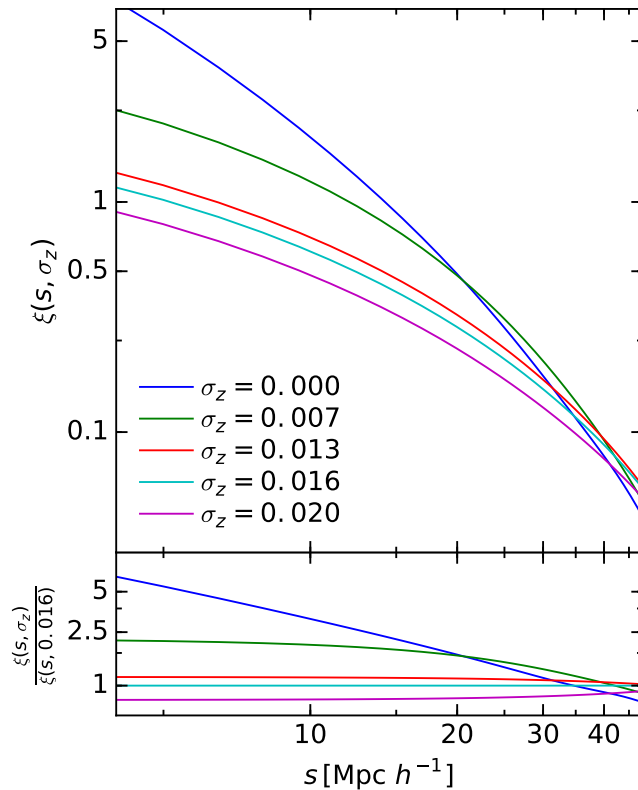
Figure 5.1: *Top panel*: model for the 2PCF estimated with Eq. 5.7 for a fixed value of the bias b=2.7 and five different values for σ_z, as shown in the legend. For sufficiently large values of the redshift error, the shape of the correlation function is almost parallel for the fitting range considered in the study ($10 \leq r[\mathrm{Mpc}\,h^{-1}] \leq 40$). In Fig 3.8 we shows the effect of damping on BAO scales with the same modelling. *Bottom panel*: ratios between the computed models and the one calculated at the redshift error of the cluster sample ($\sigma_z = 0.016$).

are close to the minimum of the cluster potential wells. Therefore their small-scale random motions are negligible with respect to photo-z errors, and the effect of non-linear peculiar velocities at small scales, the so-called *fingers of God* effect, can be safely neglected. The cut-off scale in Eq. ((3.7)) can thus be written as

$$\sigma = \frac{c\sigma_z}{H(z)}, \tag{5.11}$$

where $H(z)$ is the Hubble function computed at the median redshift of the sample, and σ_z is the typical photo-z error. In Fig. 5.1 we show this damped clustering model, for different choices of $\sigma_z = \{0, 0.007, 0.013, 0.016, 0.02\}$. The 2PCF shape results heavily distorted up to very large scales for the introduction of large photometric redshift error.

A similar approach has been used for photometric clustering of galaxy clusters by Estrada, Sefusatti, and Frieman (2009). Authors anyway truncates the term only to the first term. We will describe the effects of this choice in § 5.4.5.

5.4.4 Photo-z errors

Large photo-z errors have a dramatic impact on the measured $\xi(s)$. The real-space clustering can be derived by projecting the correlation function along the line of sight (e.g. Marulli et al., 2013; Veropalumbo et al., 2014). However, this technique becomes quite ineffective for large redshift errors and small survey area, since it would be necessary to integrate the correlation function up to too large scales to fully correct for redshift errors (see § 1.5.4, § 3.5). Here we followed a different strategy, fitting directly the redshift-space clustering with a model that takes into account redshift uncertainties. Due to targeting processes in SDSS, the redshift distributions of the photometric and spectroscopic redshift samples are different. Therefore, to combine clustering with lensing data, we are forced to measure the clustering of the photometric sample.

To estimate the photo-z errors, we use the spectroscopic data available for a sub-sample of the photometric catalogue. A spectroscopic redshift was assigned to a galaxy cluster if it was measured for its BCG. Here we consider spectroscopic redshifts of BCGs basically unaffected by peculiar velocities (Veropalumbo et al., 2014), and are measured with high precision. The resulting sample of clusters with both photometric and spectroscopic redshift measurements consists of 31338 objects.

We estimate the photo-z errors, σ_z by comparing spectroscopic and photometric cluster redshifts in different redshift and richness bins. As shown in Fig. 5.2, the $\Delta z (\equiv z_{\rm phot} - z_{\rm spec})$ distributions are well described by a Gaussian function at all redshifts. Specifically, Fig. 5.2 shows the Δz distributions (black solid lines) estimated in four illustrative redshift bins, $0.10 \leq z_{\rm phot} < 0.21$, $0.21 \leq z_{\rm phot} < 0.30$, $0.30 \leq z_{\rm phot} < 0.38$, and $0.38 \leq z_{\rm phot} \leq 0.59$. The red dashed lines show the best-fit Gaussian models, which faithfully reproduce the measured distributions. The photo-z error, σ_z, could then be estimated as the standard deviation of the distribution.

To reconstruct the full Δz distribution, we use 20 redshift bins. Anyway, the estimate of the photo-z errors resulted to be very weakly dependent on the specific redshift partition. In Fig. 5.3, top panel, we show the variation of σ_z with redshift for the whole sample (black solid line) and for four richness bins (coloured lines) in the entire redshift range. The $z \sim 0.35$ peak is due to the shift of the 4000 Å break from the $g - r$ to $r - i$ colours (Rykoff et al., 2014). Our results agree with what found by Wen, Han, and Liu (2012). As it can be seen in the bottom panel of Fig. 5.3, thanks to the larger number of cluster members, the larger the richness, the smaller the photo-z error. The estimated values of σ_z are reported in Table 5.2. Finally, to obtain a unique value of σ_z to be used in Eq. (5.11), we average the standard deviations measured in the different redshift bins, weighting over the cluster redshift distribution.

5.4.5 Constraints

The analysis to constrain the bias and σ_8 is with MCMC technique, using the full covariance matrix.
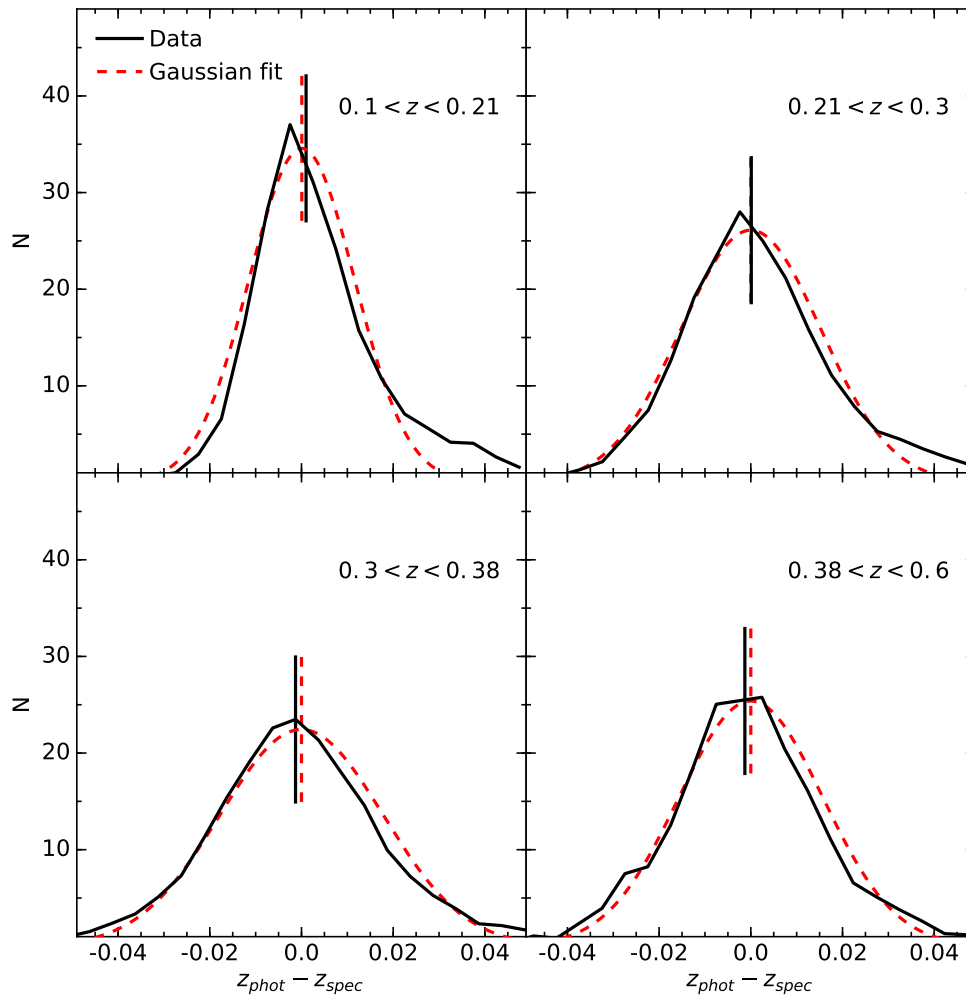
Figure 5.2: distribution of $\Delta z(\equiv z_{\mathrm{phot}} - z_{\mathrm{spec}})$ in four redshift bins (black solid lines) and the associated Gaussian fit (red dashed lines). The limiting values of each redshift bin are indicated in the corresponding panels. The vertical lines correspond to the median values of the Δz distributions (black) and to the mean of the Gaussian models (red dashed).

As described in §5.4.3, we fit the redshift-space 2PCF $\xi(s)$ with the model given by Eq. (5.7).

The redshift-space 2PCF of our photometric cluster sample is shown in Fig. 5.4 (black dots). The error bars are the square root of the diagonal values of the covariance matrix. The dashed blue line shows the best-fit model given by Eq. (5.7). The red line is the result obtained by fitting only the dominant ξ' term. The blue and red lines are in close agreement. The model with only ξ' can fit the data nearly as well as the full model but it produces systematically shifted parameter estimates. If we neglect the Kaiser term, $f\mu^2$, we find a 6 per cent higher bias. The long-dashed green line, that shows the case of a model without the photo-z dumping term, clearly demonstrates the dramatic effect of photo-z errors on the clustering shape.

When the cosmology density parameters are fixed, as in this case, this model
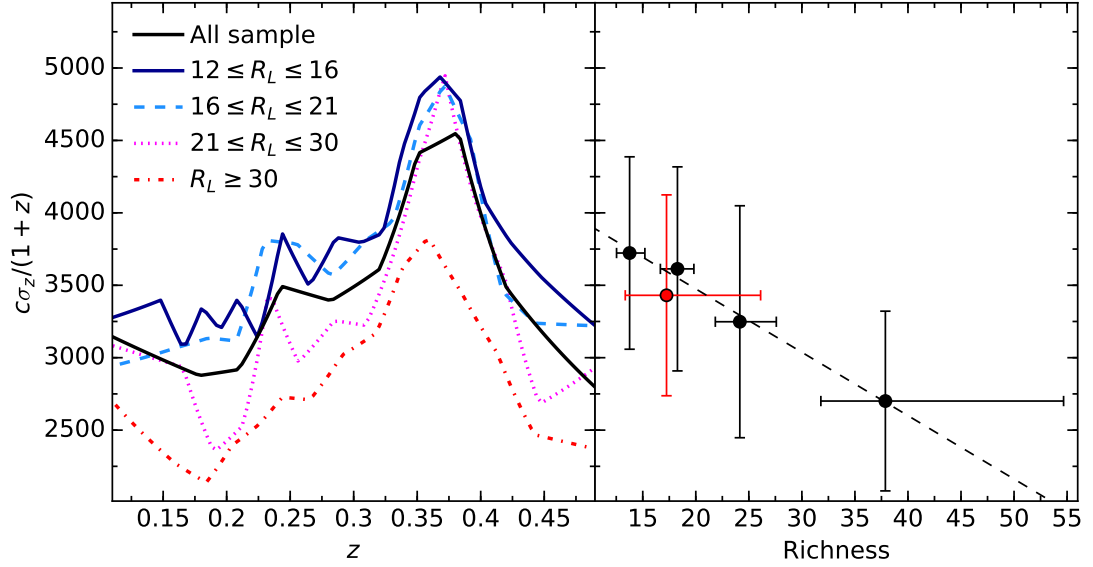
Figure 5.3: *Left panel:* photo-z errors as a function of redshift for the whole sample (black solid line) and for the four richness bins reported in Table 5.2, as indicated by the labels. The photometric redshift is systematically better determined for high richness clusters. *Right panel:* photo-z errors obtained following the procedure described in § 5.4.4 for the whole sample (red point) and for the four richness bins. The horizontal error bars span from the 16 to the 84 percentiles of the cluster richness distribution, while the vertical error bars are the standard deviations of the σ_z redshift distribution. The solid line is a least-squares linear fit to the black points which highlights the decreasing behaviour as a function of richness.

depends on three parameters only, the amplitude σ_8, the bias, b, and the cut-off scale σ, related to σ_z through Eq. (5.11). Formally, the photo-z error is a parameter to be determined too but, following the procedure described in §5.4.4, we assume an informative Gaussian prior on σ_z, with a measured standard deviation of 0.003.

We choose this approach because the bias parameter and the photometric redshift error σ_z are strongly degenerate for sufficiently large values of σ_z on the scale used for the fit ($10 \leq r\,[\mathrm{Mpc}\,h^{-1}] \leq 40$). This is shown in Fig. 5.5, where we present the b-σ_z confidence region constrained from the measured 2PCF fit with the model in Eq.5.7, for the whole cluster sample case (richness $R_L >= 12$). The blue-cyan filled areas are the $1 - 2\sigma$ confidence regions in case of flat prior on σ_z. Contours show the confidence levels after introducing a Gaussian prior on σ_z centred on two different mean values: the estimated one, $\sigma_z = 0.016$, in the left panel and the highest measure, $\sigma_z = 0.02$, in the right one, with two values of the standard deviation, $\Delta\sigma_z = 0.003$ (red contours) and $\Delta\sigma_z = 0.001$ (green contours) respectively.

As can be clearly seen, without priors on σ_z we are not able to constraint the bias. This is due to the behaviour of the model for large values of σ_z as we show in Fig. 5.1. We notice an increasing loss of correlation from small to large scale for higher values of
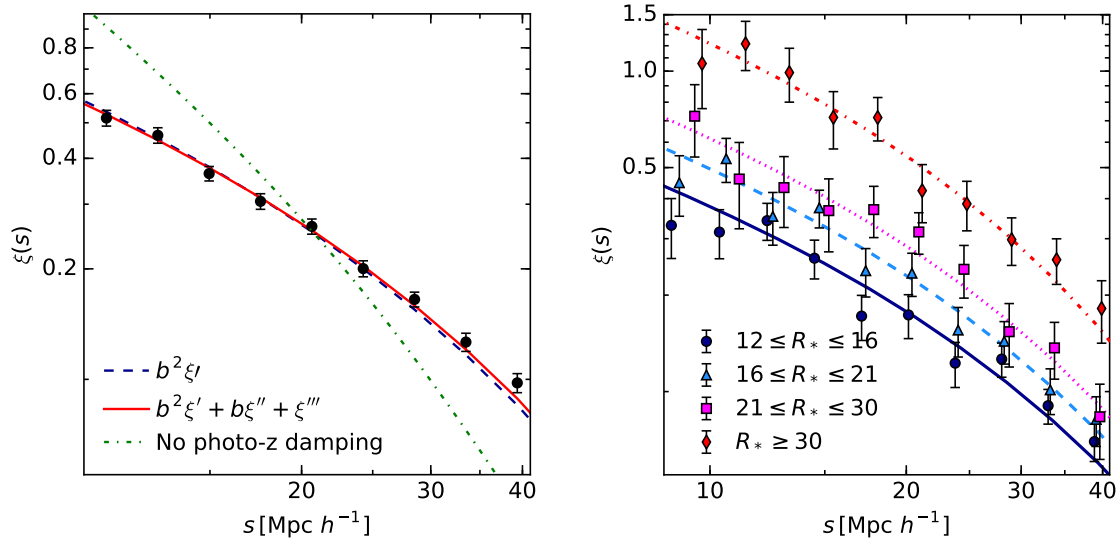
Figure 5.4: *Left panel.* The redshift-space 2PCF of the whole cluster sample ($R_{L_*} \geq 12$, black dots), compared to best-fit models obtained with the full model in Eq. (5.7, red solid line), the dominant ξ' term only (blue dashed line), and without the photo-z damping term (green long-dashed line). The error bars show the square roots of the diagonal values of the covariance matrix. *Right panel.* The redshift-space 2PCF of the four richness-selected cluster samples (dots), compared to the best-fit model obtained with Eq. (5.7, lines). The blue, magenta, purple, and red colour codes refer to the $12 \leq R_{L_*} < 16$, $16 \leq R_{L_*} < 21$, $21 \leq R_{L_*} < 30$, and $R_{L_*} > 30$, respectively. The error bars show the square roots of the diagonal elements of the covariance matrix.

σ_z (top panel). On the scale considered in this work, for sufficiently large values of σ_z (≈ 0.01), models have a very similar shape (bottom panel of Fig. 5.1): differences on σ_z are compensated with higher value of the bias.

Introducing a Gaussian prior on σ_z allows us to constrain the bias. However, using a wrong value for the mean of the photometric redshift error introduces a *systematic error* in the bias estimate.

Constraints are strongly degenerate. Clustering is strongly dependent on the product $b \sigma_8$. This degeneracy would be exact if the correlation function was measured in the real space. For the whole sample, we measured $b \sigma_8 = 2.29 \pm 0.08$, at the median redshift $z = 0.37$. The error estimate is conservative, due to the choice of the prior standard deviation. Lowering the value of the σ_z standard deviation enhances the precision of the measurement. This value is in very good agreement with results from spectroscopic cluster clustering, presented in § 3.5, demonstrating the goodness of the solution we choose to adopt. Anyway, despite the enhanced number density for the photometric cluster sample, redshift error influence the results broadening constraints by a factor ~ 2.

We repeat the analysis in the 4 richness bins, finding the value of $b\sigma_8$ increasing
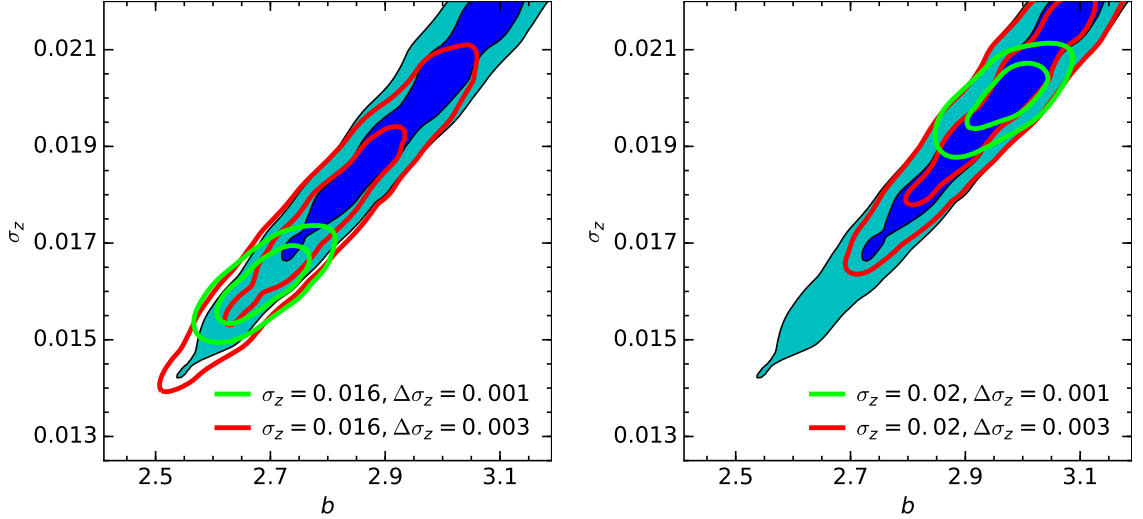
Figure 5.5: *Left Panel*: confidence region in the $b - \sigma_z$ plan. The filled area constraints the $1 - 2\sigma$ confidence of the parameters with flat priors, while the contours are obtained with a Gaussian prior on σ_z with mean $= 0.016$ and standard deviation $\Delta\sigma_z$ respectively 0.003 (red contours) and 0.001 (green contours). *Right panel*: same as left panel, with mean of the Gaussian prior $= 0.02$.

with redshift; we get $b\sigma_8 = 1.87 \pm 0.08$ for first richness bin, $b\sigma_8 = 2.12 \pm 0.08$ and $b\sigma_8 = 2.3 \pm 0.16$ for the intermediate bins; finally we get $b\sigma_8 = 2.97 \pm 0.16$ for the higher richness bin. Together with increase of the bias, worsening of constraint can also be appreciated; this is due, as expected to increasing noise in the clustering of the sample due to change in number density of tracers.

Figure 5.4 shows the redshift-space clustering measured in the four richness-selected samples. The amplitude of the correlation function scales according to the richness. The lines are the best-fit full models given by Eq. (5.7). Richer clusters also shows more precise redshift estimates; this is expected as the photometric redshift error are estimated as the mean of members redshift; the more the members the smaller is the mean error $\sigma_z^{cl} \approx \sigma_z^{gal}/\sqrt{(N_{members})}$. The results are summarised in Table 5.2.

5.5 Weak lensing

The connection between galaxies and matter can be probed with gravitational lensing. In this section, we review the methods used to extract the lensing signal from the shape measurements, to estimate the observational uncertainties, and to constrain the cosmological parameters.

5.5.1 Basics

The so-called shear-cluster correlation (or stacked lensing) is the cross-correlation between the cluster distribution and the shapes of source galaxies. The main observable

quantity for weak lensing is the tangential shear distortion γ_+ of the shapes of background galaxies. It is related to the projected surface density $\Sigma(R)$ around lenses (Mandelbaum et al., 2013),

$$\Sigma(R) = \bar{\rho}_\mathrm{m} \int \left[1 + \xi_\mathrm{hm}(\sqrt{R^2 + \Pi^2}) \right] d\Pi, \tag{5.12}$$

via

$$\Delta\Sigma_+(R) = \gamma_+ \Sigma_\mathrm{cr} = \bar{\Sigma}(< R) - \Sigma(R). \tag{5.13}$$

In the equations above, $\bar{\rho}_\mathrm{m}$ is the mean mass density at z, Π is the line of sight separation measured from the lens, $\bar{\Sigma}(< R)$ is the average lens matter density within the projected distance R, and Σ_cr is the critical surface density for lensing. For a single source redshift

$$\Sigma_\mathrm{cr} = \frac{c^2}{4\pi G} \frac{D_\mathrm{s}}{D_\mathrm{d} D_\mathrm{ds}}, \tag{5.14}$$

where c is the speed of light in the vacuum, G is the gravitational constant, and D_d, D_s and D_ds are the angular diameter distances to the lens, to the source, and from the lens to the source, respectively.

5.5.2   Shear profile modelling

Stacked lensing by galaxy clusters is described in terms of three main terms. The treatment is simplified with respect to galaxy-galaxy lensing, when central haloes have to be differentiated from satellites and related additional terms contribute to the total shear profile.

Our treatment follows Covone et al. (2014). The dominant contribution up to $\sim 1~\mathrm{Mpc}\,h^{-1}$ comes from the central haloes, $\Delta\Sigma_\mathrm{BMO}$. We model this term as a smoothly truncated Navarro-Frenk-White (NFW) density profile (Baltz, Marshall, and Oguri, 2009, BMO),

$$\rho_\mathrm{BMO} = \frac{\rho_\mathrm{s}}{\frac{r}{r_\mathrm{s}}(1 + \frac{r}{r_\mathrm{s}})^2} \left(\frac{r_\mathrm{t}^2}{r^2 + r_\mathrm{t}^2} \right)^2, \tag{5.15}$$

where r_s is the inner scale length, r_t is the truncation radius, and ρ_s is the characteristic density. When fitting the shear profiles up to very large radii (ten times the virial radius and beyond), the truncated NFW model gives less biased estimates of mass and concentration with respect to the original NFW profile (Oguri and Hamana, 2011). The truncation removes the unphysical divergence of the total mass and better describes the transition between the cluster and the 2-halo term which occurs beyond the virial radius.

In the following, as a reference halo mass, we consider M_{200}, i.e., the mass in a sphere of radius r_{200}. The concentration is defined as $c_{200} = r_{200}/r_{\rm s}$. We set the truncation radius $r_{\rm t} = 3\,r_{200}$ (Covone et al., 2014; Oguri and Hamana, 2011).

The second contribution to the total profile comes from the off-centred clusters, $\Delta\Sigma_{\rm off}$. The BCG defining the cluster centre might be misidentified (Johnston et al., 2007), which leads to underestimate $\Delta\Sigma(R)$ at small scales and to bias low the measurement of the concentration. Furthermore, even if properly identified, the BCG might not coincide with the matter centroid, but this effect is generally very small and negligible at the weak lensing scale (George et al., 2012; Zitrin et al., 2012). The azimuthally averaged profile of clusters which are displaced by a distance $R_{\rm s}$ in the lens plane is (Yang et al., 2006)

$$\Sigma(R|R_{\rm s}) = \frac{1}{2\pi} \int_0^{2\pi} d\theta \Sigma_{\rm cen}(\sqrt{R^2 + R_{\rm s}^2 + 2RR_{\rm s}\cos\theta}), \tag{5.16}$$

where $\Sigma_{\rm cen}$ is the centred profile. We model the distribution of off-sets with an azimuthally symmetric Gaussian distribution (Hilbert and S. D. M. White, 2010; Johnston et al., 2007),

$$P(R_{\rm s}) = \frac{R_{\rm s}}{\sigma_{\rm s}^2} \exp\left[-\frac{1}{2}\left(\frac{R_{\rm s}}{\sigma_{\rm s}}\right)^2\right], \tag{5.17}$$

where $\sigma_{\rm s}$ is the scale length. The contribution of the off-centred haloes is then

$$\Sigma_{\rm off}(R) = \int dR_{\rm s} P(R_{\rm s})\Sigma(R|R_{\rm s}). \tag{5.18}$$

Typical scale lengths are of order of $\sigma_{\rm s} \sim 0.4~{\rm Mpc}\,h^{-1}$ (Johnston et al., 2007). Miscentring mainly matters with regard to an unbiased determination of the cluster concentration. Its effect is minor on the scales where the correlated matter manifests through the 2-halo term. We assume that a fraction $f_{\rm off}$ of the lenses is miscentred.

The third significant contribution to the total density profile is the 2-halo term, $\Delta\Sigma_{\rm 2h}$, which describes the effects of the correlated matter distribution around the location of the galaxy cluster at scales $\gtrsim 10$ Mpc. The 2-halo shear term around a single lens of mass M at redshift z for a single source redshift can be model as (Oguri and Hamana, 2011; Oguri and Takada, 2011)

$$\gamma_{+,2h}(\theta; M, z) = \int \frac{l\,dl}{2\pi} J_2(l\theta) \frac{\bar{\rho}_{\rm m}(z)b(M;z)}{(1+z)^3 \Sigma_{\rm cr} D_{\rm d}^2(z)} P_{\rm m}(k_l; z), \tag{5.19}$$

where θ is the angular radius, J_2 is the second order Bessel function, and $k_l \equiv l/[(1+z)D_{\rm d}(z)]$. $P_{\rm m}(k_l; z)$ is the linear power spectrum, which is computed following Eisenstein and Hu (1999). Given the observational errors on the shear measurements, more accurate computations of $P_{\rm m}$ have a negligible impact on the final result.

The final profile for the total differential projected surface density is then

$$\Delta\Sigma_{\text{tot}} = (1 - f_{\text{off}})\Delta\Sigma_{\text{BMO}} + f_{\text{off}}\Delta\Sigma_{\text{off}} + \Delta\Sigma_{\text{2h}}. \tag{5.20}$$

The above model has five free parameters: the mass M_{200} and the concentration c_{200} of the clusters; the fraction of off-centred haloes, f_{off}, and the scale length σ_{s} of the probability distribution of the off-sets; the product $b\,\sigma_8^2$, which determines the amplitude of the 2-halo term.

We consider only the cosmological information contained in the 2-halo term, whose signal is proportional to $\propto b\,\sigma_8^2$. Small-scale lensing has typically the best signal-to-noise ratio, but it may be subject to systematic uncertainties both in terms of theoretical interpretation and observational uncertainties (Mandelbaum et al., 2013). We do not try to connect it directly to the halo bias and the cosmological background. We just model it in terms of a physically motivated model, i.e., the (truncated) NFW profile. In this basic approach, the parameters M_{200} and c_{200} of the main haloes, as well as the parameters f_{off} and σ_{s} describing the miscentred clusters, can be seen as nuisance parameters that we marginalise over to measure the amplitude of the 2-halo term.

However, gravitational lensing presents an exclusive feature: it provides a direct measurement of the halo mass without relying on any scaling relation. The estimate of M_{200} can then be used to constrain the evolution of bias with the halo mass.

5.5.3 Measured profiles

We measure the lensing signal behind the 1176 clusters of the WHL12 catalogue centred in the four fields of the CFHTLenS. We extract the shear profiles between 0.1 and $30 \sim Mpch$ in 25 radial annuli equally distanced in logarithmic space. The procedure is described in Covone et al. (2014), which we refer to for details on shear calibration, selection of background galaxies, source redshift estimation and stacking.

Very briefly, the raw shear components in the CFHTLenS catalogue are corrected by applying a multiplicative and an additive parameter, empirically derived from the data. The background lensed galaxy population behind each galaxy cluster are selected by using a two colour selection in the g and r bands (Medezinski et al., 2010; Oguri et al., 2012), which can safely single out galaxies at $z \gtrsim 0.7$. We determine the tangential and cross component of the shear for each cluster from the weighted ellipticity of the background sources.

The clusters are finally stacked according to their optical richness. We adopt two binning schemes: either a single bin in optical richness comprising all clusters, which we will refer to in the following as our reference case, or four bins with comparable SNR ($12 \leq R_{L^*} < 16$, $16 \leq R_{L^*} < 21$, $21 \leq R_{L^*} < 30$ and $R_{L^*} \geq 30$), as already done in Covone et al. (2014).

5.5.4 Uncertainty covariance matrix

Due to stacking, shear observations at different radii are correlated. The effect is significant at radii larger than the typical lens angular separation (Mandelbaum et al., 2013). We estimate the uncertainty covariance matrix with a bootstrap procedure with replacement. We resample the clusters 10000 times. Covariance also accounts for the residual contribution from large scale projections, which is subdominant due to the large number of line of sights we stacked over.

The inverse of a noisy, unbiased estimator of the covariance matrix is not an unbiased estimator of the inverse covariance matrix (Hartlap, Simon, and Schneider, 2007; Mandelbaum et al., 2013). An unbiasing correction factor can be estimated under very restrictive statistical requirements, which are likely violated under usual observational conditions (Hartlap, Simon, and Schneider, 2007). Furthermore, the correction is negligible if the number of lenses is significantly larger than the number of radial bins. We prefer not to apply any correction.

An alternative approach requires the smoothing of the covariance matrix to create a noiseless version (Mandelbaum et al., 2013). The diagonal terms behave according to reproducible trends. The shape noise is the dominant source of variance at small radii. It scales like R^{-2} for logarithmically spaced annular bins. However, the total noise flattens at larger radii. There are two main reasons. First, when R is significantly larger than the typical separation between lenses, annular bins include many of the same sources around nearby lenses and the shape noise can not decrease by adding more lenses (Mandelbaum et al., 2013).

Secondly, when R is comparable with the field of view of the camera, an imperfect correction of the optical distortion can cause a tangential or radial pattern of the point spread function (PSF) ellipticities in the edge of the field of view. This coherent PSF anisotropy can then cause a residual systematic error (Miyatake et al., 2015). The field of view of CFHT/MegaCam is $1 \deg$ large, which corresponds to $\sim 12.9 \ \mathrm{Mpc}\, h^{-1}$ at the median redshift of the lens sample, $z \sim 0.37$.

Taking into account all the above sources of noise, the diagonal terms of the lensing uncertainty covariance matrix **V** can be modelled as (Mandelbaum et al., 2013):

$$\mathbf{V}(R_i, R_i) = A R^{-2} \left[1 + (R/R_{\mathrm{t}})^2 \right], \tag{5.21}$$

where R_{t} denotes the turn-around radius above which the shape noise is subdominant. A basic unweighted fit for the reference binning in optical richness ($R_{L^*} \geq 12$) gives $R_{\mathrm{t}} \sim 9.3 \ \mathrm{Mpc}\, h^{-1}$ (see Fig. 5.6).

The smoothing of the non-diagonal terms of the covariance matrix is more problematic. The two main sources of correlation are the cosmic variance (which is subdominant given the large number of line of sights in our sample) and the correlated shape noise due to the large R compared to the separation between lenses (Mandelbaum et al., 2013). These effects are difficult to model. Furthermore, a smoothing procedure might
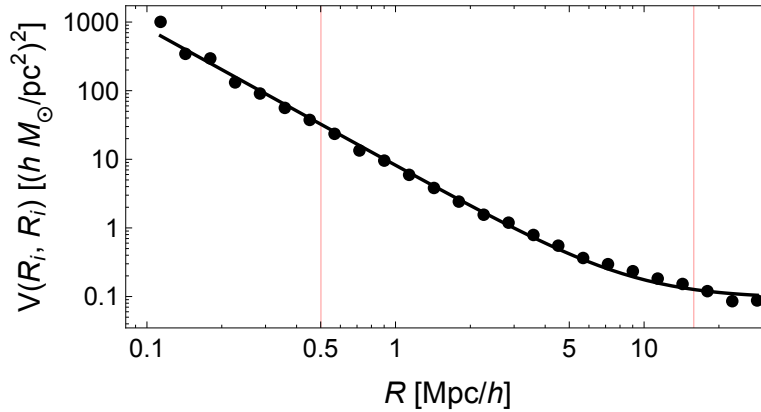
Figure 5.6: Diagonal terms of the lensing uncertainty covariance matrix of the total sample ($R_{L^*} \geq 12$) as a function of the transverse separation R. The matrix elements are estimated with a bootstrap procedure. The full black line plots the fitted smoothing function. Vertical red lines delimit the radial range considered when fitting the shear profiles.

bias low the estimated correlation of the elements near the diagonal. We then prefer to use the noisy version of the covariance matrix.

The uncertainty covariance matrix can be determined only when the number of clusters to stack js large enough. This is not the case for the less populated bins in optical richness. We then decide to use the full covariance matrix only for our reference case, whereas we take only the diagonal elements for the subsamples in optical richness in order to perform a coherent analysis when we look for trends with richness/mass.

5.5.5 Random catalogues

Residual systematic effects affecting the stacked shear profiles may come either from stacking over annuli which are largely incomplete due to the limited field of view or from other source of errors. These additional systematics are estimated by extracting the signal around random points with the same procedure used for the cluster lenses. We build a catalogue of 5046 random lenses with the same redshift and spatial distribution of the galaxy clusters. We realise 10000 bootstrap resamplings with replacement of the catalogue. The signal from the random pointings is consistent with zero up to $\sim 5 \ \mathrm{Mpc} \, h^{-1}$. The spurious signal at larger radii is likely due to residual systematics in the shear measurements at the edges of detector (Miyatake et al., 2015).

The shear profiles of the stacked clusters can be corrected for these residual systematics by subtracting the stacked signal estimated from the random catalogue. This correction rests on the assumption that the distribution of lenses is uncorrelated with residual systematics in the shape measurements (Miyatake et al., 2015), which holds in our analysis because the cluster catalogue and the shape measurements are taken from completely different data-sets.
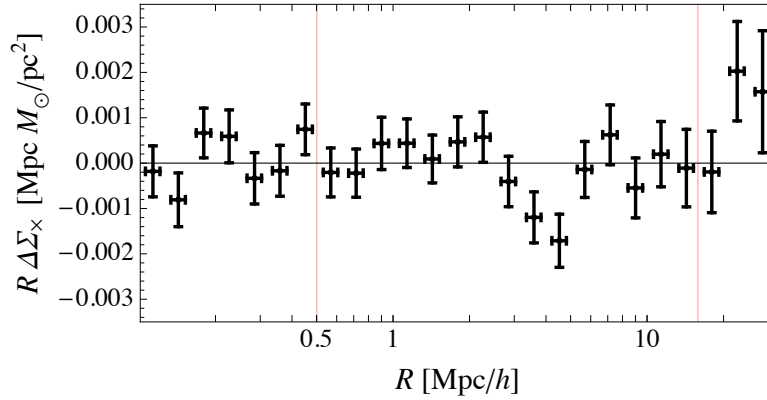
Figure 5.7: The renormalized cross component of the differential shear profile of the full sample of lensing clusters ($R_{L^*} \geq 12$) after correction for the residual signal. Vertical red line delimit the radial range considered when fitting the shear profiles.

After correction for the spurious signal, the cross component of the shear profile, $\Delta\Sigma_\times = \Sigma_{\text{cr}}\gamma_\times$, is consistent with zero at nearly all radii. This confirms that the main systematics have been eliminated. The radial profile of $\Delta\Sigma_\times$ for the full sample of clusters is plotted in Fig. 5.7. Most of the points are within 1-σ from the null value which might indicate somewhat over-estimated uncertainties. $\Delta\Sigma_\times$ increases at $R \gtrsim 20~\text{Mpc}\,h^{-1}$ but the deviation is not statistically significant.

5.5.6 Constraints

The corrected excess surface density for the total sample is plotted in Fig. 5.8. The signal is detected with high significance ($\text{SNR} \simeq 26.1$) over the full radial range. Stacked profiles for subsamples in optical richness can be found in Covone et al. (2014). Based on the analysis of the turn-around radius in the diagonal elements of the covariance matrix and the features of the shear profile $\Delta\Sigma_\times$, we limit our analysis to a maximum radius of $15.8 \sim \text{Mpc}\,h^{-1}$.

The choice of the lower limit for the radial range comes from a compromise between minimising the systematic errors due to contamination of cluster member galaxies and non-linear effects, and minimising the statistical errors (Mandelbaum, Seljak, and Hirata, 2008). We consider a minimum radius of $\sim 0.5\,\text{Mpc}\,h^{-1}$. Since to measure σ_8 we use only the information in the 2-halo term, which is dominant at very large radii, our final constraints are affected in a very negligible way by the choice of the lower fitting radius, which mainly impacts the determination of the effective concentration of the stacked clusters.

Radial fits are then performed between 0.5 and $15.8 \sim \text{Mpc}\,h^{-1}$ (15 equally spaced points in logarithmic scale). The statistical analysis is based on a χ^2 function,

$$\chi^2_{\text{WL}} = \sum_{i,j} \left[\Delta\Sigma_{\text{obs},i} - \Delta\Sigma_{\text{th},i}\right] \mathbf{V}^{-1}_{ij} \left[\Delta\Sigma_{\text{obs},j} - \Delta\Sigma_{\text{th},j}\right], \tag{5.22}$$
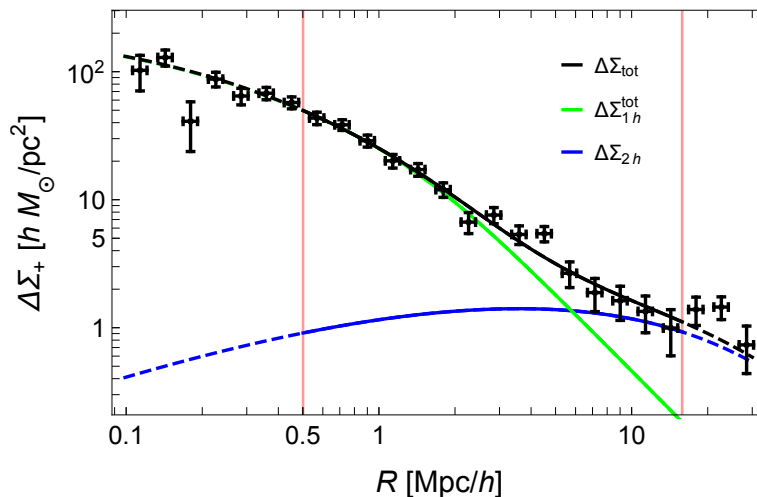
Figure 5.8: Stacked differential surface density $\Delta\Sigma_+$ after correction for the residual signal as a function of radius for clusters with optical richness $R_{L^*} \geq 12$. Black points are our measurements. The vertical error bars show the square root of the diagonal values of the covariance matrix. The horizontal lines are the weighted standard deviations of the distribution of radial distances in the annulus. The green line plots the contribution from the galaxy cluster haloes (i.e., the sum of lensing contributions from centred and offset lenses); the blue line describes the 2-halo term; the black line is the overall fitted radial profile. Vertical red lines delimit the radial range considered when fitting the shear profiles. Dashed lines are extrapolations based on the best fit model, which was determined in the radial range $0.5 < R < 15.8\,\mathrm{Mpc}/h$.

where $\mathbf{V}^{-1}$ is the inverse of the uncertainty covariance matrix, $\Delta\Sigma_{\mathrm{obs},i}$ is the observed excess density at radius R_i, and $\Delta\Sigma_{\mathrm{th}}$ is the theoretical prediction of the halo model. We adopt uniform priors for the fitting parameters and sampled the posterior probability with four Monte Carlo Markov chains. Results are summarised in Tables 5.1 and 5.2.

For the reference sample, the product $b\,\sigma_8^2$ is recovered with an accuracy of ~ 20 per cent. This estimate is stable against variation in the fitting procedure, which reassure us about the proper treatment of systematics (see Table 5.1). As far as we consider a truncated model for the lenses, the final results on $b\,\sigma_8^2$ are nearly independent of the specific modelling. The variations in the estimated $b\,\sigma_8^2$ due to different assumptions on the truncation radius of the Σ_{BMO} profile are not significant and they are much smaller than the statistical uncertainty. The case of the divergent NFW model is different. This model is unphysical at scales well beyond the virial radius and it would severely under-estimate the contribution of the 2-halo term.

We check that the results of our analysis are very similar whether using the full covariance matrix or only the diagonal terms. Neglecting the covariance in the shear measurements of near radial bins does not affect the central estimate. On the other hand, the uncertainties on the fitting parameters are slightly smaller. This agreement further supports our choice of using the (noisy) covariance matrix without any correction.

Assumption	$b\,\sigma_8^2$
reference	1.56 ± 0.35
$r_{\rm t} = 4\,r_{200}$	1.52 ± 0.34
$r_{\rm t} = 2\,r_{200}$	1.63 ± 0.34
NFW	0.96 ± 0.42
diagonal covariance	1.54 ± 0.28
$f_{\rm off} = 1$	1.58 ± 0.33
$r_{\rm max} = 20\ {\rm Mpc}\,h^{-1}$	1.73 ± 0.32
$r_{\rm max} = 30\ {\rm Mpc}\,h^{-1}$	1.86 ± 0.29
$r_{\rm min} = 0.1\ {\rm Mpc}\,h^{-1}$	1.55 ± 0.33
$r_{\rm min} = 0.2\ {\rm Mpc}\,h^{-1}$	1.55 ± 0.34

Table 5.1: Product $b\,\sigma_8^2$ (col. 2) for the reference sample ($R_{L^*} \geq 12$) as determined with the stacked lensing analysis under different assumptions. In col. 1, we report the difference in the fitting procedure with respect to the 'reference' case. All else being equal, we consider: different priors on the truncation radius $r_{\rm t}$ of the BMO model of the central haloes; a standard NFW model; a uncertainty covariance matrix with null off-diagonal elements; no miscentred haloes; different thresholds for either the maximum ($r_{\rm max}$) or the minimum ($r_{\rm min}$) fitting radius.

As expected, a different minimum radius in the fitting procedure has no effect on the estimate of the bias, which only depends on the signal at scales $\gtrsim 10\ {\rm Mpc}\,h^{-1}$. The inclusion of small scales affects nevertheless the estimate of the mass and of the concentration of the central halo. At scales $R \sim 0.1\ {\rm Mpc}\,h^{-1}$ a proper modelling of the lens requires the treatment of the BCG and of the baryonic component. Similar considerations hold for the treatment of the miscentred haloes too. The fraction of haloes with off-sets has a negligible impact on the estimate of the bias.

Finally, the inclusion of shear measurements at large radial scales not fully covered by the field of view can bias the results.

5.6 Joint analysis

In this section, we combine lensing and clustering to infer σ_8 and the halo bias. At the large scales probed by clusters of galaxies, we can safely consider the bias as linear. For each binning in optical richness, we can measure the weighted bias

$$b(M_{\rm eff}, z) = \int b(M_{200}, z) f_{\rm sel}(M_{200}) dM_{200}, \tag{5.23}$$

where $f_{\rm sel}(M_{200})$ is the selection function,

$$f_{\rm sel}(M_{200}) = \int_{R_{L^*}^{\rm min}}^{R_{L^*}^{\rm max}} P(M_{200}|R_{L^*}) n(R_{L^*}) dR_{L^*}, \tag{5.24}$$

$n(R_{L^*})$ is the distribution of the observed richness, $R_{L^*}^{\rm min}$ and $R_{L^*}^{\rm max}$ delimit the richness bin, and $P(M_{200}|R_{L^*})$ embodies the mass-richness scaling relation through the
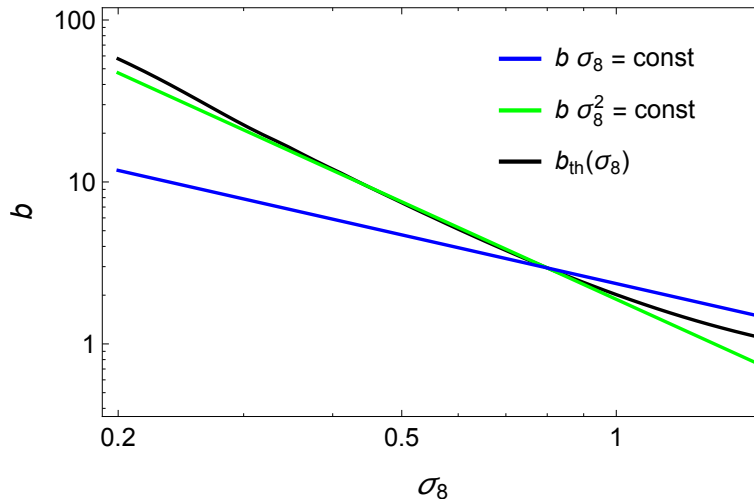
Figure 5.9: Main degeneracies between bias and σ_8 as probed by either clustering (blue line), lensing (green line), or a theoretical modelling of the bias (black line). Theoretical predictions are based on J. L. Tinker et al. (2010). We consider $\sigma_8 = 0.8$ and the bias of a halo with mass $M_{200} = 10^{14} M_\odot / h$ at $z = 0.3$.

conditional probability that a cluster with richness R_{L*} has a mass M_{200}.

The big advantage of using the same clusters to measure lensing and clustering is that we do not need to model the bias to infer the amplitude σ_8. We are assured that we observe the same weighted bias, which is written in terms of an effective mass M_{eff}, for both lensing and clustering. We do not need to determine the effective mass to estimate σ_8, even though M_{eff} can be constrained with the lensing fit of the central haloes.

This basic approach does not need any derivation of the scaling relation between the observable (the optical richness in our case) and the cluster mass. The effects of the cluster selection function and of the scaling relation are included in the effective bias. In this way, we avoid two of the main difficulties which plague cosmological tests based on cluster of galaxies (Sereno and Ettori, 2014; Sereno, Ettori, and Moscardini, 2015).

Bias and σ_8 can be computed by properly matching the constraints obtained with either lensing (which is degenerate with $b\,\sigma_8^2$) and clustering (which is degenerate with $b\,\sigma_8$). Degeneracies between bias and σ_8 which affect each of the two probes are pictured in Fig. 5.9. Results are summarised in Table 5.2. We explore two methods to infer σ_8 according to whether or not the information on the mass halo, which is inferred from the small scales in the lensing analysis, is used to infer the amplitude of the power spectrum, σ_8.

5.6.1 First method

The first proposed method is the most basic. It consists in a simultaneous analysis of σ_8 and bias. It uses only the cosmological information derived from the 2-halo term in the lensing modelling. Together with σ_8, we can then determine the halo bias b_i for each
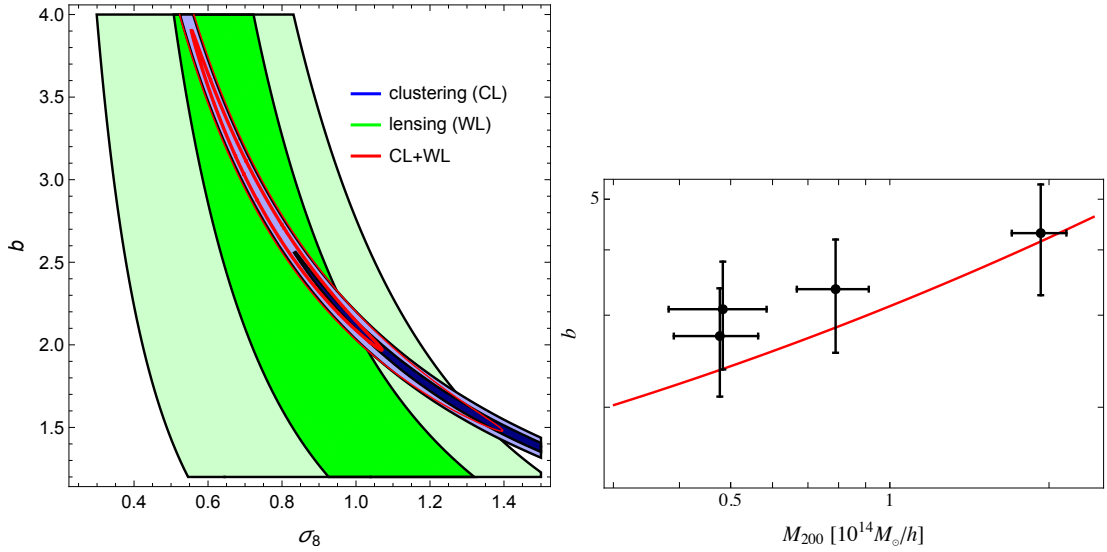
Figure 5.10: *Left Panel.* Derived probability density of bias b and σ_8 in the reference case ($R_{L_*} \geq 12$). The green (blue) regions include the confidence regions as obtained from lensing (clustering). The darker (lighter) area includes the 1-(3-)σ confidence region in two dimensions, here defined as the region within which the value of the probability is larger than $\exp(-2.3/2)$ ($\exp(-11.8/2)$) of the maximum. The red thick (thin) contour includes the 1-(3-)σ confidence regions from the joint analysis. *Right Panel.* Bias as a function of mass. The red line is the prediction by J. L. Tinker et al. (2010) for $\sigma_8 = 0.8$ at $z = 0.37$.

binning in optical richness. This method fully exploits the fact that we are measuring clustering and lensing for the same clusters, which are selected based on their richness. The determination of σ_8 does not require the modelling of the halo bias as a function of mass/richness.

The joint analysis is performed with the combined likelihood

$$\mathscr{L}_{\text{tot}}\left(\sigma_8, \{b_i\}\right) \propto \prod_i \mathscr{L}_{\text{GL},i} \mathscr{L}_{\text{CL},i}, \tag{5.25}$$

where $\mathscr{L}_{\text{CL},i}$ is the clustering likelihood for the i-th richness bin, see Eq. (1.85). The dependence on σ_z is marginalised over. The lensing likelihood, $\mathscr{L}_{\text{GL},i}(b_i \, \sigma_8)$, is obtained by marginalising the posteriori probability distribution obtained with the stacked lensing analysis of the i-th bin, see § 5.5.6. We adopt uniform priors for σ_8 and the bias. Results for the reference case are reported in Table 5.2. We find $\sigma_8 = 0.79 \pm 0.16$ and a bias of 2.86 ± 0.78. Confidence regions are plotted as red contours in Fig. 5.10. Even though the lensing constraints are quite shallow with respect to the clustering results, they are crucial to break the degeneracy between bias and power spectrum amplitude.

The lensing constraints are exactly degenerate with the contours where $b \, \sigma_8^2$ is constant whereas the constraints from clustering align to a very good approximation with the loci of points where $b \, \sigma_8$ is constant. The latter degeneracy would be exact

if the cluster-cluster correlation function are measured in the real space. A simplified joint likelihood can be written in terms of the χ^2-function

$$\chi^2 = \sum_i \left(\frac{\left[b\,\sigma_8^2\right]_i - b_i\sigma_8^2}{\delta\left[b\,\sigma_8^2\right]_i} \right)^2 + \left(\frac{\left[b\,\sigma_8\right]_i - b_i\sigma_8}{\delta\left[b\,\sigma_8\right]_i} \right)^2, \tag{5.26}$$

where the sum runs over the different richness bins; $\left[b\,\sigma_8^2\right]_i$ and $\left[b\,\sigma_8\right]_i$ are the measurements from lensing and clustering in the i-th bin, respectively. For the following tests, we use the simplified version of the likelihood.

We first check for consistency. Estimates of σ_8 obtained considering subsamples in optical richness one at a time are in agreement among themselves and with the reference case. We get $\sigma_8 = 0.92 \pm 0.27$ for $12 \leq R_{L^*} < 16$, $\sigma_8 = 0.59 \pm 0.24$ for $16 \leq R_{L^*} < 21$, $\sigma_8 = 0.80 \pm 0.29$ for $21 \leq R_{L^*} < 30$ and $\sigma_8 = 0.57 \pm 0.22$ for $R_{L^*} \geq 30$.

Being the estimates consistent, we can analyse the four subsamples together. In this way we can measure at the same time the halo bias in each richness bin and the amplitude of the power spectrum. We find $\sigma_8 = 0.69 \pm 0.15$, which is fully consistent with the reference case.

The measured halo bias is an increasing function of the optical richness, see Table 5.2. Stacked lensing also provide direct estimates of effective masses thanks to the modelling of the main halo term. We can then look for trends of b with mass without assuming any scaling relation. The bias increases with mass in agreement with results from theoretical predictions, see Fig. 5.9.

We remark that we use the small scale regime only to derive the halo mass whereas we do not try to extract constraints on the bias from the regions within the viral radius. The determination of σ_8 and of the bias for each bin was independent of the small scale-regime, which enters only when we studied the evolution of bias with mass. In this scheme the effective mass is identified with the lensing mass, which is an acceptable approximation for stacking analyses in physical length units (Okabe et al., 2013; Umetsu et al., 2014).

5.6.2   Second method

In the second approach, we focus on the determination of σ_8 by assuming that the bias is a known cosmological function of the peak height (Bhattacharya et al., 2013; J. L. Tinker et al., 2010). This requires the knowledge of the halo mass, which is determined with the stacked lensing. The weight factor when stacking in physical length units is mass-independent and estimated masses and concentration are not biased (Okabe et al., 2013; Umetsu et al., 2014). We then assume that the effective mass measured by lensing for the central halo is the same effective mass probed by the bias, see Eq. (5.23), which strictly holds if the signals are linear in mass. The quantitative analysis can be

performed in terms of a χ^2 function,

$$\chi^2\left(\sigma_8, \{M_{200,i}\}\right) = \sum_i \left[\frac{\left(\left[b\,\sigma_8^2\right]_i - b_{\mathrm{th},i}\sigma_8^2\right)^2}{\delta\left[b\,\sigma_8^2\right]_i^2 + \delta\left[b_{\mathrm{th},i}\right]^2\sigma_8^4} \right.$$
$$\left. + \frac{\left(\left[b\,\sigma_8\right]_i - b_{\mathrm{th},i}\sigma_8\right)^2}{\delta\left[b\,\sigma_8\right]_i^2 + \delta\left[b_{\mathrm{th},i}\right]^2\sigma_8^2} + \left(\frac{M_{200,i} - M_{200,i}^{\mathrm{obs}}}{\delta M_{200,i}^{\mathrm{obs}}}\right)^2 \right]. \quad (5.27)$$

where $b_{\mathrm{th},i} = b_{\mathrm{th},i}(\sigma_8, z_i, M_{200,i})$ is the theoretical prediction for given σ_8 and halo mass $M_{200,i}$ at redshift z_i and $\delta\left[b_{\mathrm{th},i}\right]$ is the related uncertainty. We use the fitting formula for the bias derived in J. L. Tinker et al. (2010). They found a six per cent scatter about their best-fit relation, which we conservatively adopted as the uncertainty on the theoretical prediction.

Differently from the first approach, where the biases themselves are free parameters, now they are expressed in terms of M_{200}. Since the masses are already constrained by the lensing analysis, we add to the χ^2 function a penalty term, i.e., the third right hand term in Eq. (5.27), and we still formally consider the mass associated to each bin as a parameter to be determined. Of course, the posterior estimate of each $M_{200,i}$ just follows the prior but we had to include the penalty not to underestimate the error on σ_8. As for the first approach, the second method still does not need to calibrate the mass-richness relation.

For the reference binning in optical richness ($R_{L^*} \geq 12$), we obtain $\sigma_8 = 0.75 \pm 0.08$, in agreement with what obtained with the first approach. The use of the information on the dependence of the bias on the peak height nearly halve the statistical error. The theoretical constraint on the bias is nearly degenerate with the lensing one, i.e., b_{th} is nearly proportional to the inverse squared σ_8. Constraints from clustering, lensing or theoretical predictions are compared in Fig. 5.9. However, we can not use the theoretical constraint without the information on mass from lensing.

5.7 Forecasting

The accuracy in the determination of σ_8 will greatly benefit from future optical galaxy surveys. As a test bed, we consider the wide survey planned by the Euclid mission (Amendola et al., 2013; Laureijs et al., 2011) [2]. The signals of either lensing or clustering can be enhanced by considering a larger number of clusters (which can be achieved with either deeper or wider surveys), a larger number of background sources (deeper surveys) and a larger survey area in order to cover the lensing 2-halo term up to 50 Mpc (wider surveys). With regard to these three aspects, Euclid will represent a significant improvement with respect to the data-sets we considered here.

Euclid will observe an area of $15000\ \mathrm{deg}^2$ and it is expected to detect $n_{\mathrm{g}} \sim 30$ galaxies per square arcminute with a median redshift greater than 0.9, that can be used for weak lensing analyses (Laureijs et al., 2011). These basic properties are enough

---

[2]http://www.euclid-ec.org/

to forecast the expected accuracy in the σ_8 determination from the joint lensing plus clustering analysis we presented.

The area of the Euclid survey is nearly 2 times larger than the area we considered in the clustering analysis and nearly 100 times wider than the CFHTLenS, with a corresponding expected improvements in the corresponding signals.

Due to improved photometry, a larger number of clusters will be detected to higher redshifts. Most of the newly detected clusters will be low mass haloes producing a small lensing signal. On the other hand, Euclid will significantly extend the redshift range of the background galaxies, whose lensing signal is maximised at high redshift.

Recently, Ford et al. (2015) presented the CFHTLenS 3D-Matched-Filter catalogue of cluster galaxies. Candidate clusters where selected if they had at least two member galaxies within the virial radius and a detection significance in excess of 3.5. More than $N_{\mathrm{cl}} \sim 18000$ clusters were detected in the $\sim 150 \, \mathrm{deg}^2$ area of the survey in the redshift range $0.2 \lesssim z \lesssim 0.9$. More than 14000 candidate clusters had an estimated $N_{200} > 10$. By comparison, with SDSS-III quality data, Wen, Han, and Liu (2012) detected $N_{\mathrm{cl}} \sim 1200$ clusters with $N_{200} \gtrsim 8$ in the redshift range $0.1 < z < 0.6$ over the area of $\sim 130 \, \mathrm{deg}^3$ in common with the CFHTLenS. We can conclude than nearly 10 times more clusters can be identified by increasing the photometric depth of the survey from SDSS-III to CFHTLenS quality data.

The Euclid mission is expected to identify an even larger number of clusters. Nevertheless, a significant number of them will be made of small groups, whose photometric redshift determination might be uncertain, which hampers the clustering analysis. Furthermore, the larger the number of identified clusters, the larger their density in the sky. As we have seen, the shot noise is not the only source of uncertainty at large radii. If we consider clusters whose mean separation is smaller than the range over which we measure the shear profile, we can not simply rescale the lensing signal-to-noise ratio as $\mathrm{SNR} \propto \sqrt{N_{\mathrm{cl}}}$. We can then conservatively consider an improvement of a factor ~ 10 in the clustering/lensing signal detected by Euclid with respect to the present analysis due to the larger density of detected clusters.

The background lensed galaxies resolved by Euclid will be more and further away than the sources in the CFHTLenS. The number density of galaxies in the CFHTLenS with shear and redshift data is $n_{\mathrm{gal}} \sim 17$ galaxies per square arcminute (Heymans et al., 2012). The effective weighted galaxy number density that is useful for a lensing analysis is $n_{\mathrm{gal}} \sim 11$ galaxies per square arcminute in the redshift range $0.2 < z < 1.3$ with a median redshift of $z \sim 0.75$ (Heymans et al., 2012), and it is ~ 6 galaxies per square arcminute at $z \gtrsim 0.7$ (Covone et al., 2014). Euclid sources will be more numerous ($n_{\mathrm{g}} \sim 30$ galaxies per square arcminute) and at a median redshift of ~ 0.9. These two factors make the signal behind a lens nearly two times larger.

Finally, the wide coverage of the Euclid survey will enable us to detect the 2-halo lensing signal to its full radial extent. The extension of the radial coverage from 15 up to $30 \, \mathrm{Mpc} \, h^{-1}$ can decrease the errors in the lensing estimate of $b \, \sigma_8^2$ from $\gtrsim 20$ to ~ 15 per cent, see Table 5.1. The improvement would be even more significant considering radii

up to $50 \ \mathrm{Mpc} \, h^{-1}$ but this effect would be counterbalanced by the increased overlap in the lensing area of near clusters.

Based on the above considerations, we expect that stacked lensing can measure $b \, \sigma_8^2$ with an accuracy of ~ 0.3 per cent and that clustering can measure $b \, \sigma_8$ with an accuracy of ~ 0.1 per cent. The combined effects of a larger sample of clusters and less noisy measurements should be enough to get an accuracy $\delta \sigma_8 \sim 0.003$ with the Euclid mission without any assumption on the mass-richness scaling or any modelling of the halo bias.

In the present analysis we could keep Ω_{M} fixed because of the large statistical uncertainties. This will be no more the case in presence of Euclid quality data. On one hand, the dependence on Ω_{M} of the joint clustering plus lensing analysis enlarge the forecasted statistical uncertainty on σ_8. On the other hand, Ω_{M} could be determined to very good accuracy by exploiting other features of the joint analysis. These effects should counterbalance each other and the expected $\delta \sigma_8$ should be nearly unchanged.

The estimate of σ_8 will also greatly benefit from the increased spectroscopic sample associated to the Euclid survey. Working with spectroscopic rather than photometric redshift eliminates one of the main sources of uncertainty in the clustering analysis, see § 5.4.4.

The high precision in Euclid measurements will demand for very accurate theoretical modelling. The bias is a stochastic process which is difficult to model. In this sense our basic approach, where the bias is treated as an effective parameter, is very promising.

	Lensing			Clustering			Combined	
	N_{cl}	M_{200}	$b\,\sigma_8^2$	N_{cl}	$b\,\sigma_8$	σ_z	σ_8	b
$R_{L*} \geq 12$	1176	0.69 ± 0.11	1.56 ± 0.35	69527	2.29 ± 0.08	0.015 ± 0.003	0.79 ± 0.16	2.86 ± 0.78
$12 \leq R_{L*} < 16$	476	0.48 ± 0.09	1.87 ± 0.46	29130	1.87 ± 0.08	0.017 ± 0.003	0.69 ± 0.15	2.74 ± 0.64
$16 \leq R_{L*} < 21$	347	0.48 ± 0.10	1.43 ± 0.57	21047	2.12 ± 0.08	0.016 ± 0.003		3.08 ± 0.72
$21 \leq R_{L*} < 30$	216	0.79 ± 0.12	2.02 ± 0.68	11962	2.30 ± 0.16	0.015 ± 0.004		3.36 ± 0.82
$30 \leq R_{L*}$	137	1.92 ± 0.23	1.86 ± 0.83	7388	2.97 ± 0.16	0.012 ± 0.002		4.31 ± 1.03

Table 5.2: Results from the stacked lensing (cols. 2, 3, and 4) and the clustering (cols. 5, 6, and 7) analysis of different binning in optical richness R_{L*} (col. 1). For the lensing part: number of clusters N_{cl} in the bin (col. 2); estimated cluster mass M_{200} (col. 3); product $b\,\sigma_8^2$ (col. 4). For the clustering: number of clusters N_{cl} in the bin (col. 5); product $b\,\sigma_8$ (col. 6); estimated redshift error σ_z (col. 7). Bias b and σ_8 from the combined analysis are reported in cols. 8 and 9, respectively. Reported values of central estimate and dispersion are the bi-weight estimators of the posterior probability densities. Masses are in units of $10^{14} M_\odot/h$.

Chapter 6

Conclusions

In this Thesis we presented new cosmological constraints from clustering and stacked lensing of galaxy clusters. The main scientific results achieved in this work can be summarised as follows:

We started our analysis focusing on the BAO detection in the monopole of the 2PCF of galaxy clusters. The main achievements are the following:

- we compiled a large spectroscopic cluster sample by cross-matching the angular positions of the cluster BCGs from the SDSS DR8 sample by Wen, Han, and Liu (2012) with the positions of the BOSS galaxies, (Alam et al., 2015), in order to asses the spectroscopic redshifts of the BCGs. We then constructed random samples that accurately account for all the systematics. Our full spectroscopic sample consists of 69035 clusters in the redshift range $0.1 < z < 0.6$. This expands the work showed in Veropalumbo et al. (2014);

- we measure the redshift-space 2PCF and detect the BAO peak at 4σ confidence level. This is the most accurate BAO peak detection for galaxy clusters ever achieved. We found the distance $D_v = 989\pm^{22}_{25} \; \mathrm{Mpc}\, h^{-1}$ when combining with sound horizon measurements (Planck Collaboration et al., 2016), and the uncalibrated distance $D_v/r_s = 9.6\pm^{0.2}_{0.2}$, in good agreement with ΛCDM predictions;

- we computed the covariance matrix for the 2PCF measurements using the jackknife resampling technique (Norberg et al., 2009); by comparing with the analytic covariance matrix (Grieb et al., 2016) we showed, that our estimate overpredicts the variance by a factor ~ 2, as expected; thus our results can be considered conservatives;

- we measured the projected correlation function to infer the bias, finding $b\sigma_8 = 2.03 \pm 0.03$ for $\Omega_M = 0.25$, $b\sigma_8 = 2.27 \pm 0.03$ for $\Omega_=0.30$ and $b\sigma_8 = 2.48 \pm 0.04$ for $\Omega_M = 0.35$. The χ^2 comparison suggests that $\Omega_M = 0.25$ is preferred. This value is significantly higher than the bias of galaxies in the BOSS sample, confirming the goodness of the cluster selection (Alam et al., 2016; Anderson et al., 2014);

- we modelled the full shape of the correlation function monopole, obtaining $\Omega_M h^2 = 0.116\pm^{0.010}_{0.009}$; that is slightly lower with respect to CMB based constraints. However, it has to be noted that the covariance with other model parameters is neglected in this work, as we chose to vary the matter density parameter only;

- we showed that there in no need to use the reconstruction technique in cluster clustering analysis (§ 1.5.4), or to include non-linear predictions for the matter power spectrum, as the BAO signal is compatible with the one predicted by linear theory, considering the estimated uncertainties;

- we investigated the small-scale clustering using the cartesian 2D 2PCF and, modelling RSD with the dispersion model. We found the fingers-of-God signal at very low significance, being $\sigma_{12} = 430\pm^{370}_{250}$ km/s, compatible with 0 at $< 2\sigma$. We also obtained $f\sigma_8 = 0.3\pm^{0.3}_{0.2}$, $b\sigma_8 = 2.0\pm^{0.1}_{0.1}$. Anyway, since for these constraints we used only the diagonal terms of the covariance matrix, the posterior variance is likely underestimated.

Since we detected the BAO peak at different redshift, we could obtain the first observational constraints on the distance-redshift relation using only the clustering properties of galaxy clusters (§ 4). Specifically:

- we splitted the cluster sample in three redshift ranges. The catalogues have been constructed by matching the BCGs from the WHL12 catalogue (Wen, Han, and Liu, 2012), with spectra from SDSS DR7 (Abazajian et al., 2009) and SDSS DR12 (Alam et al., 2015). This allowed us to construct three catalogues of galaxy clusters – Main-GCS, LOWZ-GCS and CMASS-GCS – at the median redshifts $z = 0.2$, 0.3 and 0.5, respectively. The number of objects is 12910, 42215, and 11816, respectively;

- we then estimated the covariance matrix using both internal error estimators (jackknife and bootstrap) and the lognormal mock method (Coles and Jones, 1991). These estimators provide fairly consistent errors, with internal errors more conservative and scattered. We chose the lognormal mock covariance matrix estimate as reference for this analysis;

- the BAO feature is detected with a significance larger than 2σ, for all the considered samples. For the three samples analysed we got: $\alpha(z = 0.2) = 0.96 \pm 0.06$, $\alpha(z = 0.3) = 0.99 \pm 0.03$ and $\alpha(z = 0.5) = 0.99 \pm 0.03$, respectively. This translates to the uncalibrated distance estimates: $r_s/D_V(z = 0.2) = 0.18 \pm 0.01$, $r_s/D_V(z = 0.3) = 0.124 \pm 0.004$, $r_s/D_V(z = 0.5) = 0.080 \pm 0.002$. We used the sound horizon estimate from Planck Collaboration et al. (2014b) to calibrate the distances, obtaining: $D_V(z = 0.2) = 800 \pm 50\,\mathrm{Mpc}$, $D_V(z = 0.3) = 1183 \pm 35$, $D_V(z = 0.5) = 1832 \pm 55$;

- the derived distance constraints are competitive with respect to other estimates from the BAO peak obtained using richer galaxy catalogues, such as 6dFGS (Beutler et al., 2011) and WiggleZ (Blake et al., 2011). As expected, these results are instead not comparable, in precision, with the constraints coming from the BOSS survey, of which our BCGs represent a subsample, when reconstruction is applied. However, it is worth to notice that the detection for the LOWZ-GCS is

comparable to the unreconstructed BAO detection from the whole LOWZ galaxy sample (Anderson et al., 2014), despite the latter has ~ 10 times more objects;

- we then used both the uncalibrated and calibrated distance estimates to derive cosmological constraints. Our results are all consistent with the cosmological model supported by the Planck results (see Planck Collaboration et al., 2014b).

Finally, we modelled the clustering of galaxy clusters in joint analysis with weak lensing information (§ 5), to put constraints on b and σ_8 separately:

- we considered a sample of 69527 galaxy clusters from the WHL12 with photometric redshift in the range $0.1 < z < 0.6$ in the Northern Galactic Cap. For the lensing sample, we considered the 1176 clusters from the CFHTLens survey.

- we computed the 2PCF monopole, and modelled it with a damped 2PCF model, to account for the distortions introduced by the photometric redshift errors, obtaining $b\sigma_8 = 2.29 \pm 0.08$;

- by measuring the stacked lensing signal we obtained $b\sigma_8^2 = 1.87 \pm 0.46$;

- we determined the power spectrum amplitude with an accuracy $\delta\sigma_8 \gtrsim 0.1$. Even though we fixed $\Omega_{\rm M} = 0.3$ in our analysis, the statistical error is too large to discriminate between the discrepant estimates of σ_8 from either number counts (Planck Collaboration et al., 2014b) or CMB (Planck Collaboration et al., 2014a). The method is nevertheless promising for its minimal modelling and well controlled systematics. Our estimation of σ_8 does not rely on any mass-observable scaling relation;

- we measured the linear bias as a function of cluster mass, in the mass range $0.5 \lesssim M_{200}/(10^{14} M_\odot/h) \lesssim 2$. The bias scales with mass according to theoretical predictions in excellent agreement with results from dark matter N-body simulations (Bhattacharya et al., 2013; J. L. Tinker et al., 2010). Thanks to the minimal modelling of the employed method, we could obtain this result bypassing the calibration of the scaling relation between cluster mass and observable.

All the algorithms to perform the described analyses have been implemented within the CBL software (§ 2 Marulli, Veropalumbo, and Moresco, 2016).

All the results presented in this Thesis, clearly demonstrate that galaxy clusters are powerful tracers of the cosmic density field and can be efficiently exploited for BAO analyses. Despite the paucity of cluster samples, with respect to generally larger galaxy samples, the higher values of cluster bias and the fact that their redshifts are less distorted by random motions improve the clustering signal, that results almost insensitive to non-linear dynamical distortions. This reflects in a sharper BAO peak in the 2PCF, close to the prediction of linear theory. We also showed that by combining clustering and weak gravitational lensing, it is possible to disentangle the bias and the power spectrum amplitude constraints, by assuming a minimal-modelling. To further

tighten the cosmological constraints obtained in this work, these statistics should be combined with other cosmological probes, such as the cluster mass function.

The techniques presented here will be further exploited in the next future on the increasingly large collections of data expected from new experiments like e.g. Euclid (Amendola et al., 2013; Laureijs et al., 2011; Sartoris et al., 2016), eBOSS (Dawson et al., 2015) and eROSITA (Merloni et al., 2012). Galaxy cluster samples and dedicated spectroscopic follow-ups will provide in fact an independent tracer of the dark matter density field, with respect to the typical emission line galaxies, targets of many future experiments. We will also extend the cluster clustering analysis considering the anisotropic 2PCF, that is measuring the multipoles and the wedges and modelling their full shape. The final goal will be to join, in one single likelihood, all the cosmological probes that galaxy clusters can provide.

Bibliography

Abazajian, K. N. et al. (2009).
"The Seventh Data Release of the Sloan Digital Sky Survey".
In: ApJS 182, 543-558, pp. 543–558. DOI: 10.1088/0067-0049/182/2/543.
arXiv: 0812.0649.

Aihara, H. et al. (2011).
"The Eighth Data Release of the Sloan Digital Sky Survey: First Data from SDSS-III".
In: ApJS 193, 29, p. 29. DOI: 10.1088/0067-0049/193/2/29.
arXiv: 1101.1559 [astro-ph.IM].

Alam, S. et al. (2015). "The Eleventh and Twelfth Data Releases of the Sloan Digital Sky
Survey: Final Data from SDSS-III". In: ApJS 219, 12, p. 12.
DOI: 10.1088/0067-0049/219/1/12. arXiv: 1501.00963 [astro-ph.IM].

Alam, S. et al. (2016).
"The clustering of galaxies in the completed SDSS-III Baryon Oscillation
Spectroscopic Survey: cosmological analysis of the DR12 galaxy sample".
In: *ArXiv e-prints*. arXiv: 1607.03155.

Allen, S. W., A. E. Evrard, and A. B. Mantz (2011).
"Cosmological Parameters from Observations of Galaxy Clusters".
In: ARA&A 49, pp. 409–470. DOI: 10.1146/annurev-astro-081710-102514.
arXiv: 1103.4829 [astro-ph.CO].

Alonso, D. (2012). "CUTE solutions for two-point correlation functions from large
cosmological datasets". In: *ArXiv e-prints*. arXiv: 1210.1833 [astro-ph.IM].

Amendola, L. et al. (2013).
"Cosmology and Fundamental Physics with the Euclid Satellite".
In: *Living Reviews in Relativity* 16. DOI: 10.12942/lrr-2013-6.
arXiv: 1206.1225.

Anderson, L. et al. (2012).
"The clustering of galaxies in the SDSS-III Baryon Oscillation Spectroscopic Survey:
baryon acoustic oscillations in the Data Release 9 spectroscopic galaxy sample".
In: MNRAS 427, pp. 3435–3467. DOI: 10.1111/j.1365-2966.2012.22066.x.
arXiv: 1203.6594.

Anderson, L. et al. (2014).
"The clustering of galaxies in the SDSS-III Baryon Oscillation Spectroscopic Survey:
baryon acoustic oscillations in the Data Releases 10 and 11 Galaxy samples".
In: MNRAS 441, pp. 24–62. DOI: 10.1093/mnras/stu523. arXiv: 1312.4877.

Angulo, R. E. et al. (2005). "Constraints on the dark energy equation of state from the
imprint of baryons on the power spectrum of clusters".

In: MNRAS 362, pp. L25–L29. DOI: `10.1111/j.1745-3933.2005.00067.x`.
eprint: `astro-ph/0504456`.

Angulo, R. E. et al. (2012).
"Scaling relations for galaxy clusters in the Millennium-XXL simulation".
In: MNRAS 426, pp. 2046–2062. DOI: `10.1111/j.1365-2966.2012.21830.x`.
arXiv: `1203.3216`.

Angulo, R. E. et al. (2014). "Galaxy formation on the largest scales: the impact of
astrophysics on the baryonic acoustic oscillation peak".
In: MNRAS 442, pp. 2131–2144. DOI: `10.1093/mnras/stu905`.
arXiv: `1311.7100`.

Aslanyan, G. (2014). "Cosmo++: An object-oriented C++ library for cosmology".
In: *Computer Physics Communications* 185, pp. 3215–3227.
DOI: `10.1016/j.cpc.2014.08.021`. arXiv: `1312.4961 [astro-ph.IM]`.

Astropy Collaboration et al. (2013).
"Astropy: A community Python package for astronomy". In: A&A 558, A33, A33.
DOI: `10.1051/0004-6361/201322068`. arXiv: `1307.6212 [astro-ph.IM]`.

Aubourg, É. et al. (2015).
"Cosmological implications of baryon acoustic oscillation measurements".
In: Phys. Rev. D 92.12, 123516, p. 123516. DOI: `10.1103/PhysRevD.92.123516`.
arXiv: `1411.1074`.

Bahcall, N. A. (1986). "The difference between the galaxy and cluster correlation
functions - A manifestation of tails of galaxy clusters". In: ApJ 302, pp. L41–L44.
DOI: `10.1086/184633`.

Bahcall, N. A. and R. M. Soneira (1983).
"The spatial correlation function of rich clusters of galaxies". In: ApJ 270, pp. 20–38.
DOI: `10.1086/161094`.

Baldauf, T. et al. (2010). "Algorithm for the direct reconstruction of the dark matter
correlation function from weak lensing and galaxy clustering".
In: Phys. Rev. D 81.6, 063531, p. 063531. DOI: `10.1103/PhysRevD.81.063531`.
arXiv: `0911.4973 [astro-ph.CO]`.

Baltz, E. A., P. Marshall, and M. Oguri (2009).
"Analytic models of plausible gravitational lens potentials".
In: J. Cosmology Astropart. Phys. 1, 015, p. 015.
DOI: `10.1088/1475-7516/2009/01/015`. arXiv: `0705.0682`.

Benjamin, J. et al. (2013). "CFHTLenS tomographic weak lensing: quantifying accurate
redshift distributions". In: MNRAS 431, pp. 1547–1564.
DOI: `10.1093/mnras/stt276`. arXiv: `1212.3327`.

Berlind, A. A. et al. (2006). "Percolation Galaxy Groups and Clusters in the SDSS
Redshift Survey: Identification, Catalogs, and the Multiplicity Function".
In: ApJS 167, pp. 1–25. DOI: `10.1086/508170`. eprint: `astro-ph/0601346`.

Bernardeau, F. et al. (2002).
"Large-scale structure of the Universe and cosmological perturbation theory".

In: Phys. Rep. 367, pp. 1–248. DOI: `10.1016/S0370-1573(02)00135-7`.
eprint: `astro-ph/0112551`.

Betoule, M. et al. (2014). "Improved cosmological constraints from a joint analysis of the SDSS-II and SNLS supernova samples". In: A&A 568, A22, A22.
DOI: `10.1051/0004-6361/201423413`. arXiv: `1401.4064`.

Beutler, F. et al. (2011). "The 6dF Galaxy Survey: baryon acoustic oscillations and the local Hubble constant". In: MNRAS 416, pp. 3017–3032.
DOI: `10.1111/j.1365-2966.2011.19250.x`. arXiv: `1106.3366`.

Beutler, F. et al. (2012).
"The 6dF Galaxy Survey: $z \approx 0$ measurements of the growth rate and σ_8".
In: MNRAS 423, pp. 3430–3444. DOI: `10.1111/j.1365-2966.2012.21136.x`.
arXiv: `1204.4725`.

Bhattacharya, S. et al. (2013).
"Dark Matter Halo Profiles of Massive Clusters: Theory versus Observations".
In: ApJ 766, 32, p. 32. DOI: `10.1088/0004-637X/766/1/32`. arXiv: `1112.5479`.

Bianchi, D. et al. (2012). "Statistical and systematic errors in redshift-space distortion measurements from large surveys". In: MNRAS 427, pp. 2420–2436.
DOI: `10.1111/j.1365-2966.2012.22110.x`. arXiv: `1203.1545`.

Blake, C. et al. (2011). "The WiggleZ Dark Energy Survey: mapping the distance-redshift relation with baryon acoustic oscillations".
In: MNRAS 418, pp. 1707–1724. DOI: `10.1111/j.1365-2966.2011.19592.x`.
arXiv: `1108.2635`.

Blake, C. et al. (2012). "The WiggleZ Dark Energy Survey: joint measurements of the expansion and growth history at $z < 1$". In: MNRAS 425, pp. 405–414.
DOI: `10.1111/j.1365-2966.2012.21473.x`. arXiv: `1204.3674`.

Blake, C. et al. (2013). "Galaxy And Mass Assembly (GAMA): improved cosmic growth measurements using multiple tracers of large-scale structure".
In: MNRAS 436, pp. 3089–3105. DOI: `10.1093/mnras/stt1791`.
arXiv: `1309.5556`.

Blanton, M. R. et al. (2003).
"The Galaxy Luminosity Function and Luminosity Density at Redshift $z = 0.1$".
In: ApJ 592, pp. 819–838. DOI: `10.1086/375776`. eprint: `astro-ph/0210215`.

Blanton, M. R. et al. (2005). "New York University Value-Added Galaxy Catalog: A Galaxy Catalog Based on New Public Surveys". In: AJ 129, pp. 2562–2578.
DOI: `10.1086/429803`. eprint: `astro-ph/0410166`.

Blas, D., J. Lesgourgues, and T. Tram (2011). "The Cosmic Linear Anisotropy Solving System (CLASS). Part II: Approximation schemes".
In: J. Cosmology Astropart. Phys. 7, 034, p. 034.
DOI: `10.1088/1475-7516/2011/07/034`. arXiv: `1104.2933`.

Brimioulle, F. et al. (2013). "Dark matter halo properties from galaxy-galaxy lensing".
In: MNRAS 432, pp. 1046–1102. DOI: `10.1093/mnras/stt525`.
arXiv: `1303.6287`.

Cacciato, M. et al. (2013). "Cosmological constraints from a combination of galaxy clustering and lensing - III. Application to SDSS data".
In: MNRAS 430, pp. 767–786. DOI: 10.1093/mnras/sts525. arXiv: 1207.0503.

Chevallier, M. and D. Polarski (2001).
"Accelerating Universes with Scaling Dark Matter".
In: *International Journal of Modern Physics D* 10, pp. 213–223.
DOI: 10.1142/S0218271801000822. eprint: gr-qc/0009008.

Chuang, C.-H. et al. (2015). "nIFTy cosmology: Galaxy/halo mock catalogue comparison project on clustering statistics". In: MNRAS 452, pp. 686–700.
DOI: 10.1093/mnras/stv1289. arXiv: 1412.7729.

Coil, A. L. et al. (2008). "The DEEP2 Galaxy Redshift Survey: Color and Luminosity Dependence of Galaxy Clustering at z ~ 1". In: ApJ 672, 153-176, pp. 153–176.
DOI: 10.1086/523639. arXiv: 0708.0004.

Coles, P. and B. Jones (1991).
"A lognormal model for the cosmological mass distribution".
In: MNRAS 248, pp. 1–13. DOI: 10.1093/mnras/248.1.1.

Contreras, C. et al. (2013). "Determining accurate measurements of the growth rate from the galaxy correlation function in simulations". In: MNRAS 430, pp. 934–945.
DOI: 10.1093/mnras/sts649. arXiv: 1302.5167 [astro-ph.CO].

Covone, G. et al. (2014).
"Measurement of the Halo Bias from Stacked Shear Profiles of Galaxy Clusters".
In: ApJ 784, L25, p. L25. DOI: 10.1088/2041-8205/784/2/L25.
arXiv: 1402.4815.

Crocce, M. and R. Scoccimarro (2006).
"Renormalized cosmological perturbation theory".
In: Phys. Rev. D 73.6, 063519, p. 063519. DOI: 10.1103/PhysRevD.73.063519.
eprint: astro-ph/0509418.

Crocce, M., R. Scoccimarro, and F. Bernardeau (2012).
"MPTBREEZE: a fast renormalized perturbative scheme".
In: MNRAS 427, pp. 2537–2551. DOI: 10.1111/j.1365-2966.2012.22127.x.
arXiv: 1207.1465.

Crocce, M. et al. (2010).
"Simulating the Universe with MICE: the abundance of massive clusters".
In: MNRAS 403, pp. 1353–1367. DOI: 10.1111/j.1365-2966.2009.16194.x.
arXiv: 0907.0019.

Cucciati, O. et al. (2016). "Measuring galaxy environment with the synergy of future photometric and spectroscopic surveys". In: MNRAS 462, pp. 1786–1801.
DOI: 10.1093/mnras/stw1729. arXiv: 1604.05323.

Cuesta, A. J. et al. (2016). "The clustering of galaxies in the SDSS-III Baryon Oscillation Spectroscopic Survey: baryon acoustic oscillations in the correlation function of LOWZ and CMASS galaxies in Data Release 12". In: MNRAS 457, pp. 1770–1785.
DOI: 10.1093/mnras/stw066. arXiv: 1509.06371.

Davis, M. and P. J. E. Peebles (1983).
"A survey of galaxy redshifts. V - The two-point position and velocity correlations".
In: ApJ 267, pp. 465–482. DOI: 10.1086/160884.

Dawson, K. S. et al. (2013). "The Baryon Oscillation Spectroscopic Survey of SDSS-III".
In: AJ 145, 10, p. 10. DOI: 10.1088/0004-6256/145/1/10. arXiv: 1208.0022.

Dawson, K. S. et al. (2015). "The SDSS-IV extended Baryon Oscillation Spectroscopic
Survey: Overview and Early Data". In: *ArXiv e-prints*, *arXiv:1508.04473*.
arXiv: 1508.04473.

de la Torre, S. et al. (2013). "The VIMOS Public Extragalactic Redshift Survey (VIPERS) .
Galaxy clustering and redshift-space distortions at $z \simeq 0.8$ in the first data release".
In: A&A 557, A54, A54. DOI: 10.1051/0004-6361/201321463.
arXiv: 1303.2622.

Delubac, T. et al. (2015).
"Baryon acoustic oscillations in the Lyα forest of BOSS DR11 quasars".
In: A&A 574, A59, A59. DOI: 10.1051/0004-6361/201423969.
arXiv: 1404.1801.

Dias Pinto Vitenti, S. and M. Penna-Lima (2014). *NumCosmo: Numerical Cosmology*.
Astrophysics Source Code Library. ascl: 1408.013.

Eisenstein, D. J. and W. Hu (1998). "Baryonic Features in the Matter Transfer Function".
In: ApJ 496, pp. 605–614. DOI: 10.1086/305424. eprint: astro-ph/9709112.

— (1999). "Power Spectra for Cold Dark Matter and Its Variants".
In: ApJ 511, pp. 5–15. DOI: 10.1086/306640. eprint: astro-ph/9710252.

Eisenstein, D. J., H.-J. Seo, and M. White (2007).
"On the Robustness of the Acoustic Scale in the Low-Redshift Clustering of Matter".
In: ApJ 664, pp. 660–674. DOI: 10.1086/518755. eprint: astro-ph/0604361.

Eisenstein, D. J. et al. (2005). "Detection of the Baryon Acoustic Peak in the Large-Scale
Correlation Function of SDSS Luminous Red Galaxies". In: ApJ 633, pp. 560–574.
DOI: 10.1086/466512. eprint: astro-ph/0501171.

Erben, T. et al. (2013). "CFHTLenS: the Canada-France-Hawaii Telescope Lensing
Survey - imaging data and catalogue products". In: MNRAS 433, pp. 2545–2563.
DOI: 10.1093/mnras/stt928. arXiv: 1210.8156.

Estrada, J., E. Sefusatti, and J. A. Frieman (2009). "The Correlation Function of
Optically Selected Galaxy Clusters in the Sloan Digital Sky Survey".
In: ApJ 692, pp. 265–282. DOI: 10.1088/0004-637X/692/1/265.
arXiv: 0801.3485.

Fedeli, C. et al. (2011). "The clustering of galaxies and galaxy clusters: constraints on
primordial non-Gaussianity from future wide-field surveys".
In: MNRAS 414, pp. 1545–1559. DOI: 10.1111/j.1365-2966.2011.18490.x.
arXiv: 1012.2305.

Fisher, K. B., C. A. Scharf, and O. Lahav (1994).
"A spherical harmonic approach to redshift distortion and a measurement of

Omega(0) from the 1.2-Jy IRAS Redshift Survey". In: MNRAS 266, p. 219. DOI: 10.1093/mnras/266.1.219. eprint: astro-ph/9309027.

Ford, J. et al. (2014). "Cluster magnification and the mass-richness relation in CFHTLenS". In: MNRAS 439, pp. 3755–3764. DOI: 10.1093/mnras/stu225. arXiv: 1310.2295 [astro-ph.CO].

Ford, J. et al. (2015). "CFHTLenS: a weak lensing shear analysis of the 3D-Matched-Filter galaxy clusters". In: MNRAS 447, pp. 1304–1318. DOI: 10.1093/mnras/stu2545. arXiv: 1409.3571.

George, M. R. et al. (2012). "Galaxies in X-Ray Groups. II. A Weak Lensing Study of Halo Centering". In: ApJ 757, 2, p. 2. DOI: 10.1088/0004-637X/757/1/2. arXiv: 1205.4262 [astro-ph.CO].

Giocoli, C. et al. (2013). "Characterizing dark interactions with the halo mass accretion history and structural properties". In: MNRAS 434, pp. 2982–2998. DOI: 10.1093/mnras/stt1218. arXiv: 1301.3151.

Gonzalez, A. H. et al. (2013). "Galaxy Cluster Baryon Fractions Revisited". In: ApJ 778, 14, p. 14. DOI: 10.1088/0004-637X/778/1/14. arXiv: 1309.3565.

Goodman, Jonathan and Jonathan Weare (2010). "Ensemble samplers with affine invariance". In: *Communications in Applied Mathematics and Computational Science* 5.1, pp. 65–80.

Grieb, J. N. et al. (2016). "Gaussian covariance matrices for anisotropic galaxy clustering measurements". In: MNRAS 457, pp. 1577–1592. DOI: 10.1093/mnras/stw065. arXiv: 1509.04293.

Gunn, J. E. and J. R. Gott III (1972). "On the Infall of Matter Into Clusters of Galaxies and Some Effects on Their Evolution". In: ApJ 176, p. 1. DOI: 10.1086/151605.

Guzzo, L. et al. (2008). "A test of the nature of cosmic acceleration using galaxy redshift distortions". In: Nature 451, pp. 541–544. DOI: 10.1038/nature06555. arXiv: 0802.1944.

Guzzo, L. et al. (2014). "The VIMOS Public Extragalactic Redshift Survey (VIPERS). An unprecedented view of galaxies and large-scale structure at 0.5 < z < 1.2". In: A&A 566, A108, A108. DOI: 10.1051/0004-6361/201321489. arXiv: 1303.2623.

Hamilton, A. J. S. (1992). "Measuring Omega and the real correlation function from the redshift correlation function". In: ApJ 385, pp. L5–L8. DOI: 10.1086/186264.

— (1993). "Toward Better Ways to Measure the Galaxy Correlation Function". In: ApJ 417, p. 19. DOI: 10.1086/173288.

Hartlap, J., P. Simon, and P. Schneider (2007). "Why your model parameter confidences might be too optimistic. Unbiased estimation of the inverse covariance matrix". In: A&A 464, pp. 399–404. DOI: 10.1051/0004-6361:20066170. eprint: astro-ph/0608064.

Hastings, W. K. (1970).
"Monte Carlo sampling methods using Markov chains and their applications".
In: *Biometrika* 57.1, pp. 97–109. ISSN: 1464-3510. DOI: 10.1093/biomet/57.1.97.
URL: http://dx.doi.org/10.1093/biomet/57.1.97.

Heymans, C. et al. (2012).
"CFHTLenS: the Canada-France-Hawaii Telescope Lensing Survey".
In: MNRAS 427, pp. 146–166. DOI: 10.1111/j.1365-2966.2012.21952.x.
arXiv: 1210.0032.

Hilbert, S. and S. D. M. White (2010).
"Abundances, masses and weak-lensing mass profiles of galaxy clusters as a
function of richness and luminosity in ΛCDM cosmologies".
In: MNRAS 404, pp. 486–501. DOI: 10.1111/j.1365-2966.2010.16310.x.
arXiv: 0907.4371.

Hildebrandt, H. et al. (2012). "CFHTLenS: improving the quality of photometric
redshifts with precision photometry". In: MNRAS 421, pp. 2355–2367.
DOI: 10.1111/j.1365-2966.2012.20468.x. arXiv: 1111.4434.

Hirata, C. M. and U. Seljak (2004).
"Intrinsic alignment-lensing interference as a contaminant of cosmic shear".
In: Phys. Rev. D 70.6, 063526, p. 063526. DOI: 10.1103/PhysRevD.70.063526.
eprint: astro-ph/0406275.

Hong, T., J. L. Han, and Z. L. Wen (2016). "A Detection of Baryon Acoustic Oscillations
from the Distribution of Galaxy Clusters". In: ApJ 826, 154, p. 154.
DOI: 10.3847/0004-637X/826/2/154. arXiv: 1511.00392.

Hong, T. et al. (2012). "The Correlation Function of Galaxy Clusters and Detection of
Baryon Acoustic Oscillations". In: ApJ 749, 81, p. 81.
DOI: 10.1088/0004-637X/749/1/81. arXiv: 1202.0640.

Howlett, C. et al. (2015).
"The clustering of the SDSS main galaxy sample - II. Mock galaxy catalogues and a
measurement of the growth of structure from redshift space distortions at z = 0.15".
In: MNRAS 449, pp. 848–866. DOI: 10.1093/mnras/stu2693.
arXiv: 1409.3238.

Huchra, J. P. and M. J. Geller (1982). "Groups of galaxies. I - Nearby groups".
In: ApJ 257, pp. 423–437. DOI: 10.1086/160000.

Hudson, M. J. et al. (2015).
"CFHTLenS: co-evolution of galaxies and their dark matter haloes".
In: MNRAS 447, pp. 298–314. DOI: 10.1093/mnras/stu2367.
arXiv: 1310.6784.

Hütsi, G. (2010). "Power spectrum of the maxBCG sample: detection of acoustic
oscillations using galaxy clusters". In: MNRAS 401, pp. 2477–2489.
DOI: 10.1111/j.1365-2966.2009.15824.x. arXiv: 0910.0492.

Jarvis, M. (2015). *TreeCorr: Two-point correlation functions*.
Astrophysics Source Code Library. ascl: 1508.007.

Jenkins, A. et al. (2001). "The mass function of dark matter haloes".
    In: MNRAS 321, pp. 372–384. DOI: `10.1046/j.1365-8711.2001.04029.x`.
    eprint: `astro-ph/0005260`.

Johnston, D. E. et al. (2007). "Cross-correlation Weak Lensing of SDSS galaxy Clusters
    II: Cluster Density Profiles and the Mass–Richness Relation". In: *ArXiv e-prints*.
    arXiv: `0709.1159`.

Kaiser, N. (1984). "On the spatial correlations of Abell clusters".
    In: ApJ 284, pp. L9–L12. DOI: `10.1086/184341`.

— (1987). "Clustering in real space and in redshift space". In: MNRAS 227, pp. 1–21.
    DOI: `10.1093/mnras/227.1.1`.

Kazin, E. A. et al. (2014). "The WiggleZ Dark Energy Survey: improved distance
    measurements to z = 1 with reconstruction of the baryonic acoustic feature".
    In: MNRAS 441, pp. 3524–3542. DOI: `10.1093/mnras/stu778`.
    arXiv: `1401.0358`.

Kilbinger, M. et al. (2011). "CosmoPMC: Cosmology Population Monte Carlo".
    In: *ArXiv e-prints*. arXiv: `1101.0950`.

Kilbinger, M. et al. (2013). "CFHTLenS: combined probe cosmological model
    comparison using 2D weak gravitational lensing". In: MNRAS 430, pp. 2200–2220.
    DOI: `10.1093/mnras/stt041`. arXiv: `1212.3338`.

Koester, B. P. et al. (2007).
    "A MaxBCG Catalog of 13,823 Galaxy Clusters from the Sloan Digital Sky Survey".
    In: ApJ 660, pp. 239–255. DOI: `10.1086/509599`. eprint: `astro-ph/0701265`.

Labatie, A. et al. (2010). "Uncertainty in 2-point correlation function estimators and
    BAO detection in SDSS DR7". In: *ArXiv e-prints*.
    arXiv: `1009.1232 [astro-ph.CO]`.

Lahav, O. et al. (1991). "Dynamical effects of the cosmological constant".
    In: MNRAS 251, pp. 128–136. DOI: `10.1093/mnras/251.1.128`.

Landy, S. D. and A. S. Szalay (1993).
    "Bias and variance of angular correlation functions". In: ApJ 412, pp. 64–71.
    DOI: `10.1086/172900`.

Laureijs, R. et al. (2011). "Euclid Definition Study Report". In: *ArXiv e-prints*.
    arXiv: `1110.3193 [astro-ph.CO]`.

Leauthaud, A. et al. (2012). "New Constraints on the Evolution of the Stellar-to-dark
    Matter Connection: A Combined Analysis of Galaxy-Galaxy Lensing, Clustering,
    and Stellar Mass Functions from z = 0.2 to z =1". In: ApJ 744, 159, p. 159.
    DOI: `10.1088/0004-637X/744/2/159`. arXiv: `1104.0928`.

Lesgourgues, J. (2011).
    "The Cosmic Linear Anisotropy Solving System (CLASS) I: Overview".
    In: *ArXiv e-prints*. arXiv: `1104.2932 [astro-ph.IM]`.

Lewis, A. and S. Bridle (2002).
    "Cosmological parameters from CMB and other data: A Monte Carlo approach".

In: Phys. Rev. D 66.10, 103511, p. 103511. DOI: 10.1103/PhysRevD.66.103511. eprint: astro-ph/0205436.

Lewis, A., A. Challinor, and A. Lasenby (2000). "Efficient Computation of Cosmic Microwave Background Anisotropies in Closed Friedmann-Robertson-Walker Models". In: ApJ 538, pp. 473–476. DOI: 10.1086/309179. eprint: astro-ph/9911177.

Linder, E. V. and A. Jenkins (2003). "Cosmic structure growth and dark energy". In: MNRAS 346, pp. 573–583. DOI: 10.1046/j.1365-2966.2003.07112.x. eprint: astro-ph/0305286.

Maartens, R. (2011). "Is the Universe homogeneous?" In: *Philosophical Transactions of the Royal Society of London Series A* 369, pp. 5115–5137. DOI: 10.1098/rsta.2011.0289. arXiv: 1104.1300.

Mana, A. et al. (2013). "Combining clustering and abundances of galaxy clusters to test cosmology and primordial non-Gaussianity". In: MNRAS 434, pp. 684–695. DOI: 10.1093/mnras/stt1062. arXiv: 1303.0287 [astro-ph.CO].

Mandelbaum, R., U. Seljak, and C. M. Hirata (2008). "A halo mass-concentration relation from weak lensing". In: J. Cosmology Astropart. Phys. 8, 006, p. 006. DOI: 10.1088/1475-7516/2008/08/006. arXiv: 0805.2552.

Mandelbaum, R. et al. (2013). "Cosmological parameter constraints from galaxy-galaxy lensing and galaxy clustering with the SDSS DR7". In: MNRAS 432, pp. 1544–1575. DOI: 10.1093/mnras/stt572. arXiv: 1207.1120.

Mantz, A. et al. (2010). "The observed growth of massive galaxy clusters - II. X-ray scaling relations". In: MNRAS 406, pp. 1773–1795. DOI: 10.1111/j.1365-2966.2010.16993.x. arXiv: 0909.3099.

Marulli, F., M. Baldi, and L. Moscardini (2012). "Clustering and redshift-space distortions in interacting dark energy cosmologies". In: MNRAS 420, pp. 2377–2386. DOI: 10.1111/j.1365-2966.2011.20199.x. arXiv: 1110.3045 [astro-ph.CO].

Marulli, F., A. Veropalumbo, and M. Moresco (2016). "CosmoBolognaLib: C++ libraries for cosmological calculations". In: *Astronomy and Computing* 14, pp. 35–42. DOI: 10.1016/j.ascom.2016.01.005. arXiv: 1511.00012.

Marulli, F. et al. (2011). "Effects of massive neutrinos on the large-scale structure of the Universe". In: MNRAS 418, pp. 346–356. DOI: 10.1111/j.1365-2966.2011.19488.x. arXiv: 1103.0278 [astro-ph.CO].

Marulli, F. et al. (2012). "Cosmology with clustering anisotropies: disentangling dynamic and geometric distortions in galaxy redshift surveys". In: MNRAS 426, pp. 2566–2580. DOI: 10.1111/j.1365-2966.2012.21875.x. arXiv: 1203.1002 [astro-ph.CO].

Marulli, F. et al. (2013). "The VIMOS Public Extragalactic Redshift Survey (VIPERS) .
    Luminosity and stellar mass dependence of galaxy clustering at $0.5 < z < 1.1$".
    In: A&A 557, A17, A17. DOI: 10.1051/0004-6361/201321476.
    arXiv: 1303.2633.

Marulli, F. et al. (2015).
    "Redshift-space distortions of galaxies, clusters and AGN: testing how the accuracy
    of growth rate measurements depends on scales and sample selections".
    In: *ArXiv e-prints*. arXiv: 1505.01170.

McBride, C. et al. (2009). "LasDamas Mock Galaxy Catalogs for SDSS".
    In: *American Astronomical Society Meeting Abstracts #213*. Vol. 41.
    Bulletin of the American Astronomical Society, p. 253.

Medezinski, E. et al. (2010). "Detailed cluster mass and light profiles of A1703, A370
    and RXJ1347-11 from deep Subaru imaging". In: MNRAS 405, pp. 257–273.
    DOI: 10.1111/j.1365-2966.2010.16491.x. arXiv: 0906.4791.

Merloni, A. et al. (2012).
    "eROSITA Science Book: Mapping the Structure of the Energetic Universe".
    In: *ArXiv e-prints*. arXiv: 1209.3114 [astro-ph.HE].

Meszaros, P. (1974).
    "The behaviour of point masses in an expanding cosmological substratum".
    In: A&A 37, pp. 225–228.

Miller, L. et al. (2013). "Bayesian galaxy shape measurement for weak lensing surveys -
    III. Application to the Canada-France-Hawaii Telescope Lensing Survey".
    In: MNRAS 429, pp. 2858–2880. DOI: 10.1093/mnras/sts454.
    arXiv: 1210.8201 [astro-ph.CO].

Miyatake, H. et al. (2015).
    "The Weak Lensing Signal and the Clustering of BOSS Galaxies. I. Measurements".
    In: ApJ 806, 1, p. 1. DOI: 10.1088/0004-637X/806/1/1. arXiv: 1311.1480.

More, S. et al. (2015). "The Weak Lensing Signal and the Clustering of BOSS Galaxies.
    II. Astrophysical and Cosmological Constraints". In: ApJ 806, 2, p. 2.
    DOI: 10.1088/0004-637X/806/1/2. arXiv: 1407.1856.

Moresco, M. et al. (2014). "Disentangling interacting dark energy cosmologies with the
    three-point correlation function". In: MNRAS 443, pp. 2874–2886.
    DOI: 10.1093/mnras/stu1359. arXiv: 1312.4530.

Moresco, M. et al. (2016). "The VIMOS Public Extragalactic Redshift Survey (VIPERS).
    Exploring the dependence of the three-point correlation function on stellar mass
    and luminosity at 0.5<z<1.1". In: *ArXiv e-prints*. arXiv: 1603.08924.

Moscardini, L. et al. (2000). "The correlation function of X-ray galaxy clusters in the
    ROSAT All-Sky Survey 1 Bright Sample". In: MNRAS 314, pp. 647–656.
    DOI: 10.1046/j.1365-8711.2000.03372.x. eprint: astro-ph/9904282.

Norberg, P. et al. (2009). "Statistical analysis of galaxy surveys - I. Robust error
    estimation for two-point clustering statistics". In: MNRAS 396, pp. 19–38.
    DOI: 10.1111/j.1365-2966.2009.14389.x. arXiv: 0810.1885.

Oguri, M. (2014). "A cluster finding algorithm based on the multiband identification of red sequence galaxies". In: MNRAS 444, pp. 147–161.
DOI: `10.1093/mnras/stu1446`. arXiv: `1407.4693`.

Oguri, M. and T. Hamana (2011). "Detailed cluster lensing profiles at large radii and the impact on cluster weak lensing studies". In: MNRAS 414, pp. 1851–1861.
DOI: `10.1111/j.1365-2966.2011.18481.x`. arXiv: `1101.0650`.

Oguri, M. and M. Takada (2011). "Combining cluster observables and stacked weak lensing to probe dark energy: Self-calibration of systematic uncertainties".
In: Phys. Rev. D 83.2, 023008, p. 023008. DOI: `10.1103/PhysRevD.83.023008`.
arXiv: `1010.0744`.

Oguri, M. et al. (2012). "Combined strong and weak lensing analysis of 28 clusters from the Sloan Giant Arcs Survey". In: MNRAS 420, pp. 3213–3239.
DOI: `10.1111/j.1365-2966.2011.20248.x`. arXiv: `1109.2594`.

Oka, A. et al. (2014). "Simultaneous constraints on the growth of structure and cosmic expansion from the multipole power spectra of the SDSS DR7 LRG sample".
In: MNRAS 439, pp. 2515–2530. DOI: `10.1093/mnras/stu111`.
arXiv: `1310.2820 [astro-ph.CO]`.

Okabe, N. et al. (2013).
"LoCuSS: The Mass Density Profile of Massive Galaxy Clusters at z = 0.2".
In: ApJ 769, L35, p. L35. DOI: `10.1088/2041-8205/769/2/L35`.
arXiv: `1302.2728`.

Padmanabhan, N. et al. (2012).
"A 2 per cent distance to z = 0.35 by reconstructing baryon acoustic oscillations - I. Methods and application to the Sloan Digital Sky Survey".
In: MNRAS 427, pp. 2132–2145. DOI: `10.1111/j.1365-2966.2012.21888.x`.
arXiv: `1202.0090`.

Pan, J. (2007). "Fractional Brownian motion and the halo mass function".
In: MNRAS 374, pp. L6–L9. DOI: `10.1111/j.1745-3933.2006.00253.x`.
eprint: `astro-ph/0610451`.

Peacock, J. A. and S. J. Dodds (1996).
"Non-linear evolution of cosmological power spectra".
In: MNRAS 280, pp. L19–L26. DOI: `10.1093/mnras/280.3.L19`.
eprint: `astro-ph/9603031`.

Peebles, P. J. E. (1980). *The large-scale structure of the universe*.

Peebles, P. J. E. and M. G. Hauser (1974). "Statistical Analysis of Catalogs of Extragalactic Objects. III. The Shane-Wirtanen and Zwicky Catalogs".
In: ApJS 28, p. 19. DOI: `10.1086/190308`.

Percival, W. J. et al. (2004). "The 2dF Galaxy Redshift Survey: spherical harmonics analysis of fluctuations in the final catalogue". In: MNRAS 353, pp. 1201–1218.
DOI: `10.1111/j.1365-2966.2004.08146.x`. eprint: `astro-ph/0406513`.

Petracca, F. et al. (2016). "Forecasts on neutrino mass constraints from the
    redshift-space two-point correlation function". In: MNRAS 462, pp. 4208–4219.
    DOI: 10.1093/mnras/stw1948. arXiv: 1512.06139.

Planck Collaboration et al. (2014a).
    "Planck 2013 results. XVI. Cosmological parameters". In: A&A 571, A16, A16.
    DOI: 10.1051/0004−6361/201321591. arXiv: 1303.5076.

— (2014b).
    "Planck 2013 results. XX. Cosmology from Sunyaev-Zeldovich cluster counts".
    In: A&A 571, A20, A20. DOI: 10.1051/0004−6361/201321521.
    arXiv: 1303.5080.

— (2014c).
    "Planck 2013 results. XX. Cosmology from Sunyaev-Zeldovich cluster counts".
    In: A&A 571, A20, A20. DOI: 10.1051/0004−6361/201321521.
    arXiv: 1303.5080.

Planck Collaboration et al. (2016). "Planck 2015 results. XIII. Cosmological parameters".
    In: A&A 594, A13, A13. DOI: 10.1051/0004−6361/201525830.
    arXiv: 1502.01589.

Prada, F. et al. (2016).
    "Hunting down systematics in baryon acoustic oscillations after cosmic high noon".
    In: MNRAS 458, pp. 613–623. DOI: 10.1093/mnras/stw312. arXiv: 1410.4684.

Press, W. H. and P. Schechter (1974). "Formation of Galaxies and Clusters of Galaxies
    by Self-Similar Gravitational Condensation". In: ApJ 187, pp. 425–438.
    DOI: 10.1086/152650.

Reed, D. S. et al. (2007).
    "The halo mass function from the dark ages through the present day".
    In: MNRAS 374, pp. 2–15. DOI: 10.1111/j.1365−2966.2006.11204.x.
    eprint: astro-ph/0607150.

Reid, B. et al. (2016). "SDSS-III Baryon Oscillation Spectroscopic Survey Data Release
    12: galaxy target selection and large-scale structure catalogues".
    In: MNRAS 455, pp. 1553–1573. DOI: 10.1093/mnras/stv2382.
    arXiv: 1509.06529.

Ross, A. J. et al. (2012). "The clustering of galaxies in the SDSS-III Baryon Oscillation
    Spectroscopic Survey: analysis of potential systematics".
    In: MNRAS 424, pp. 564–590. DOI: 10.1111/j.1365−2966.2012.21235.x.
    arXiv: 1203.6499.

Ross, A. J. et al. (2015). "The clustering of the SDSS DR7 main Galaxy sample - I. A 4
    per cent distance measure at z = 0.15". In: MNRAS 449, pp. 835–847.
    DOI: 10.1093/mnras/stv154. arXiv: 1409.3242.

Ross, A. J. et al. (2016). "The clustering of galaxies in the completed SDSS-III Baryon
    Oscillation Spectroscopic Survey: Observational systematics and baryon acoustic
    oscillations in the correlation function". In: MNRAS.
    DOI: 10.1093/mnras/stw2372. arXiv: 1607.03145.

Rozo, E. et al. (2010). "Cosmological Constraints from the Sloan Digital Sky Survey maxBCG Cluster Catalog". In: ApJ 708, pp. 645–660. DOI: 10.1088/0004-637X/708/1/645. arXiv: 0902.3702 [astro-ph.CO].

Rykoff, E. S. et al. (2014). "redMaPPer. I. Algorithm and SDSS DR8 Catalog". In: ApJ 785, 104, p. 104. DOI: 10.1088/0004-637X/785/2/104. arXiv: 1303.3562.

Sánchez, A. G., C. M. Baugh, and R. E. Angulo (2008). "What is the best way to measure baryonic acoustic oscillations?" In: MNRAS 390, pp. 1470–1490. DOI: 10.1111/j.1365-2966.2008.13769.x. arXiv: 0804.0233.

Sanchez, A. G. et al. (2016). "The clustering of galaxies in the completed SDSS-III Baryon Oscillation Spectroscopic Survey: cosmological implications of the configuration-space clustering wedges". In: *ArXiv e-prints*. arXiv: 1607.03147.

Sánchez, A. G. et al. (2012). "The clustering of galaxies in the SDSS-III Baryon Oscillation Spectroscopic Survey: cosmological implications of the large-scale two-point correlation function". In: MNRAS 425, pp. 415–437. DOI: 10.1111/j.1365-2966.2012.21502.x. arXiv: 1203.6616.

Sartoris, B. et al. (2016). "Next generation cosmology: constraints from the Euclid galaxy cluster survey". In: MNRAS 459, pp. 1764–1780. DOI: 10.1093/mnras/stw630. arXiv: 1505.02165.

Saunders, W., M. Rowan-Robinson, and A. Lawrence (1992). "The spatial correlation function of IRAS galaxies on small and intermediate scales". In: MNRAS 258, pp. 134–146. DOI: 10.1093/mnras/258.1.134.

Sereno, M. and S. Ettori (2014). "Comparing Masses in Literature (CoMaLit)-I. Bias and scatter in weak lensing and X-ray mass estimates of clusters". In: *ArXiv e-prints*. arXiv: 1407.7868.

Sereno, M., S. Ettori, and L. Moscardini (2015). "CoMaLit - II. The scaling relation between mass and Sunyaev-Zel'dovich signal for Planck selected galaxy clusters". In: MNRAS 450, pp. 3649–3664. DOI: 10.1093/mnras/stv809. arXiv: 1407.7869.

Sereno, M. et al. (2015). "New constraints on σ_8 from a joint analysis of stacked gravitational lensing and clustering of galaxy clusters". In: MNRAS 449, pp. 4147–4161. DOI: 10.1093/mnras/stv280. arXiv: 1410.5438.

Shen, J. et al. (2006). "An Excursion Set Model of the Cosmic Web: The Abundance of Sheets, Filaments, and Halos". In: ApJ 645, pp. 783–791. DOI: 10.1086/504513. eprint: astro-ph/0511365.

Sheth, R. K., H. J. Mo, and G. Tormen (2001). "Ellipsoidal collapse and an improved model for the number and spatial distribution of dark matter haloes".

In: MNRAS 323, pp. 1–12. DOI: 10.1046/j.1365-8711.2001.04006.x. eprint: astro-ph/9907024.

Sheth, R. K. and G. Tormen (1999). "Large-scale bias and the peak background split". In: MNRAS 308, pp. 119–126. DOI: 10.1046/j.1365-8711.1999.02692.x. eprint: astro-ph/9901122.

— (2002). "An excursion set model of hierarchical clustering: ellipsoidal collapse and the moving barrier". In: MNRAS 329, pp. 61–75. DOI: 10.1046/j.1365-8711.2002.04950.x. eprint: astro-ph/0105113.

Stevans, M. L. et al. (2014). "The NEWFIRM HETDEX Survey - Studying Galaxy Growth with 400,000 Galaxies at $2 < z < 3.5$". In: *American Astronomical Society Meeting Abstracts #223*. Vol. 223. American Astronomical Society Meeting Abstracts, p. 254.47.

Swanson, M. E. C. et al. (2008). "Methods for rapidly processing angular masks of next-generation galaxy surveys". In: MNRAS 387, pp. 1391–1402. DOI: 10.1111/j.1365-2966.2008.13296.x. arXiv: 0711.4352.

Szapudi, I. and A. S. Szalay (1998). "A New Class of Estimators for the N-Point Correlations". In: ApJ 494, pp. L41–L44. DOI: 10.1086/311146.

Taghizadeh-Popp, M. (2010). "CfunBASE: A Cosmological Functions Library for Astronomical Databases". In: PASP 122, pp. 976–989. DOI: 10.1086/655666.

Tempel, E. et al. (2014). "Flux- and volume-limited groups/clusters for the SDSS galaxies: catalogues and mass estimation". In: A&A 566, A1, A1. DOI: 10.1051/0004-6361/201423585. arXiv: 1402.1350.

Tinker, J. L. et al. (2010). "The Large-scale Bias of Dark Matter Halos: Numerical Calibration and Model Tests". In: ApJ 724, pp. 878–886. DOI: 10.1088/0004-637X/724/2/878. arXiv: 1001.3162.

Tinker, J. L. et al. (2012). "Cosmological Constraints from Galaxy Clustering and the Mass-to-number Ratio of Galaxy Clusters". In: ApJ 745, 16, p. 16. DOI: 10.1088/0004-637X/745/1/16. arXiv: 1104.1635.

Tinker, J. et al. (2008). "Toward a Halo Mass Function for Precision Cosmology: The Limits of Universality". In: ApJ 688, 709-728, pp. 709–728. DOI: 10.1086/591439. arXiv: 0803.2706.

Umetsu, K. et al. (2014). "CLASH: Weak-lensing Shear-and-magnification Analysis of 20 Galaxy Clusters". In: ApJ 795, 163, p. 163. DOI: 10.1088/0004-637X/795/2/163. arXiv: 1404.1375.

Vanderplas, J.T. et al. (2012). "Introduction to astroML: Machine learning for astrophysics". In: *Conference on Intelligent Data Understanding (CIDU)*, pp. 47–54. DOI: 10.1109/CIDU.2012.6382200.

Velander, M. et al. (2014). "CFHTLenS: the relation between galaxy dark matter haloes and baryons from weak gravitational lensing". In: MNRAS 437, pp. 2111–2136. DOI: 10.1093/mnras/stt2013. arXiv: 1304.4265.

Veropalumbo, A. et al. (2014). "An improved measurement of baryon acoustic oscillations from the correlation function of galaxy clusters at z ∼ 0.3". In: MNRAS 442, pp. 3275–3283. DOI: 10.1093/mnras/stu1050. arXiv: 1311.5895.

— (2016). "Measuring the distance-redshift relation with the baryon acoustic oscillations of galaxy clusters". In: MNRAS 458, pp. 1909–1920. DOI: 10.1093/mnras/stw306. arXiv: 1510.08852.

Vikhlinin, A. et al. (2009). "Chandra Cluster Cosmology Project III: Cosmological Parameter Constraints". In: ApJ 692, pp. 1060–1074. DOI: 10.1088/0004-637X/692/2/1060. arXiv: 0812.2720.

Villaescusa-Navarro, F. et al. (2014). "Cosmology with massive neutrinos I: towards a realistic modeling of the relation between matter, haloes and galaxies". In: J. Cosmology Astropart. Phys. 3, 011, p. 011. DOI: 10.1088/1475-7516/2014/03/011. arXiv: 1311.0866.

Wang, Q. and H. Zhan (2013). "Mass-dependent Baryon Acoustic Oscillation Signal and Halo Bias". In: ApJ 768, L27, p. L27. DOI: 10.1088/2041-8205/768/2/L27. arXiv: 1302.1640.

Warren, M. S. et al. (2006). "Precision Determination of the Mass Function of Dark Matter Halos". In: ApJ 646, pp. 881–885. DOI: 10.1086/504962. eprint: astro-ph/0506395.

Wen, Z. L. and J. L. Han (2015). "Calibration of the Optical Mass Proxy for Clusters of Galaxies and an Update of the WHL12 Cluster Catalog". In: ApJ 807, 178, p. 178. DOI: 10.1088/0004-637X/807/2/178. arXiv: 1506.04503.

Wen, Z. L., J. L. Han, and F. S. Liu (2009). "Galaxy Clusters Identified from the SDSS DR6 and Their Properties". In: ApJS 183, pp. 197–213. DOI: 10.1088/0067-0049/183/2/197. arXiv: 0906.0803.

— (2012). "A Catalog of 132,684 Clusters of Galaxies Identified from Sloan Digital Sky Survey III". In: ApJS 199, 34, p. 34. DOI: 10.1088/0067-0049/199/2/34. arXiv: 1202.6424 [astro-ph.CO].

White, M. (2015). "Reconstruction within the Zeldovich approximation". In: MNRAS 450, pp. 3822–3828. DOI: 10.1093/mnras/stv842. arXiv: 1504.03677.

Yang, X. et al. (2006). "Weak lensing by galaxies in groups and clusters - I. Theoretical expectations". In: MNRAS 373, pp. 1159–1172. DOI: 10.1111/j.1365-2966.2006.11091.x. eprint: astro-ph/0607552.

Yoo, J. and U. Seljak (2012). "Joint analysis of gravitational lensing, clustering, and
    abundance: Toward the unification of large-scale structure analysis".
    In: Phys. Rev. D 86.8, 083504, p. 083504. DOI: 10.1103/PhysRevD.86.083504.
    arXiv: 1207.2471.

Yoo, J. et al. (2006). "From Galaxy-Galaxy Lensing to Cosmological Parameters".
    In: ApJ 652, pp. 26–42. DOI: 10.1086/507591. eprint: astro-ph/0511580.

Zehavi, I. et al. (2011). "Galaxy Clustering in the Completed SDSS Redshift Survey: The
    Dependence on Color and Luminosity". In: ApJ 736, 59, p. 59.
    DOI: 10.1088/0004-637X/736/1/59. arXiv: 1005.2413.

Zel'dovich, Y. B. (1970).
    "Gravitational instability: An approximate theory for large density perturbations."
    In: A&A 5, pp. 84–89.

Zitrin, A. et al. (2012). "Miscentring in galaxy clusters: dark matter to brightest cluster
    galaxy offsets in 10 000 Sloan Digital Sky Survey clusters".
    In: MNRAS 426, pp. 2944–2956. DOI: 10.1111/j.1365-2966.2012.21886.x.
    arXiv: 1208.1766 [astro-ph.CO].

Zurek, W. H. et al. (1994). "Large-scale structure after COBE: Peculiar velocities and
    correlations of cold dark matter halos". In: ApJ 431, pp. 559–568.
    DOI: 10.1086/174507.